UNIVERSIDADE FEDERAL DE VIÇOSA

Criticality in dynamical systems through complex networks

Juliane Teixeira de Moraes
Doctor Scientiae

VIÇOSA - MINAS GERAIS
2025

JULIANE TEIXEIRA DE MORAES

Criticality in dynamical systems through complex networks

Thesis submitted to the Physics Graduate Program of the Universidade Federal de Viçosa in partial fulfillment of the requirements for the degree of *Doctor Scientiae*.

Adviser: Silvio da C. F. Junior

VIÇOSA - MINAS GERAIS
2025

Ficha catalográfica elaborada pela Biblioteca Central da Universidade Federal de Viçosa - Campus Viçosa

T
M827c
2025

Moraes, Juliane Teixeira de, 1996-
Criticality in dynamical systems through complex networks / Juliane Teixeira de Moraes. – Viçosa, MG, 2025.
1 tese eletrônica (148 f.): il. (algumas color.).

Texto em inglês.
Inclui apêndices.
Orientador: Silvio da Costa Ferreira Junior.
Tese (doutorado) - Universidade Federal de Viçosa, Departamento de Física, 2025.
Referências bibliográficas: f. 119-134.
DOI: https://doi.org/10.47328/ufvbbt.2025.506
Modo de acesso: World Wide Web.

1. Transformações de fase (Física estatística). 2. Teoria dos grafos. I. Ferreira Junior, Silvio da Costa, 1976-.
II. Universidade Federal de Viçosa. Departamento de Física. Programa de Pós-Graduação em Física. III. Título.

CDD 22. ed. 530.474

Bibliotecário(a) responsável: Euzébio Luiz Pinto CRB-6/3317

JULIANE TEIXEIRA DE MORAES

Criticality in dynamical systems through complex networks

Thesis submitted to the Physics Graduate Program of the Universidade Federal de Viçosa in partial fulfillment of the requirements for the degree of *Doctor Scientiae*.

APPROVED: July 4, 2025.

Assent:

Juliane Teixeira de Moraes
Author

Silvio da Costa Ferreira Junior
Adviser

Aos meus pais Eleonora e Maurício,
e meu irmão Leonardo.

ACKNOWLEDGMENTS

First of all, I express my deepest gratitude to God for allowing me, in His infinite goodness, to complete this journey of my doctoral studies and for gifting me the privilege of having such amazing people in my life, especially my family. I am profoundly thankful to my parents and my brother for their support throughout this process. This achievement would not be possible without their love and care in the moments I needed the most. I also want to thank my fiancé, who accompanied me during all these years of post-graduation, making this process much lighter and happier.

Special thanks to my friends from Universidade Federal de Viçosa, who provided such good times in this city that I will carry forever in my heart. The years I spent with you will always be remembered as the most fun I ever had. Thank you very much for all the laughter!

I am also sincerely thankful to my advisor for instructing me as a scientist with patience and comprehension. I am profoundly grateful for all the learning you have passed to me throughout these years.

My sincere appreciation to the CEMSC3 group, who hosted me during my research internship in Argentina. Thank you all for the great hospitality and the financial support.

Finally, I would like to thank all my professors for inspiring me in this beautiful profession. I also thank all the staff from UFV, and I thank the university for providing the infrastructure for my research, also enabled by the Núcleo de Simulação de Sistemas Complexos (NSSC), which supplied the computational resources.

This work has been sponsored by the following Brazilian research agencies: Coordination for the Improvement of Higher Education Personnel (CAPES; Financing code 001), Minas Gerais State Foundation for Research Aid (FAPEMIG) and National Council of Scientific and Technological Development (CNPq).

Don’t give up.
You can do anything you want to, but you have to work at it.
Annie Easley, a computer scientist who paved the way for women in STEM.

ABSTRACT

MORAES, Juliane Teixeira de, D.Sc., Universidade Federal de Viçosa, July, 2025. **Criticality in dynamical systems through complex networks**. Adviser: Silvio da Costa Ferreira Junior.

The study of phase transitions, which originated in the context of equilibrium systems, can be extended to a broad range of applications, including non-equilibrium cases. An example is the absorbing state phase transition, where a system undergoes a transition from an absorbing to an active state. This type of transition occurs, for instance, in models inspired by spreading phenomena. The system may be poised between the two phases, in a critical state characterized by a diverging susceptibility in the thermodynamic limit. These concepts are explored in the present thesis, starting from a simple equilibrium example and extending to the description of absorbing state phase transitions. In addition, spreading processes can be investigated using complex networks as substrates. A brief review of basic concepts and models, as well as the broad applicability of complex networks, is also included in this thesis. Thus, the criticality of dynamical systems on complex networks is addressed in two directions: using visibility graphs and intermittent networks. The visibility graph method is used to map time series onto networks. We applied this framework to generate and analyze visibility graphs from time series of the density of infected individuals. The main network metric used is the degree correlation. We found that asymptotic disassortativity in the visibility graph is a hallmark of criticality in the system. Furthermore, we show how localization in the original system can blur this signature of criticality. The other approach involved a temporal network implementation based on the intermittent activity of nodes or links. Changes in the states of nodes and links, following a general renewal process, can capture the temporal heterogeneity observed in real social interactions. Simulating spreading processes on these intermittent networks provided important insights into how inter-event time distributions influence the epidemic threshold. Moreover, when investigating the critical exponents of the absorbing state phase transition in intermittent lattices, we raised the possibility of temporal Griffiths phases occurring in this system. Additionally, criticality is discussed in the context of neuronal activity, including evidence supporting the critical brain hypothesis. In this context, a control strategy for an individual neuron model is explored. Brain criticality is a broad research topic and a promising system for applying methods discussed in the thesis.

Keywords: phase transitions; spreading process; visibility graphs; intermittent networks.

RESUMO

MORAES, Juliane Teixeira de, D.Sc., Universidade Federal de Viçosa, julho de 2025. **Criticalidade em sistemas dinâmicos através de redes complexas**. Orientador: Silvio da Costa Ferreira Junior.

O estudo das transições de fase, que se originou no contexto de sistemas em equilíbrio, pode ser estendido a uma ampla gama de aplicações, incluindo casos de não equilíbrio. Um exemplo é a transição de fase para estados absorventes, onde um sistema passa de um estado absorvente para um estado ativo. Esse tipo de transição ocorre, por exemplo, em modelos inspirados em fenômenos de disseminação, em que o sistema pode estar em um estado entre as duas fases. Esse estado crítico é caracterizado por uma suscetibilidade divergente no limite termodinâmico. Esses conceitos são explorados nesta tese, partindo de um exemplo simples de equilíbrio e estendendo-se à descrição das transições de fase para estado absorvente. Além disso, os processos de disseminação podem ser investigados usando redes complexas como substratos. Uma breve revisão dos conceitos e modelos básicos, bem como da ampla aplicabilidade de redes complexas, também está incluída nesta tese. Assim, a criticalidade de sistemas dinâmicos em redes complexas é abordada em duas direções: usando grafos de visibilidade e redes intermitentes. O método do grafo de visibilidade é usado para mapear séries temporais em redes. Usamos esse mapeamento para gerar e analisar grafos de visibilidade a partir de séries temporais da densidade de indivíduos infectados. A principal análise de rede utilizada é a correlação de grau. Constatamos que a desassortatividade assintótica no grafo de visibilidade é uma característica marcante que mostra criticalidade no sistema. Além disso, mostramos como a presença de localização no sistema original pode mascarar essa assinatura de criticalidade. A outra abordagem envolveu uma implementação de rede temporal baseada na atividade intermitente de nós ou ligações. As mudanças nos estados de nós e ligações (eventos), seguindo um processo de renovação, podem capturar a heterogeneidade temporal observada em interações sociais reais. A simulação de processos de disseminação nessas redes intermitentes forneceu percepções importantes sobre como a distribuição de tempos entre eventos influencia o limiar epidêmico. Além disso, ao investigar os expoentes críticos da transição de fase para estado absorvente em redes intermitentes, levantamos a possibilidade de ocorrência de fases de Griffiths temporais. Além disso, nesta tese a criticalidade é discutida no contexto da atividade neuronal, incluindo evidências que apoiam a hipótese do cérebro crítico. Neste contexto,

explora-se uma estratégia de controle para um modelo de neurônio individual. A criticalidade cerebral é um tópico de pesquisa rico e um sistema promissor para a aplicação de métodos discutidos ao longo desta tese.

Palavras-chave: transições de fase ; processos de disseminação ; grafos de visibilidade ; redes intermitentes

List of abbreviations and acronyms

ASPT	Absorbing State Phase Transition
CP	Contact Process
SIS	Susceptible-Infected-Susceptible
2SCP	Two-Species Contact Process
QCP	Quenched Contact Process
RRN	Random Regular Network
ER	Erdős-Renyi Network
GP	Griffiths Phase
VG	Visibility Graph
HMF	Heterogeneous Mean Field
QMF	Quenched Mean Field
UCM	Uncorrelated Configuration Model
OGA	Optmized Gillespie Algorithm
NI	Node Intermittent
LI	Link Intermittent
TGP	Temporal Griffiths Phase
CM	Chialvo Map

Contents

1 Introduction

Taking a kettle full of water to heat on the stove is a daily habit for many people. If you pause to observe the water as it begins to boil, you can see the coexistence of two phases in the kettle: liquid water and the bubbles of gas forming within it. However, if you could considerably increase the pressure and temperature, specifically to $p = 218$ atm and $T = 374$ ºC, you would observe a very different behavior. These values correspond to the critical point of water, where the liquid-gas coexistence disappears. This means that, in contrast to the abrupt change in density between liquid and gas phases seen at standard conditions, at the critical point, there is no distinction between the two phases. Many other unusual properties arise at the critical point, for instance, the fluid becomes highly susceptible to slight variations in pressure [1]. A completely different system, such as a magnetic material, exhibits similar threshold behavior when cooled: some materials change from a paramagnetic to a ferromagnetic state when the temperature drops below a critical value, leading to the spontaneous emergence of non-zero magnetization. Both cases are examples of critical phase transitions and belong to the same universality class [2]. According to the universality hypothesis, different critical phenomena can be grouped into a small number of universality classes, each characterized by the same critical exponents and scaling functions.

The aforementioned examples are drawn from the realm of equilibrium phenomena, where, after sufficiently long periods, the system evolves into a state that depends neither on time nor on its history [3]. However, the concept of universality extends beyond equilibrium and applies also to non-equilibrium systems, which are present in both living and non-living nature. Non-equilibrium systems are typically history-dependent and characterized by a continuous flux of matter, energy, or other quantities [4]. For instance, models inspired by the propagation of rumors or infectious diseases may be examples of non-equilibrium phenomena belonging to the Direct Percolation (DP) universality class. A particularly relevant realization of DP is the absorbing-state phase transition, wherein the system shifts from an absorbing (inactive) state to an active one. This type of transition has been extensively studied in the context of spreading dynamics [5].

Still within the context of epidemic propagation, the recent COVID-19 pandemic emphasized the urgent need for models of spreading dynamics and techniques for tracking

new infections [6]. Investigating how a disease spreads in small populations, such as schools or workplaces, already poses significant challenges, and scaling these analyses to larger populations, such as entire cities, presents even greater difficulties. However, this challenge can be substantially mitigated by representing individuals as components of a network structure and their social interactions as links between them.

This network thinking perspective is not limited to epidemic spreading but extends to a broad variety of complex systems [7]. Such systems are characterized by emergence, in which the collective properties of the whole cannot be fully understood by examining only the individual components and their interactions [8]. One of the key advantages of modeling complex systems as networks is the extensive set of analytical tools available for studying their structure and dynamics [9, 10]. As a result, network science is distinguished by its strong interdisciplinarity, enabling applications in diverse fields such as medicine [11] and air transportation [12], as well as theoretical approaches, for example, in the investigation of critical phenomena [13, 14, 15].

In many cases, complex systems are described through time series analysis, in which correlations and other characteristics can be investigated using statistical models [16]. The variety of systems represented by sequences of time-ordered data ranges from natural phenomena [17] to financial systems [18]. This approach is also employed in biology, for instance, the ability to measure electrical activity in the brain through electroencephalogram (EEG) signals has brought advances in the study of epilepsy [19] and Alzheimer's disease [20]. Yet, starting from a time series and extracting information about the complex system that generated it, i.e., reverse engineering, can be challenging [21]. One promising approach to address this issue is the transformation of time series into networks [22]. Among various methods for doing so, the construction of visibility graphs (VG) has emerged as particularly promising [23]. This simple approach, based on geometric criteria of the time series, requires no parameters for its computation. Despite its simplicity, the method has proven highly effective in characterizing time series through network analysis. For example, fractal time series have been shown to map into scale-free VGs, whose degree distribution exponent can be related to the Hurst exponent of the original time series [24]. As a result, VGs have been applied across diverse fields, such as natural phenomena [25], EEG signals [26, 27], and, more recently, cardiac disorders [28]. This broad applicability drew our attention to the possibility of using VG to study spreading phenomena.

As previously mentioned, epidemic propagation is a relevant topic not only for developing management strategies but also from a theoretical perspective, particularly regarding phase transitions. This latter aspect was the key motivation for us to use VG to study synthetic time series of the number of infected individuals (prevalence) in spreading processes. Using simple spreading models such as the contact process (CP) [29] and the susceptible-infected-susceptible (SIS) model [30], we investigated the degree correlations of the VG constructed from prevalence time series. Among other results, we found that, for the CP model in homogeneous structures, the degree correlations of the VG serve as an effective measure for distinguishing between critical and off-critical regimes in spreading processes [31]. Additionally, we observed that strong localization in the underlying structure where the spreading occurs may obscure the critical signature of the transition [32].

Network thinking applied to spreading phenomena has provided several important insights into how diseases propagate through a substrate, for example, the ability to compute an epidemic threshold [33]. While static network approaches remain relevant in many respects, more realistic models that incorporate the temporal dimension have shown that static models tend to overestimate disease propagation [34]. Therefore, considering the structure in which a disease spreads as a temporal network can yield more accurate results [35]. Our social interactions are not homogeneous in time. For instance, a person may spend significantly more time with family and work colleagues than with the janitor of the building - heterogeneity that is not captured by static networks. However, considering a static backbone of contacts and implementing temporal dynamics on top of it can more accurately represent real-life interactions.

This approach was adopted in the present thesis, in which we simulated network temporality by intermittently activating nodes or links. When the dynamics of activation are applied to the links, we obtain a link-intermittent (LI) network, and when applied to the nodes, the result is a node-intermittent (NI) network. Both approaches were implemented using general renewal processes, where events (i.e., changes in the state of a link or node) follow an inter-event time distribution [36]. In principle, any distribution could be used for the inter-event times, but empirical data from several real-world systems suggest that activity often occurs in bursts [37]. For example, face-to-face interaction data from academic conferences [38] and high school environments [39] have been shown to follow power-law distributions of inter-event times. In this thesis, we simulated intermittent

dynamics on various contact backbone networks and demonstrated significant differences between the LI and NI approaches, among other results. Furthermore, by studying the SIS model on intermittent lattices, we raised the possibility of temporal Griffiths phases (TGP) [40] emerging as a result of intermittency.

Concepts of criticality and phase transitions permeate this thesis, as systems that one might initially think to be unrelated at first glance can exhibit the same critical behavior. The very act of thinking may be a manifestation of criticality in the brain, since phenomena such as consciousness have been shown to be associated with critical dynamics [41]. The idea of criticality in brain function has been extensively discussed over the years, and although its origins remain a subject of debate within the scientific community, strong evidence supports the critical brain hypothesis [42, 43, 44, 45, 46, 47, 48]. Understanding brain function is a highly interdisciplinary research field, and many questions remain open [49]. Beyond applied and health-related concerns, the brain may also be approached from a theoretical physics perspective, considering it operates near a critical point [50]. Among the various analyses related to brain criticality, one possible direction involves modeling individual neurons. In this context, rather than focusing solely on critical points, bifurcation points can also be investigated using low-dimensional models [51].

The present thesis is organized as follows. Chapter II begins by characterizing complex systems and extends the discussion of network thinking by introducing definitions, measures, and models of complex networks. Criticality and phase transitions are addressed in Chapter III, with a brief review of basic concepts in critical phenomena in equilibrium systems, followed by a focus on phase transitions in different models of spreading processes. These first two chapters provide the fundamental background for the results presented in Chapters IV and V. Additional methodological tools are included in the Appendices. This thesis is based on two main projects. The first is related to the use of visibility graphs (VG) to study spreading dynamics, discussed in Chapter IV. The second project, presented in Chapter V, explores an intermittent network approach to simulate the temporal heterogeneity of social interactions. A further contribution, not specifically related to networks but still connected to criticality, is the discussion of critical behavior in the brain, which is presented in Chapter VI.

II Network thinking of complex systems

> Network thinking will become essential to all branches of science as we struggle to interpret the data pouring in from neurobiology, genomics, ecology, finance, and the World Wide Web. Will theory be able to keep up?
>
> - Steven H. Strogatz [7]

P. Bak wrote in [52] that "the laws of physics are simple, but nature is complex". Physicists tend to adopt a reductionist approach to describe many natural phenomena. However, accounting for the interactions between simple components becomes increasingly challenging as the system size grows. The emergence of collective phenomena can be addressed by assuming a broader perspective when analyzing real systems. The coordinated behavior observed in ant colonies or bird flocks emerges without any central controller [8]. This exemplifies how self-assembling in real systems may play a role that would not be perceived only by analyzing the individual components. As a result, a different approach spanning multiple disciplines has been developed to understand complex systems ranging from societies to atmospheric dynamics.

One of the Latin roots of the word *complex* is *plectere*, meaning "to weave" or "to entwine" [53], reflecting that, in complex systems, simple individual parts are irreducibly interlaced. In this sense, we can view the components of a system as entwined or interconnected, as a network. Representing system components and their interactions as nodes and links has provided a new perspective on complex systems, where the main challenge lies in reassembling the elements that are well understood individually [7].

This chapter aims to present the key characteristics of complexity science, with an emphasis on network thinking as a powerful framework for studying complex systems. Additionally, it introduces basic metrics and techniques for network analysis, along with models for generating synthetic networks, highlighting the theoretical aspect of this thesis. These fundamental concepts will be applied throughout the subsequent chapters.

2.1 Characterizing complex systems

Although there is no universally agreed-upon definition of complex systems, examples are everywhere. From interactions between immune cells to Economy, complexity permeates our world in many ways [53]. As illustrated in Fig. 2.1, the existence of intricate forms of life, such as the human body, depends on cells, which depend on molecules, which are made up of atoms, and these are made of fundamental particles. However, when studying human behavior in society, we do not directly analyze how atoms are arranged within our bodies. This highlights that the reductionist approach is not always the most appropriate path to follow. This perspective is present in the celebrated 1972 article *More is Different* by P. W. Anderson [54], which discusses the limitations of the reductionist approach. Anderson argues that when dealing with large, complex systems, new properties and behaviors often emerge at the collective level, which cannot be fully understood by analyzing only the isolated interactions of the system's parts. Nevertheless, the 'More is different' concept is not the absolute opposite of reductionism since it is necessary to understand how the fundamental parts of the system interact with each other [8]. Thus, complexity science aims to find similarities in processes and emergent phenomena on different levels of organization [55].

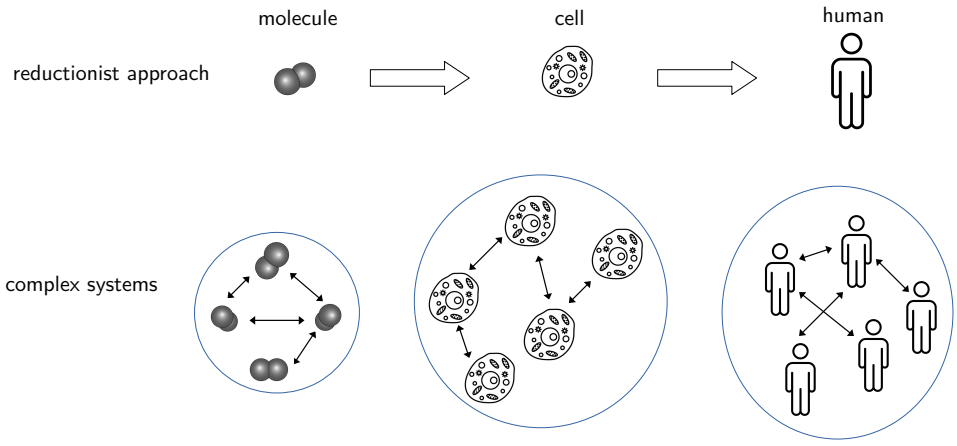

Figure 2.1 – Illustration comparing the reductionist approach to complexity. Different scales and levels of organization can exhibit similar emergent phenomena, allowing them to be treated as separate complex systems. For example, the collective behavior in large systems of molecules or in social interactions among people cannot be fully understood by analyzing only the individual components.

Recently, complex systems gained significant recognition with the awarding of the first Nobel Prize in this field in 2021. Half of the award was given to Syukuro Manabe and Klaus Hasselmann "for the physical modeling of Earth's climate, quantifying variability and reliably predicting global warming," and the other half was to Giorgio Parisi "for the discovery of the interplay of disorder and fluctuations in physical systems from atomic to planetary scales" [56]. It is interesting to note that, at first glance, spin glasses and Earth's climate appear to be very different systems. However, both can be understood as complex systems. Hasselmann and Manabe investigated how reliable climate models can be constructed despite the chaotic and short-term predictability of weather. Their work was also fundamental in understanding how human activity affects climate change through carbon dioxide emissions. Parisi's insights into hidden patterns in disordered structures, particularly in spin glasses, have applications extending from turbulence to starling murmurations.

The 2024 Nobel Prize in Physics, awarded to John Hopfield and Geoffrey Hinton, has also drawn global attention to the application of concepts from complex systems. The work of both laureates integrates ideas from condensed matter and statistical physics to develop technologies that use network structures for information processing [57]. Artificial neural networks lie at the heart of machine learning, where remarkable phenomena such as pattern recognition and memory emerge from the interaction of simple system components. Thus, the 2021 and 2024 Nobel Prizes testify to the vast applicability of complexity science.

Complexity takes ingredients from Physics, Biology, and Social sciences [58]. The predictive and quantitative aspects, along with the approach of formulating specific questions for experimental testing, are grounded in a physical point of view. Additionally, the strategy in physics of understanding macroscopic properties through statistical descriptions at the microscopic level is widely applied in complex systems. From Biology, complexity science inherits key concepts such as evolution, self-organization, self-replication, and adaptation. Meanwhile, Social Sciences contribute insights into collective behavior [53] and the tendency of components to form diverse **network structures**, which are fundamental for modeling and understanding real-world complex systems.

2.2 Basic notions and applicability of complex networks

Around the beginning of the eighteenth century, a curious puzzle intrigued the residents of Königsberg, the capital of Eastern Prussia: Could a person walk through the city, crossing each of its seven bridges exactly once [59]? Leonhard Euler, investigating this puzzle, wrote: "This question is so trivial, yet it seemed to me worthy of attention because neither geometry, nor algebra, nor even the art of counting was sufficient to solve it" [60]. Euler presented a solution to the seven bridges problem to the Petersburg Academy and published it one year later [61]. In this paper, Euler provided a necessary condition to solve the puzzle. He labeled the land areas with different letters and represented the bridges as lines connecting them, as illustrated in Fig. 2.2(a). He showed that no such path existed because, to cross each bridge only once, at least two land areas should have an even number of bridges. However, at that time, all land areas had an odd number of connections. The city, now called Kaliningrad, has changed over the years, with bridges being built and destroyed. Nevertheless, considering approximately the same area examined by Euler in 1735, the current arrangement of bridges allows a walk through them, crossing each one only once, as shown in Fig. 2.2(b). Despite the simplicity of its solution, this puzzle has a much more profound consequence: the representation of land areas as nodes and bridges as links. Moreover, the number of links at each node imposed a limitation on the possible paths. This brief historical episode is considered the birth of graph theory [10], which is the mathematical basis for complex networks.

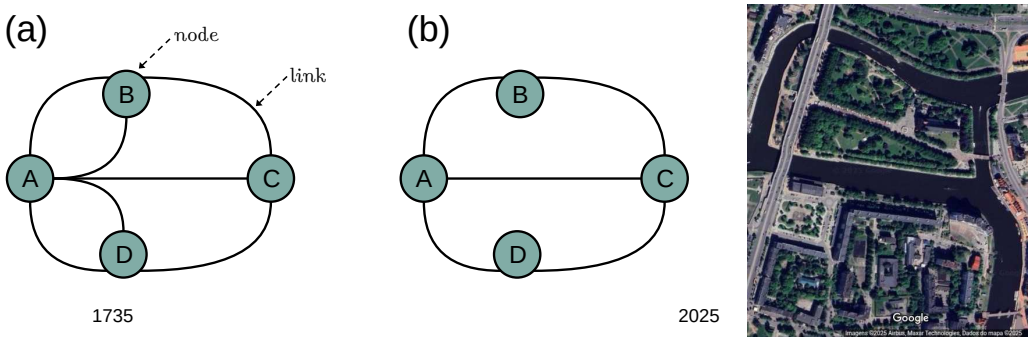

Figure 2.2 – Seven Bridges of Königsberg problem. Schematic arrangement of the bridges (links) and land areas (nodes). In (a), the one proposed by Euler in 1735, and in (b), the new possible configuration of bridges together with the present satellite view of the city that originated the puzzle, captured using Google Maps [62].

The possibility of identifying the components of a given system as nodes and their interactions as links had a strong impact on the way we analyze complex systems. As Network Science developed over the years, real systems in completely different scientific domains were discovered to have similar architectures, enabling the use of common tools to explore these systems [10]. To express the great diversity of systems that can be tackled using a network approach [9], let us name two examples.

- **Medicine:** The nodes in biological networks can represent various components, such as proteins, genes, RNA molecules, and even diseases. The links between nodes can correspond to protein–protein binding interactions or represent connections between diseases with a common genetic origin. If a protein has a large number of interactions, it is potentially encoded by essential genes. Moreover, considering diseases as nodes and the molecular relations between their associated cellular components can enhance the understanding of why certain groups of diseases occur together. Mapping these intricate biological interactions can also improve pharmacological strategies, advancing treatments by targeting specific components affected by drugs rather than merely addressing disease symptoms. Thus, the network approach may offer a forward-looking perspective on medicine [11].

- **Air transportation:** Our distances become shorter over the years, not only virtually, but also our physical distances have also seemed to shorten due to the possibility of traveling to distant places in just a few hours by plane. Air transportation networks can be constructed in different ways; for instance, the nodes can represent airports or the cities with airports, and the links generally correspond to the flights between them. Temporal networks can also be considered by analyzing how these connections change over given periods [12]. These networks are responsible for intense trading worldwide, but are also highly susceptible to failures and inefficiencies, such as flight delays, which incur large financial costs [63]. Understanding the properties of these networks can not only improve their efficiency but also enhance strategies for managing them during health emergencies, as they play an important role in the spread of infectious diseases [64].

These two examples are not directly related to the networks that will be treated in this thesis. Still, this illustrates the vast applicability of Network Science to distinct

areas, which is one of the reasons for the field's expansion in recent decades. Two systems with completely different motivations can be modeled as an abstract representative structure based on the same principle: nodes and links [10]. Therefore, to fully embrace the interdisciplinary potential of the network approach, the theoretical foundations must be strong, with continuous development of new methods for network analysis. Returning to the chapter's opening quotation, as the available data sets increase in quantity and quality, it is important not only to understand the techniques but also to come up with new ones for handling them.

Therefore, the approach for networks in this text is mostly theoretical, using synthetically generated networks to understand the interdependence of structure and dynamics in these systems. Thus, this chapter aims to provide methodological and conceptual support for the following chapters, presenting networks of different kinds and analysis tools.

2.3 Metrics for static structures

A graph can be defined as a set of vertices connected by edges [9]. The word graph may be used as a synonym for the word network, but more generally, a graph is a mathematical representation of a network, in which nodes and links stand for specific real objects, as mentioned above in the examples.

A simple graph does not contain self-loops or multiple links, and it can also be classified according to the characteristics of the links as undirected/directed and weighted/unweighted. Networks can be mathematically represented by an adjacency matrix A_{ij} with size $N \times N$, in which N is the number of nodes or network size. This matrix contains all the structural information of the network since if $A_{ij} = 1$, there is a link between the nodes i and j, and $A_{ij} = 0$ otherwise. All networks considered in this thesis are undirected, which have a symmetric adjacency matrix, i.e., $A_{ij} = A_{ji}$. If the links have weights, this information can also be encoded in the adjacency matrix. For instance, if nodes i and j share a link with weight w_{ij}, it can be written as $A_{ij} = w_{ij}$.

Fig. 2.3 shows an example of simple networks with their corresponding adjacency matrices. Panel (a) in this figure shows a matrix with almost all entries equal to one since it is a fully connected graph. Also, the diagonal is zero because there are no self-connections. This network was built using my Google Scholar page [66]. The platform

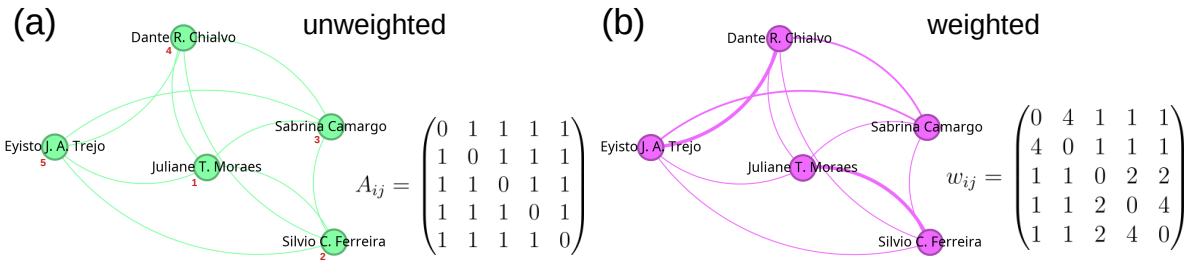

Figure 2.3 – My Google Scholar scientific collaboration network with connections up to first neighbors. Panel (a) is an unweighted version, considering only the existence of collaboration. Panel (b) shows the weighted links accounting the number of papers on which the two nodes have collaborated. Gephi software was used for network visualization [65].

contains information on scientific publications, citations, and coauthors. Thus, the links between the nodes exist if they co-authored research papers. A weighted version of this network is shown in panel (b), considering the number of papers in which two persons are coauthors. For simplicity, only unweighted networks will be addressed in the remainder of the text.

An important metric to consider is the number of links each node has, named degree k. For a given node i it can be computed as

$$k_i = \sum_{j=1}^{N} A_{ij} \ . \tag{2.1}$$

The average degree for the nodes in a network $\langle k \rangle$ is then

$$\langle k \rangle = \frac{1}{N} \sum_{i=1}^{N} k_i \ . \tag{2.2}$$

Networks in which all nodes have the same degree are called homogeneous. For structures having a diversity of degrees (heterogeneous), the average degree may be representative or not, depending on the degree distribution, which will be discussed further in the sequence of this chapter.

The total number of links in the network (ℓ) can be determined as

$$\ell = \frac{1}{2} \sum_{i=1}^{N} k_i = \frac{N \langle k \rangle}{2}. \tag{2.3}$$

Note that the factor 1/2 accounts for undirected networks, where each link will appear twice in the adjacency matrix. The density of a network can be analyzed by the maximum number of links it would have if fully connected

$$\ell_{\max} = \binom{n}{2} = \frac{1}{2}N(N-1) \ . \tag{2.4}$$

If $\ell \ll \ell_{\max}$, the density of links is low, and the network is sparse [9]. Most real networks are sparse, and so are their adjacency matrices. This will generate many zero entries, making the representation of the networks as square matrices computationally inefficient. An optimization for the storage of the connections using adjacency lists is discussed in Appendix A.

Although physical distance can be relevant in some applications, it is often not considered when analyzing networks. Instead, the distance between two nodes can be measured in terms of paths. The length of a path is defined as the number of links that must be crossed to move from one node to another, passing by the path. The distance is the shortest possible path, denoted by d_{ij}. The average path length $\langle d \rangle$ is the average over all distances d_{ij} for all pairs of nodes (i, j), given by

$$\langle d \rangle = \frac{1}{N(N-1)} \sum_{\substack{i,j=1,N \\ i \neq j}} d_{ij} \ , \tag{2.5}$$

in which the set containing all distances can be computed using a Breadth-First Search algorithm [9]. This algorithm starts from an initial node and labels the other ones with the distances to it. After repeating the labeling process for all nodes, the distances between any given two nodes in the network will be known. This also allows the computation of the longest shortest path in the network, known as the diameter $d_{\max}$ [10].

If we think of a square lattice, the distance between two nodes scales with the lattice width, i.e. $\langle d \rangle \sim N^{1/2}$. As will be discussed in Sec. 2.4, random networks are characterized by small $\langle d \rangle$, and it has important consequences in network analysis. Let us consider a more complex case, using the scientific collaboration connections of my advisor, Silvio C. Ferreira, as an example. It is an illustrative network that was generated by extracting data from the HTML source code of the Google Scholar webpage. Some links are missing, since the platform does not always display all coauthors. Also, the

network is truncated at the next-nearest neighbors of the initial node. Even so, it is possible to analyze the generated network, which is shown in Fig. 2.4 and has $N = 716$, $\ell = 859$, and $\langle k \rangle = 2.4$. Concerning the paths, the network has a diameter of $d_{\max} = 4$, and the average distance between two random nodes is only $\langle d \rangle = 3.53$. Additionally, Fig. 2.4 was generated using the software VOSviewer [67], which condenses the nodes with degree $k = 1$ in the network to improve visualization. Thus, the red arrows in this figure indicate that these nodes, which appear to have multiple links, are actually many unit-degree nodes drawn together.

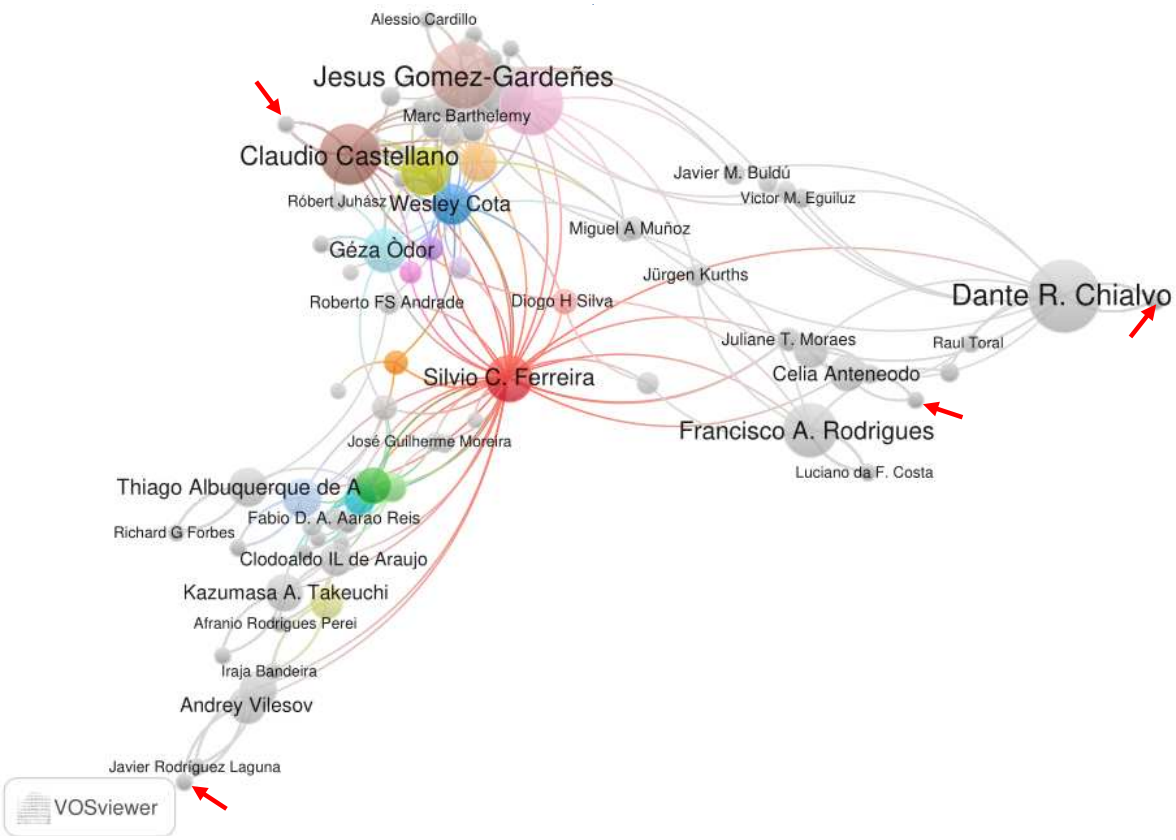

Figure 2.4 – Unweighted network built on Google Scholar scientific collaborations, with connections up to next-nearest neighbors of Silvio C. Ferreira. Colored nodes have the highest number of triangles. Node sizes are related to degrees. Red arrows indicate the condensations of nodes with unit degree. VOSviewer software was used for network visualization [67].

The probability p_k that a randomly chosen node has degree k is named the degree distribution. It is given by $p_k = N_k/N$, in which N_k is the number of nodes having degree k in the network. Considering a continuous approximation, the normalization condition

can be rewritten as

$$\int_{k_0}^{k_{\max}} P(k)dk = 1 \ , \tag{2.6}$$

which gives the normalized degree distributions. For nodes having degree between k_0 and $k_{\max}$ [10], the moments of the distribution are

$$\langle k^n \rangle = \int_{k_0}^{k_{\max}} k^n P(k)dk \ . \tag{2.7}$$

The first moment ($n = 1$) is the average degree, and the second $n = 2$ is used to calculate the variance $\sigma^2 = \langle k^2 \rangle - \langle k \rangle^2$. These two quantities establish a range in which the degree has a non-negligible probability of happening, giving a scale to the network. For instance, in the limit $\langle k \rangle \ll N$ of sparse networks, the degree distribution can be approximated by the Poisson distribution given by

$$P(k) = e^{-\langle k \rangle} \frac{\langle k \rangle^k}{k!} \ , \tag{2.8}$$

whose standard deviation is $\sigma = \langle k \rangle^{1/2}$. This means that random networks following this distribution have a characteristic scale.

However, if the network has a degree distribution following a power law, i.e., $P(k) = Ak^{-\gamma}$, the scenario changes. Let us analyze the moments of this distribution using Eq. (2.7), which gives

$$\langle k^n \rangle = \frac{A}{n - \gamma + 1}(k_{\max}^{n-\gamma+1} - k_0^{n-\gamma+1}) \ . \tag{2.9}$$

Note that the second term $k_0^{n-\gamma+1}$ is always finite since k_0 is a constant. Yet, taking the limit $N \to \infty$, the first term may diverge as $k_{\max} \to \infty$ depending on n and γ. The moments are finite for $n < \gamma - 1$, but diverge for $n \geq \gamma - 1$, meaning that for a network with exponent $2 < \gamma \leq 3$, the mean degree $\langle k \rangle$ can be computed, but it does not determine a scale since the variance diverges as $\langle k^2 \rangle \to \infty$. Thus, for these networks, the range of variation for the degree of a randomly chosen node is arbitrarily large. It is worth noticing that it is not strictly necessary that the network size is infinite. For finite large networks, the variance is not infinity, but if $\sigma \gg \langle k \rangle$, it will result that $\langle k \rangle$ does not represent a meaningful scale.

In the late 90s, one seminal example of a real network following a scale-free distribution was found in the network of documents in the World Wide Web that exhibited a power-law degree distribution with an exponent of $\gamma = 2.45$ [68]. Several other real networks were shown to display the same property [69] rather than the Poisson distribution frequently found in random graph theory at that time. This discovery marked an important milestone in network science, as this power-law architecture has a strong impact on dynamical processes, as will be discussed in Ch. III.

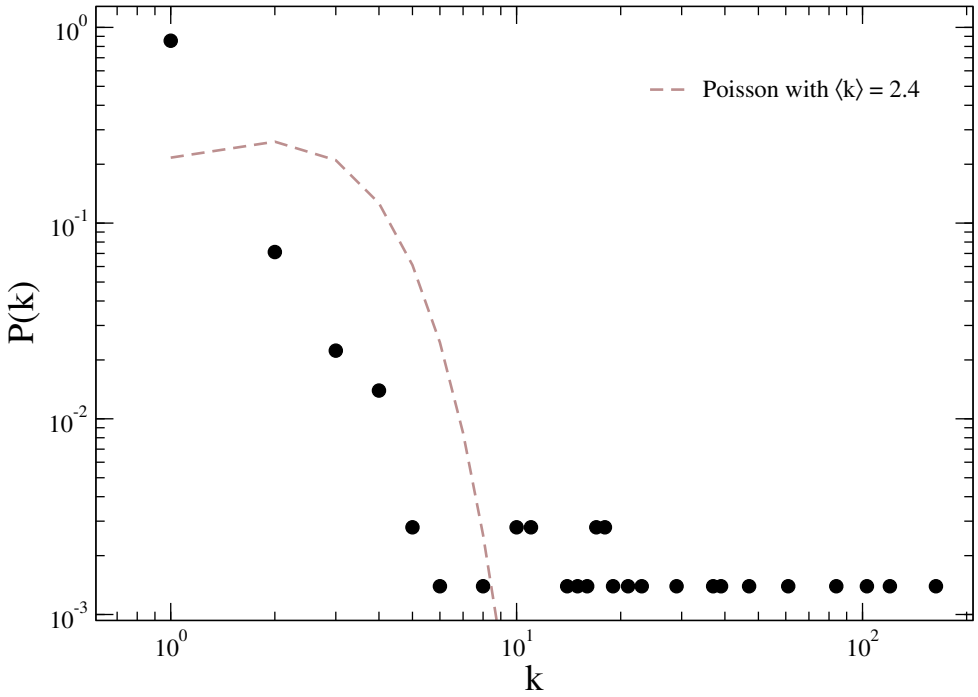

Figure 2.5 – Degree distribution for the collaboration network of Fig. 2.4. The dashed line corresponds to the curve generated from Eq. (2.8) using the average degree of the network.

The degree distribution of the network in Fig. 2.4 is shown in Fig. 2.5. Although a power law curve can not be accurately fit in this figure, it visibly deviates from the Poisson distribution. Also, at the tail of the distribution, some highly connected nodes are shown. These nodes are called hubs and have degree $k_{\text{hub}} \gg \langle k \rangle$.

Concerning the organization of the network, some questions may arise. For instance, how many of Silvio's coauthors have collaborated? This question can be answered by computing the local clustering coefficient given by

$$c_i = \frac{2\ell_i}{k_i(k_i - 1)} \ , \tag{2.10}$$

in which ℓ_i is the number of pairs of neighbors of node i that are connected, and $k_i(k_i-1)/2$

is the number of possible links between the neighbors of this node [9]. Silvio has a degree $k_i = 37$, and their neighbors have 56 links, meaning that his node in the network has 56 triangles. Thus, its clustering coefficient is $c_i = 0.084$, meaning that for two coauthors of Silvio randomly chosen, there is a probability of 8% that they have already collaborated.

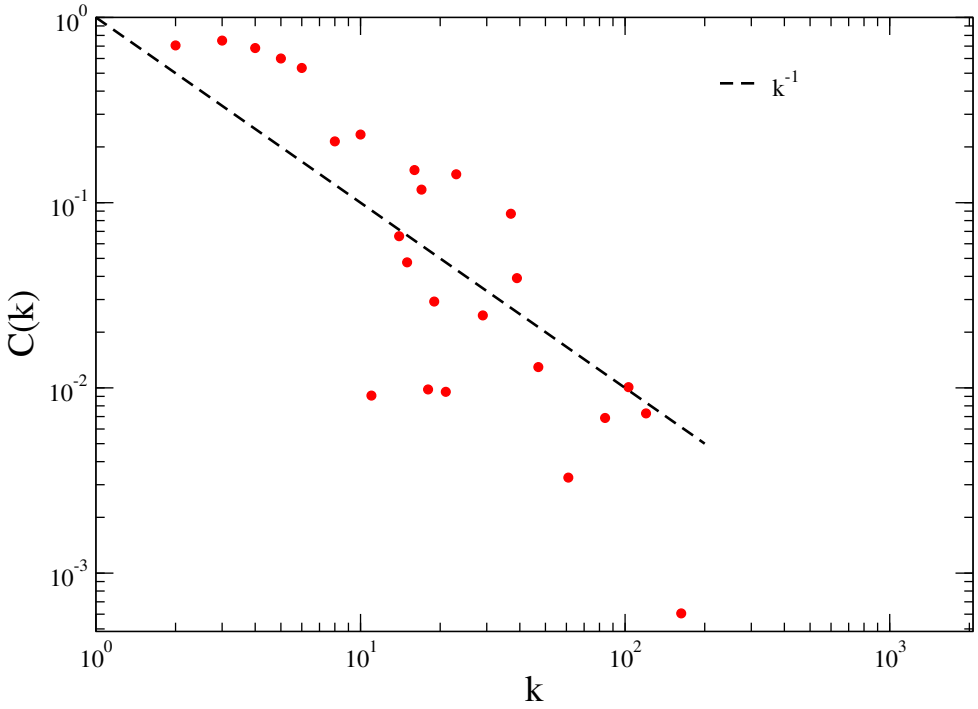

Figure 2.6 – Clustering coefficient as a function of degree for the collaboration network of Fig. 2.4. The dashed line is a guide to the eye for the decreasing pattern of the clustering.

The average clustering of the whole network can be computed by summing up c_i for all nodes and dividing by N. The network presented in Fig. 2.4 has $\langle c \rangle = 0.56$. Another analysis for the whole network is the global clustering coefficient as a function of degree, which can be computed using

$$C(k) = \frac{1}{N_k} \sum_{i=1}^{N} c_i \delta_{k,k_i} \ . \tag{2.11}$$

This quantity is plotted in Fig. 2.6 for the collaboration network. It is related to the community structure of the network: nodes with low degree tend to have high clustering because they belong to densely connected subgraphs (communities). In contrast, nodes with low clustering and high degree are more connected across different communities than within a specific one.

Another analysis is the degree correlations of the network, measured by the average degree of the nearest neighbors as

$$K_{nn}(i) = \frac{1}{k_i} \sum_{j=1}^{N} A_{ij} k_j \ . \tag{2.12}$$

To analyze how this quantity varies as a function of the degree, we compute

$$K_{nn}(k) = \frac{1}{N_k} \sum_{i=1}^{N} K_{nn}(i) \delta_{k,k_i} \ . \tag{2.13}$$

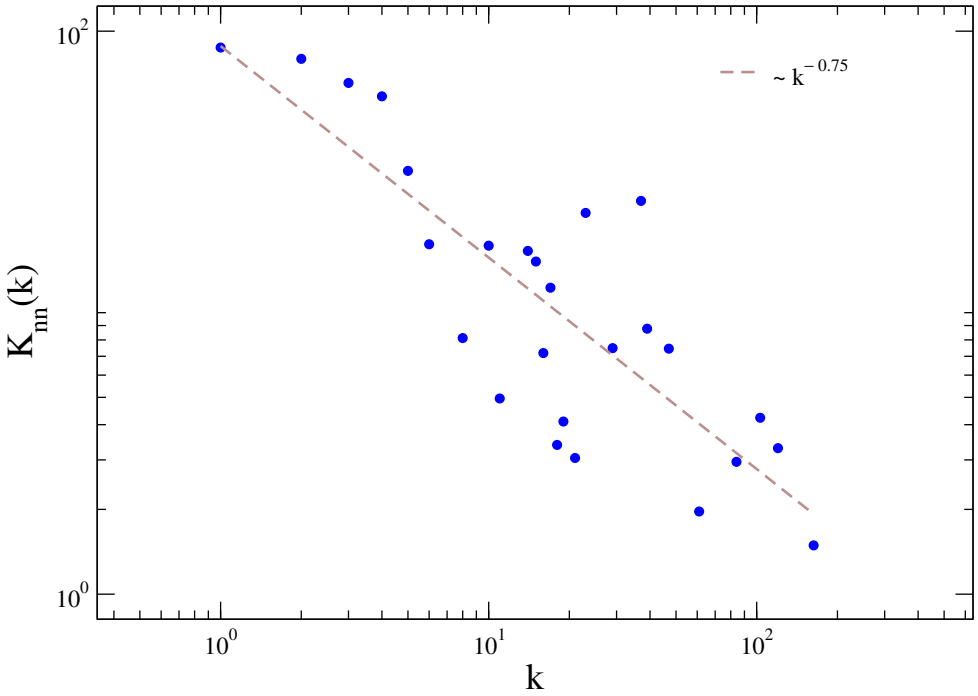

Figure 2.7 – Average degree of the nearest neighbors as a function of degree for the collaboration network of Fig. 2.4. The dashed line is a power-law regression for the data points.

The average degree of the nearest neighbors as a function of degree is shown in Fig. 2.7 for the network of Fig. 2.4. In this figure, a power-law regression to a power-law $K_{\rm nn}(k) \sim k^{\mu}$ leads to $\mu = -0.75$. The $K_{\rm nn}(k) \sim k^{\mu}$ scaling has already been observed in many real networks [70] and the exponent μ will dictate the degree correlations of the network: if $\mu > 0$, the network is assortative, meaning that nodes of similar degree tend to be connected; if $\mu < 0$, the network is disassortative meaning that low degree nodes tend to connect to high degree ones. The network will present neutral degree correlations if $\mu \approx 0$.

There is still a possibility of characterizing the degree correlations through a single number, the Pearson correlation coefficient, also called the assortativity coefficient r [71]. To build an expression for r, first we must consider the matrix e_{ij} as the probability of finding nodes with degrees i and j at the ends of a link selected at random [10]. Also, we must take into account the probability that there is a degree-k node at the end of a randomly selected link, given by $q_k = kp_k/\langle k\rangle$. So, uncorrelated networks will simply lead to $e_{ij} = q_i q_j$. However, if the network presents degree correlations, e_{ij} will deviate from this expression, and the deviation can be computed using $\sum_{jk} jk(e_{jk} - q_j q_k)$. For a perfectly assortative network we have $e_{jk} = q_k \delta_{jk}$ and this value is equal to the variance $\sigma^2 = \sum_k k^2 q_k - (\sum_k k q_k)^2$ of the distribution q_k. These expressions lead to a normalized relation that is the Pearson correlation coefficient, given by

$$r = \frac{1}{\sigma^2} \sum_{jk} jk(e_{jk} - q_j q_k). \tag{2.14}$$

Thus, the values of r will be in a range $[-1, 1]$, with $r > 0$ ($r < 0$) signaling an assortative (disassortative) mixing, and $r \approx 0$ representing the uncorrelated case, so the sign of r has the same meaning as for μ. For instance, Silvio's collaboration network of Fig. 2.4 has $r = -0.52$, which indicates disassortative correlations. However, it is not a common characteristic for this type of network, since collaboration networks are, in general, assortative [10]. This happens because, for building the network, nodes were truncated up to Silvio's next-nearest neighbors, so the neighbors of these coauthors are generally nodes of unit degree.

2.4 Modeling networks

This section aims to present some important models for generating synthetic networks that will be used in many instances in the remainder of the text.

Lattices

In terms of a graph, a lattice is a strictly homogeneous structure. For simple hypercubic graphs, nodes have $2D$ neighbors in D dimensions. In all cases in this text, the lattices are considered to have periodic boundary conditions so that the graph is

connected and all the vertices have the same number of edges. Fig. 2.8 (a) shows an example of a square lattice. The size of the lattice is always related to the width L as $N = L^D$. Despite the simplicity, this structure has relevance in the study of both equilibrium and non-equilibrium phase transitions [4].

Erdős-Rényi networks and the small-world effect

Random graph theory was extensively investigated by P. Erdős and A. Rényi through a series of papers starting from 1959 [72]. Random networks can be constructed using two models that lead to the same properties [73]. The first model, introduced by Erdős and Rényi, defines a random graph $G(N, \ell)$ as consisting of N vertices and a fixed number ℓ of edges. The second model considers $G(N, p)$, where any pair of vertices is connected with probability p. The latter version of the random network model has a simpler implementation, and its properties are more straightforward to analyze. It was introduced independently of the Erdős and Rényi studies by E. N. Gilbert [74]. Following the terminology used in important network textbooks such as [10], throughout this text, random graphs generated using $G(N, p)$ will be referred to as Erdős-Rényi (ER) networks, with an example shown in Fig. 2.8(b).

One interesting property of random networks is that the distances can be small. If we consider that $\langle k \rangle$ nodes are at distance $d = 1$ from each other, $\langle k \rangle^2$ at distance $d = 2$, and so on. So if we start from a given node in the network, the expected number of nodes up to distance d from it would be $N(d) = 1 + \langle k \rangle + \langle k \rangle^2 + ... + \langle k \rangle^d$, leading to a geometric sequence for the number of nodes at distance d given by

$$N(d) = \frac{\langle k \rangle^{d+1} - 1}{\langle k \rangle - 1} \ . \tag{2.15}$$

However, this number of nodes is constrained by the network size N, so that $N(d_{\max}) \approx N$. If we consider a well connected network, meaning that $\langle k \rangle \gg 1$, Eq. (2.15) reduces to $\langle k \rangle^{d_{\max}} \approx N$, which would lead to $d_{\max} \approx \ln(N)/\ln(\langle k \rangle)$. Yet, for several real network data, the previous expression offers a better agreement to $\langle d \rangle$ rather than $d_{\max}$ [10]. Thus, we have $\langle d \rangle \approx \ln(N)/\ln(\langle k \rangle)$ and this relation between $\langle d \rangle$ and $\ln(N)$ is known as the small-world property, which is present in many important real systems, such as the brain networks [75].

The 'small-world problem' was discussed in 1967 by S. Milgram [76], describing a social experiment in which people were supposed to send letters to specific targets in the US. Most messages reached their target with a median of 5 letters, meaning that, on average, participants in the experiment were separated by a very small number of connections.

Cohen *et al* showed that hubs can play an important role in decreasing the distances in networks [77]. Therefore, for random power-law degree distributions with exponent $2 < \gamma < 3$, the average path length follows $\langle d \rangle \sim \ln[\ln(N)]$, which can be interpreted as an ultra-small world property of the scale-free networks.

Uncorrelated configuration model

Although real networks may exhibit degree correlations, from a theoretical perspective, it can be convenient to use uncorrelated networks. Thus, the uncorrelated configuration model (UCM) is a method to generate networks with a given degree distribution while avoiding degree correlations [78]. Basically, the model starts by assigning to each node a given number of stubs defined according to the degree distribution, and these stubs are then connected at random. By introducing a structural cutoff for the degrees in the network as $k_c = (\langle k \rangle N)^{1/2}$, the probabilities of self-loops and multiple links become negligible, while degree correlations are suppressed [79]. The computational details of the implementation of this model are discussed in Appendix A.

Assuming a degree distribution $P(k) = \delta(k-m)$, the UCM can be used to generate a random network in which all nodes have degree $k = m$, named random regular networks (RRN). An example of this network is shown in Fig. 2.8 (c) for $N = 8$ and $m = 4$.

Star graphs, as shown in Fig. 2.8 (d), mimic the configuration of the hubs, where a central node is connected to many neighbors (the leaves). This structure can be analyzed separately from the whole network, providing insightful characteristics of epidemic spreading on networks, as will be discussed in Ch. III.

To generate networks containing hubs, one possible degree distribution is $P(k) = Ak^{-\gamma}$. Since in this thesis we do not use other types of distributions to generate power-law degree distributed networks, these will be referred to as "UCM networks" in the remainder of the text. An example of a UCM network with exponent $\gamma = 2.75$ is shown in Fig. 2.8 (e). It is interesting to note that in Fig. 2.8, both the ER (b) and UCM (e) networks

have the same size, $N = 50$. However, in the first case, all nodes have similar degrees, whereas in the power-law case, the hubs are significantly more connected than the other nodes of the network.

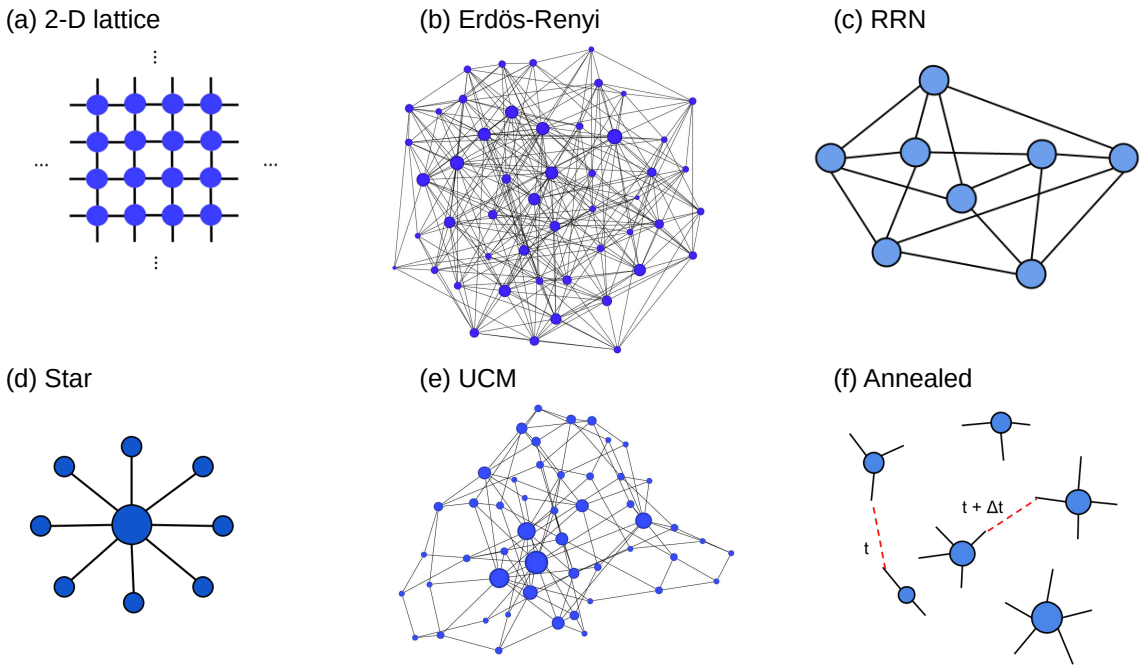

Figure 2.8 – Illustration of networks generated from different models. (a) Square lattice of width $L = 4$. (b) Erdős-Renyi network with $N = 50$, $p = 0.25$, $\ell = 288$, and $\langle k \rangle = 11.52$. (c) Random Regular Network with size $N = 8$ and $k = 4$. (d) Star graph with 8 leaves. (e) Power-law degree distributed network generated using UCM with size $N = 50$, $\gamma = 2.75$, $\ell = 118$, and $\langle k \rangle = 4.72$. (f) Examples of possible links in an annealed network. The sizes of nodes are related to their degrees in all panels.

Annnealed networks

The aforementioned networks are quenched, in the sense that their connections do not change in time. The opposite behavior happens if the connections are completely reshuffled between any two steps of the dynamics occurring on the network. If this occurs while maintaining the degree distributions and correlations, this is called the annealed network approach [80]. An illustration of connections being made in different time steps for annealed networks is shown in Fig. 2.8 (f).

If the links in quenched networks are described by an adjacency matrix A_{ij}, for annealed networks it is replaced by the ensemble average $\overline{A}(k_i, k_j)$. Thus, for uncorrelated

networks, the probability that two vertices of degree k and k' are connected is [81]

$$\overline{A}(k,k') = \frac{kk'}{N\langle k\rangle} \ . \tag{2.16}$$

As this approach is based on a predefined degree distribution and connections are only probabilistic, it is not considered a temporal network in this text. Despite its simplicity, annealed networks are very important from a theoretical perspective, as some mean-field methods become exact in this approach.

2.5 Concluding remarks

In summary, this chapter presented the idea of networks as playing a central role in the study of complex systems. Basic quantities and simple measures were explored, along with models for generating synthetic networks. The concepts and definitions introduced here will be important throughout the remainder of this thesis, as we aim to investigate dynamical processes occurring on network structures. Additionally, the relationship between dynamics and structure will be examined, particularly in terms of how it can alter the critical behavior of systems.

III Critical phenomena and phase transitions

> Living systems need to achieve a trade-off between robustness and flexibility. An optimal balance between these two conflicting tendencies can be accomplished by keeping the system dynamical state at the borderline of an order-disorder phase transition, i.e., at criticality.
>
> - Miguel A. Muñoz [82]

Strong evidence supports the hypothesis of a critical brain [83]. Criticality also manifests across various domains of biology. Large-scale structural patterns and collective functions, such as tumor growth and bacterial biofilm formation, emerge as properties arising from the interaction of groups of cells [84]. Similarly, the collective motion observed in flocks of starlings exhibits long-range, scale-invariant correlations, suggesting self-organization as a mechanism for achieving coordination [85]. Although these examples are drawn from living systems, the opening sentence provides a broader perspective on criticality: a state poised between order and disorder.

Examples of systems exhibiting critical behavior are found across diverse domains, including economics. For instance, stock market price fluctuations have been shown to lack a characteristic scale, a hallmark of self-organized criticality [86]. Moreover, features such as phase transitions and universality are also observed in various social systems, including opinion and language dynamics, crowd behavior, and the formation of hierarchies [87].

Spreading phenomena represent an important area of investigation related to criticality [5]. Epidemic models such as the contact process (CP) [29] and the susceptible-infected-susceptible (SIS) model [30] are examples that exhibit absorbing state phase transitions (ASPT) in the thermodynamic limit. These models provide a framework to explore a broad range of criticality concepts through finite-size scaling analysis. Accordingly, this chapter will address spreading phenomena by analyzing the CP model and two of its modifications, each leading to distinct phase transitions. In addition, the SIS model will be employed to investigate how network structure influences the activation mechanisms driving the transition. To provide the necessary background, the chapter begins with a review of primary concepts related to phase transitions, such as long-range correlations, symmetry breaking, and scale invariance. Although these terms are typically discussed in the context of equilibrium systems, they can be adapted to study non-equilibrium scenarios as well.

3.1 Critical phenomena

From a historical perspective, the earliest manifestations of criticality concepts, as we understand them today, emerged when studying systems in thermodynamic equilibrium. Over sufficiently long periods, a system tends to evolve toward an equilibrium state, which is past independent and can be fully described by macroscopic variables such as energy, volume, and number of constituting particles [3]. These variables are called extensive since they scale with the size of the system. On the other hand, variables such as the temperature that remain constant regardless of changes in system size are called intensive.

Pierre Curie, in his PhD thesis *Propriétés magnétiques des corps à diverses températures* [88], investigated how the magnetization of a given material changes as the temperature is varied. A framework for these experimental observations is illustrated by the Ising model, which has a rich critical behavior in equilibrium. The Hamiltonian for the nearest-neighbor Ising model in the absence of an external field is

$$\mathcal{H} = -J \sum_{\langle i,j \rangle} \sigma_i \sigma_j \ , \tag{3.1}$$

in which $J > 0$ is a coupling constant that accounts for the ferromagnetic interactions and $\langle i, j \rangle$ represents the summation over only nearest neighbor spins [89]. Considering the spins to be arranged on a square lattice[1] of size $N = L \times L$, each of which can assume one of two possible states: $\sigma_i = 1$ if the particle has spin up ($\uparrow$), and $\sigma_i = -1$ if it has spin down ($\downarrow$)[2]. The magnetization per particle m of the system is defined as [2]

$$m = \frac{1}{N} \left| \sum_i \sigma_i \right|. \tag{3.2}$$

Following Curie's experimental observations, there is no defined magnetization when the material in thermodynamic equilibrium is at high temperatures. Thus, there is no direction for the spins to point at, meaning that the system is isotropic and symmetric [91]. If the temperature is slowly decreased, below a specific value T_c, the material responds by choosing a magnetic orientation, and the original **symmetry is sponta-**

[1] This two-dimensional version of the Ising model was analyzed by Lars Onsager, and its exact solution was published in 1944 [90].

[2] The terms *up* and *down* refer to the intrinsic orientation of the particle's angular momentum.

neously broken. In this sense, it is possible to associate magnetization with an indicator of the system's organization, or more technically, an indicator of order. The concept of **order parameter** was introduced in Landau's theory [92], where the deviation from the Hamiltonian symmetry determines the degree of order in the system. In this framework, the isotropic configuration represents a disordered state, while an ordered state emerges as the temperature decreases below a specific value, $T = T_c$, known as the **critical point**, and Fig. 3.1(a) illustrates these concepts. This change in the system's state, or the phase, is called **phase transition**. Following modern terminology, the paramagnetic–ferromagnetic transition is continuous, also called a second-order phase transition in the former classification [2]. The term "continuous" came from the fact that the free energy is a continuous function of parameters even at the critical point [1]. The phase transition in the Ising model is a result of the competition between energy and entropy: energy tends to make the spins align, and entropy leads to spin disorder [3].

To simulate the phase transition present in the Ising model, we can use the Glauber dynamics [2], which is explained ahead in the present section. Through simulations, we can compute the average magnetization as a function of temperature for different system sizes, as shown in Fig. 3.1(b). In this panel (b), it is possible to observe that as the size of the system increases, the phase transition behavior looks more similar to the one illustrated in panel (a). Finite systems will always have size effects, since the transition occurs only in the thermodynamic limit as $N \to \infty$.

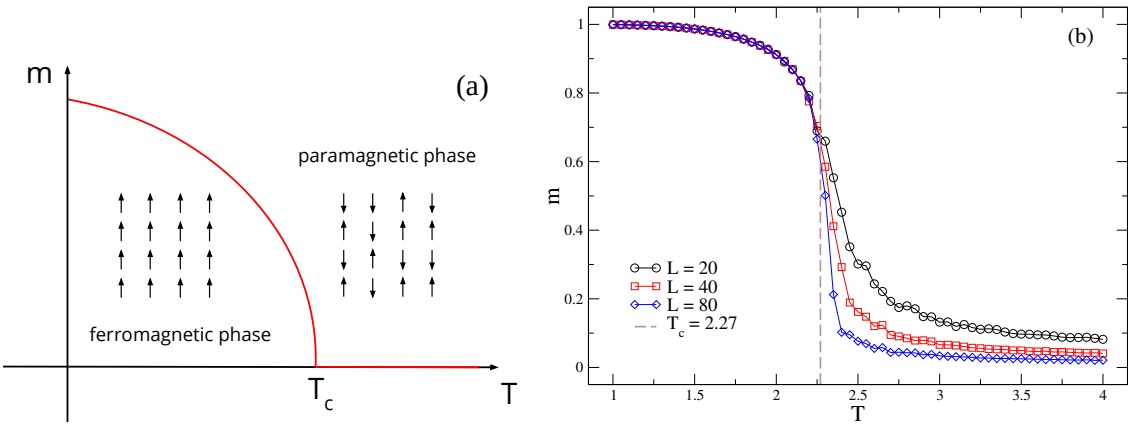

Figure 3.1 – Paramagnetic-ferromagnetic phase transition. As the temperature decreases below T_c, symmetry is broken, resulting in a non-zero magnetization (m). (a) Schematic illustration. (b) Curves simulated through the Glauber dynamics using 5.10^3 Monte Carlo steps for computing the average magnetization and 10^4 steps for thermalization.

In the Ising model, interactions occur only between nearest-neighbor spins, mediated by the coupling constant J. However, as the system temperature decreases, below the critical point, a collective phenomenon emerges and spins far from each other in the lattice become ordered. Yet, for temperature values near the critical point, the system becomes long-range correlated. To better understand this, let us analyze the correlation between any two spins in the lattice given by

$$C(\mathbf{r}_1, \mathbf{r}_2; T) = \langle \sigma_1 \sigma_2 \rangle - \langle \sigma_1 \rangle \langle \sigma_2 \rangle \ , \tag{3.3}$$

where $\mathbf{r}_1$ and $\mathbf{r}_2$ are positions of the sites 1 and 2. As the system under consideration exhibits translational and rotational invariance, the correlation function depends only on the distance $r = |\mathbf{r}_1 - \mathbf{r}_2|$. Thus, far from criticality, the correlation function decays as

$$C(r; T) \sim r^{-\vartheta} e^{-r/\xi} \ , \tag{3.4}$$

meaning that in the off-critical regimes, the correlation between spins decays fast, exponentially. For the two-dimensional Ising model, $\vartheta = 2$ above and $\vartheta = 1/2$ below the critical point [2]. The exponential decay is controlled by the correlation length ξ, which depends on the temperature. The correlation length gives a measure of the distance over which spins are correlated [3]. At criticality, the correlation function exhibits a power-law decay given by

$$C(r; T) \sim r^{-d+2-\eta} \ , \tag{3.5}$$

meaning that at the critical point the system exhibits **long-range correlations**. This can also be expressed by defining a reduced temperature $\tau = (T_c - T)/T_c$. Thus, for $T \to T_c$

$$\xi \sim |\tau|^{-\nu} \ , \tag{3.6}$$

demonstrating that in the vicinity of the critical point, the correlation length diverges. The exponents η and ν are called **critical exponents** [2], and will be discussed later.

With the correlation length diverging at the critical point, clusters of aligned spins of all sizes arise in the system, as shown in Fig. 3.2. To better understand this, we could imagine an ocean of up spins, where there are continents of down spins, which in turn enclose lakes of up spins, and so on, with all length scales appearing. That is, fluctuations occur at every possible scale, making the system **scale invariant** at the critical point [3].

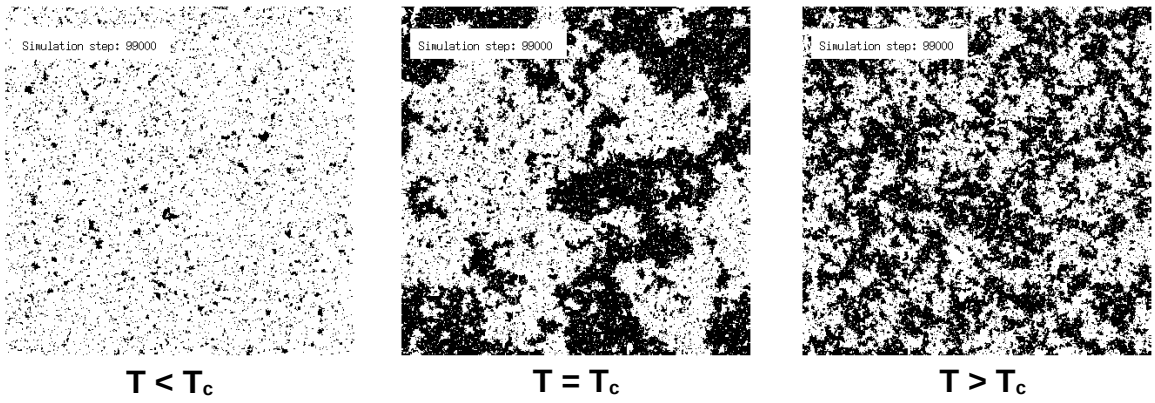

Figure 3.2 – Two-dimensional Ising model in a square lattice of size $L = 400$. Simulation of the model using Glauber dynamics for different temperatures. The material in low temperatures (left panel) tends to an ordered phase, with defined orientations for almost all spins. While for temperatures $T > T_c$, the spins are in a disordered phase, with no preferred magnetization. At the critical point, spin clusters of all sizes are present.

The possibility of computing critical exponents[3] for different systems is a hallmark of the study of phase transitions. Quantities such as the critical temperature T_c are highly sensitive to the details of the interactions. However, the critical exponents are independent of microscopic details and depend solely on a limited set of characteristics, such as the system's dimensionality and symmetries [2]. This led to the universality hypothesis, which simplifies the wide range of critical phenomena into a limited number of categories, known as **universality classes**, determined by only a few essential features. All systems within a specific universality class share the same critical exponents, as observed experimentally in many real systems [1].

The behavior of individual spins and their interactions can provide explanations at the microscopic level. However, considering only each component of the system does not explain why it adopts a specific phase, such as a preferred magnetization at the critical point. This happens because interactions between many agents give rise to new behavior at the collective level, and this property is called **emergence** [55].

These concepts in criticality originated in the domain of equilibrium systems. However, they can be extended, with appropriate modifications, to non-equilibrium systems and are also observed in real data [82]. To understand the non-equilibrium concept, we

[3] Other critical exponents will be addressed in more detail in Section 3.2.4.1, using an example of a non-equilibrium phase transition.

need to define the condition of detailed balance. Let us consider two possible microstate configurations of spins, σ and τ, and let $P(\sigma, t)$ and $P(\tau, t)$ be the probabilities of finding these respective configurations at time t. To allow the spin configurations to evolve in simulations, we may use a simplified dynamics in which a single spin is updated at each time step, called Glauber dynamics[4] [2]. The rates between the two possible configurations can be chosen by adopting different stochastic algorithms. In this thesis, for generating Fig. 3.2 and the curves in Fig. 3.1(b), we chose the Metropolis algorithm, introduced by Metropolis *et al.* in [93], which is given by the rates

$$w(\tau \to \sigma) = \begin{cases} \exp(-(\mathcal{H}[\{\sigma\}] - \mathcal{H}[\{\tau\}])/T) & \text{if } \mathcal{H}[\{\sigma\}] - \mathcal{H}[\{\tau\}] > 0 \\ 1 & \text{otherwise} \end{cases} . \tag{3.7}$$

in which $\mathcal{H}[\{\sigma\}]$ and $\mathcal{H}[\{\tau\}]$ are the Hamiltonians of the system concerning the configurations σ and τ, respectively. To use this expression for generating the possible configurations, we must first assume a Markov process, which satisfies two properties: (i) the transition rate $w(\sigma \to \tau)$ is time-independent, and (ii) the transitions depend only on the configurations τ and σ; in particular, they do not depend on what happened before configuration σ, meaning that the system has no memory of past configurations [3]. With this condition established, the probability $P(\sigma, t)$ evolves in time according to a **master equation** given by

$$\frac{dP(\{\sigma\}, t)}{dt} = \sum_{\{\tau\}} [w(\tau \to \sigma) P(\{\tau\}, t) - w(\sigma \to \tau) P(\{\sigma\}, t)] . \tag{3.8}$$

Considering the stationary probability distribution as

$$P_\infty(\{\sigma\}) := \lim_{t \to \infty} P(\{\sigma\}, t) , \tag{3.9}$$

it is possible to define the condition of **detailed balance** as

$$w(\tau \to \sigma) P_\infty(\{\tau\}, t) - w(\sigma \to \tau) P_\infty(\{\sigma\}, t) = 0 . \tag{3.10}$$

Thus, due to the time reversal invariance of the micro states, also called micro reversibility

[4] Note that there is also the Glauber Algorithm, which defines another possibility for the rates $w(\tau \to \sigma)$ in the Glauber dynamics. Reference [2] discusses details on that.

[3], Eq. (3.10) holds for equilibrium systems. In non-equilibrium systems, where the system allows the exchange of matter and energy, there is a non-vanishing flow of probability between the microstates. Therefore, the intrinsic microscopic irreversibility of the system generates a macroscopic non-equilibrium behavior, breaking detailed balance [2]. Although there is no universally valid and canonical formalism for tackling non-equilibrium phenomena, the master equation can be written in many cases. Moreover, even if the system does not obey detailed balance, a quasi-stationary state may exist, allowing the system to be described in terms of it. Details on how the quasi-stationary state is handled for the systems investigated in this thesis can be found in Appendix B.

3.2 Critical behavior in spreading phenomena

The spread of misinformation is a current and relevant issue, with negative effects in many aspects of society [94]. The dissemination of rumors is an ancient social activity, but with the advent of the internet, the speed and volume of information spread have increased enormously. In some cases, fake news behaves similarly to a virus, infecting people who then pass the misinformation on to others.

To start exploring the spreading process, we address a simple model for epidemics, as a stochastic reaction-diffusion process [95]. This model divides a population into three different classes: Susceptibles (S), as the healthy individuals; the Infected (I), currently infectious and able to transmit the disease; and the Recovered or Removed (R) ones. These classes are also called compartments. Considering a fixed population with N individuals, these can change from one compartment to another as follows. Susceptible individuals will become infected upon contact with another infected, with an infection rate λ. The transition to the recovered compartment occurs with a rate μ [96]. The diagram in Fig. 3.3 illustrates the transitions and the classes of the model.

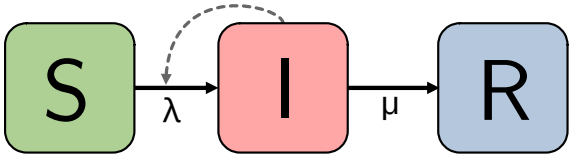

Figure 3.3 – SIR model diagram. Solid arrows represent the transitions between the classes, which happen stochastically depending on the rates λ and μ. The dashed arrow means that the transition from the S to I depends on contact with an infected individual.

To investigate the threshold in epidemic models, let us consider the fraction os susceptible, infected, and recovered individuals in a fixed population as s,i, and r, respectively. For the sake of simplicity, a well-mixed population in which individuals interact with each other randomly will first be assumed. Given constant rates for the compartment transitions, the SIR model equations are

$$\frac{ds}{dt} = -\lambda si \ , \qquad \frac{di}{dt} = \lambda si - \mu i \ , \qquad \frac{dr}{dt} = \mu i \ . \tag{3.11}$$

The $(+)$ sign means that the term stands for new individuals joining the compartment, and the opposite is for the $(-)$ sign. Given that the population size is finite, the relation $s+i+r = 1$ is valid. Thus, knowing the numerical solutions for $s(t)$ and $i(t)$, it is possible to obtain $r(t)$ [96]. Rewriting the equation for $i(t)$ in the form

$$\frac{di}{dt} = i(\lambda s - \mu) \ , \tag{3.12}$$

if the derivative di/dt is negative, the infection ends at some time. Therefore, for the epidemic to reach a finite number of individuals, necessarily, the initial fraction of susceptible individuals must exceed a threshold: $s(0) > \mu/\lambda$. This condition for an epidemic to invade was observed in the seminal paper by Kermack and McKendrick in 1927 [97].

A similar discussion on equilibrium phenomena has already been made in this text. For the paramagnetic-ferromagnetic phase transition, the system will pass from a disordered to an ordered phase only if the temperature reaches the critical value. This resemblance caught the attention of statistical physicists, who realized that epidemic models could be studied in the context of non-equilibrium phase transitions [4]. In the following, examples of different critical behaviors in spreading phenomena will be explored.

3.2.1 Contact Process

In the context of non-equilibrium systems, phase transitions can also be investigated. A particular case is when the system presents an absorbing state, which is a configuration (or a set thereof) from which the system cannot leave once reached. Systems showing this kind of state undergo absorbing state phase transitions (ASPT), and the most important universality class related to it is the Direct Percolation (DP) [2]. Many models that follow a reaction-diffusion scheme, such as the spread of an infection,

catalytic reactions, and percolation in porous media, belong to this universality class. An iconic realization of the DP class is the Contact Process model.

The Contact Process (CP) [29] is one of the simplest examples of models that exhibit a non-equilibrium phase transition. Despite its simplicity, this model presents a rich critical behavior, and many parallels can be drawn between the aforementioned equilibrium systems. Reference [4] calls the CP the 'Ising model' of absorbing state phase transitions, emphasizing these similarities. The basic implementation for CP is explained below.

Considering a lattice structure, each node can be in one of two possible states: susceptible (vacant) or infected (occupied). The initial condition can be chosen to be all nodes occupied, for instance. At a given time, an occupied node is randomly chosen, and it will infect one of its nearest neighbors with probability $p = \lambda/(1+\lambda)$ or become vacant with probability $1 - p$. The simulation runs in continuous time using the optimized Gillespie algorithm (OGA), which is detailed in Appendix C. If the infection rates λ assume values lower or greater than the critical value[5], the scenario changes, as illustrated in Fig. 3.4 for a square lattice. The critical value is presented in the literature as $\lambda_c = 1.6488(1)$ [4]. Figure 3.4 was generated using the homogeneous initial state technique, which will be explored in Sec. 3.2.4.1. The three panels are snapshots taken at the same simulation time ($t = 4.0$ since for the subcritical regime with $\lambda = 0.5$ the dynamics rapidly vanish), showing that for different infection rates, the occupation of the lattice differs even when observed at the same time.

One of the quantities that can be computed in this model is the density of infected nodes, given by $\rho = N_i/N$, where N_i is the number of occupied sites. Since the infection of a new node depends on contact with an infected neighbor, if all nodes are susceptible, the dynamics freeze in the absorbing state and no longer evolve. Thus, if we want to compute stationary quantities as $t \to \infty$, it is necessary to prevent the absorbing state from occurring. For instance, this can be done by bringing the system back to the immediately previous configuration, a method called the Reflecting Boundary Condition (RBC), through which the quasi-stationary state can be analyzed[6] [98]. Thus, the average density of infected nodes can be computed after a transient initial time t_{rlx}. In the off-

[5] It is worth emphasizing that using the expression 'critical point' in a small system such as the ones used for illustrating CP is not correct, since the phase transition occurs only in the thermodynamic limit.

[6] A more detailed discussion on quasi-stationary states is presented in Appendix B.

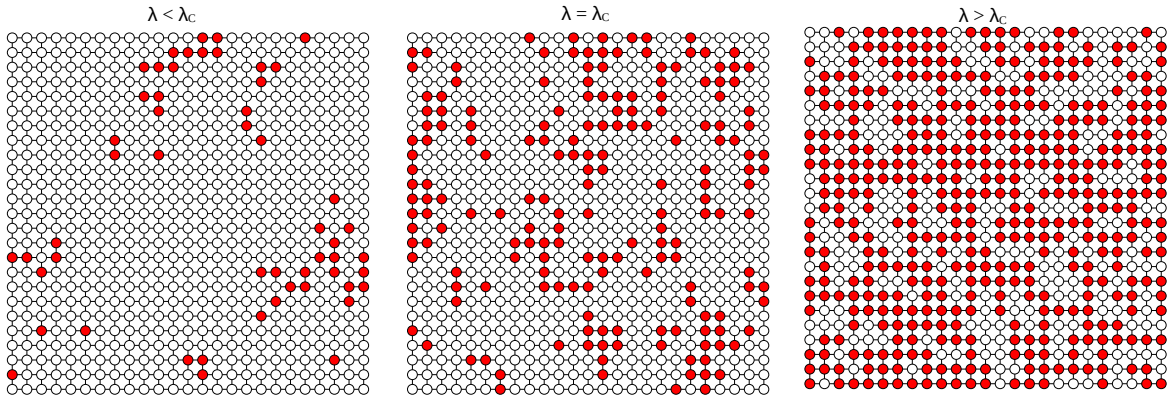

Figure 3.4 – Contact Process in a square lattice with size $N = L^2$, and $L = 25$. Red nodes are infected (occupied), and white ones are susceptible (vacant). The values of infection rate used were $\lambda = 0.5, 1.6488$, and 3.5, for the subcritical, critical, and supercritical regimes, respectively. A homogeneous initial state was employed for the three cases. The images are screenshots taken for the same simulation time $t = 4.0$.

critical regimes, the time series becomes quasi-stationary for short times, but for $\lambda \approx \lambda_c$, the time t_{rlx} required increases with the system size. This behavior is known as critical slowing down [4], and Sec. 3.2.4.1 presents an example illustrating it.

Once the absorbing state is handled, it is possible to compute the quasi-stationary average density of infected nodes, $\langle\rho\rangle$. This quantity serves as the order parameter, since, as we vary the infection rate, the system undergoes a phase transition in the thermodynamic limit. For finite systems, size effects prevent the simulations from showing the actual phase transition, which occurs only in the limit $N \to \infty$. However, the shift in the behavior of $\langle\rho\rangle$ can be observed even in small systems, such as those shown in panel (b) of Fig. 3.5, which resembles the behavior depicted in Fig. 3.1.

Another analysis that can be done is the computation of the susceptibility of the quasi-stationary time series for different infection rates. This is another term borrowed from equilibrium phase transitions, where the susceptibility represents the fluctuations of the order parameter density [4]. The susceptibility is often defined as a rescaled version of the variance $x = N(\langle\rho^2\rangle - \langle\rho\rangle^2)$. However, for a clearer visualization of numerical results a modified version of susceptibility χ [30] can be written as

$$\chi = \frac{N(\langle\rho^2\rangle - \langle\rho\rangle^2)}{\langle\rho\rangle} \ . \tag{3.13}$$

As the fluctuations on the order parameter increase significantly in the vicinity of the critical point, the susceptibility exhibits a maximum at $\lambda = \lambda_P$. This value is size dependent, and as size increases λ_P approaches λ_c. In Fig. 3.5, panel (a) shows the susceptibility as a function of the infection rate for the CP in two different lattice sizes. One can see that by only doubling the size, from $L = 25$ to $L = 50$, the curve for χ becomes sharper. Also, the transition shown in panel (b) is less rounded for the larger size. The actual critical behavior can be seen only in the infinite size limit. This finite size effect is expected, and it will be addressed in Sec. 3.2.4.1.

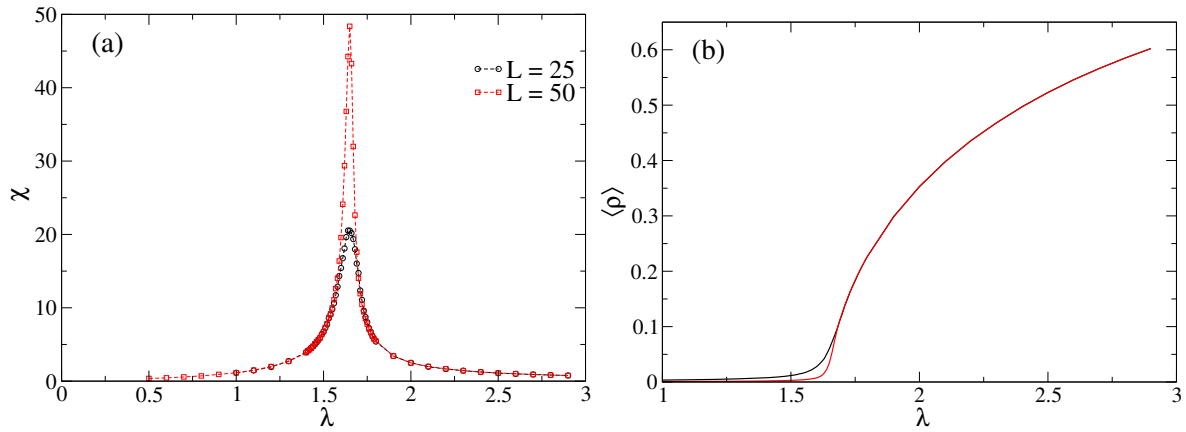

Figure 3.5 – CP model in square lattices of different sizes. Panel (a) shows the susceptibility and (b) the quasi-stationary average density of infected nodes, both as a function of the infection rate.

Consider that the nodes spread the infection to their neighbors at rate λ/q, with q being the lattice coordination number, and heal spontaneously at rate $\mu = 1$. Let $\sigma_X(t) = 1$ define the state in which the node X is occupied/infected, and $\sigma_X(t) = 0$ if it is vacant/susceptible. The time evolution of the probability, defined as $\varrho(X,t) = \text{Prob}[\sigma_X(t) = 1]$, will be

$$\frac{d\varrho(X,t)}{dt} = \underbrace{-\varrho(X,t)}_{\text{heal event}} + \underbrace{\lambda/q \sum_Y \text{Prob}[\sigma_X(t) = 0, \sigma_Y(t) = 1]}_{\text{infection event}} \ . \tag{3.14}$$

Thus, the sum is over the neighbors of site X, and the infection may occur if one of them, Y, is infected. The problem with this equation is that the two-site probability in the second term is not known. To handle this issue, a mean-field approximation can be used by assuming the occupancy of each site as statistically independent and the distribution of active sites is homogeneous in space, which means $\varrho(X,t) := \rho(t)$ [4]. Therefore, the

second term becomes $\lambda\rho(1-\rho)$, and the mean-field equation is

$$\frac{d\rho}{dt} = \rho(1-\lambda) - \lambda\rho^2 \ . \tag{3.15}$$

To study this equation, we may consider the stationary regime. Thus, it is possible to perform a stability analysis, finding two fixed points $\overline{\rho}_1 = 0$ and $\overline{\rho}_2 = 1 - \lambda^{-1}$. The first one is stable if $\lambda < 1$ and unstable otherwise, while the second has the opposite behavior, being stable if $\lambda > 1$. This marks a transcritical bifurcation at the value $\lambda = \lambda_c = 1$, interpreted as a phase transition. Also is possible to note that $\overline{\rho}_2 = \overline{\rho} \propto (\lambda - \lambda_c)$ for $\lambda \approx \lambda_c$, which represents a linear growth of the order parameter around the critical point.

Another interesting analysis is the linearization of Eq. (3.15) around the stationary solution using $\rho(t) = \overline{\rho}(t) + \delta\rho(t)$, with $\delta\rho$ being a small perturbation. After some algebra, we found that

$$\frac{d\delta\rho}{dt} = -(\lambda - 1)\delta\rho \ , \tag{3.16}$$

with solution $\delta\rho \propto \exp(-|\lambda - 1|t)$. Thus, for $\lambda \neq 1$ and $t \to \infty$

$$\rho(t) - \overline{\rho} \propto e^{-t/\tau} \ , \tag{3.17}$$

where $\tau = |1 - \lambda|^{-1}$ is the relaxation time, which diverges at the critical point, reflecting the critical slowing down aforementioned in the lattice discussion. Besides, solving Eq. (3.15) for $\lambda = 1$, we get $\rho(t) \sim t^{-\delta}$, where δ is a critical exponent, and for the mean field approach $\delta = 1$. This power-law decay will be addressed in detail in Sec. 3.2.4.1.

The mean-field approximation fails to predict the critical exponents for low-dimensional lattices, as the previously discussed one. However, the precision of the mean-field approach improves if the dimension of the system is $d > d_c$, with $d_c = 4$ being the critical dimension. This happens because, for these low dimensions, the system is strongly correlated in space, and the mean-field approximation neglects this correlation by treating each node as independent. Still, this approach can be insightful in many aspects.

3.2.2 Two-Species Contact Process

Extending the discussion on absorbing-state phase transitions, studies in recent decades have pointed out the existence of other types of transitions, different from the continuous one mentioned above. In discontinuous phase transitions, the order parameter

jumps suddenly from zero to a finite value, involving a macroscopic portion of the system. This kind of transition is also called a catastrophic phase transition [99]. For instance, discontinuous phase transitions have been observed in synchronization [15] and coevolution spreading [100]. The latter has attracted attention because the cooperative behavior between two different species, or two diseases infecting the same individual, leads to rich phase diagrams [101]. A particularly interesting example is presented in the following.

The two-species contact process (2SCP) model considers a mutualistic symbiotic relationship between two species, which could represent two diseases that benefit from coevolution within a given contact structure [102]. The model is defined as follows. Consider two diseases coevolving in a population. For simplicity, these diseases are treated as two distinct species that can replicate within the population. Each node can be either singly or doubly occupied, but hosting only one of the two species. The replication process occurs as in the standard CP: each species creates a clone of itself in a chosen neighbor at a rate λ/q, provided that this neighbor is not already occupied by the same species, where q is the number of neighbors. If the node is singly occupied, it will become vacant at rate μ. However, if the node is doubly occupied, it becomes singly occupied at a reduced rate $\mu_s < \mu$. This means that the two species benefit from doubly occupying the same node. The annihilation events are illustrated in Fig. 4.6, where panel (a) shows the singly occupied case and (b) the symbiotic relationship when the node (marked with a red border) is doubly occupied. For this work, we consider $\mu = 1$.

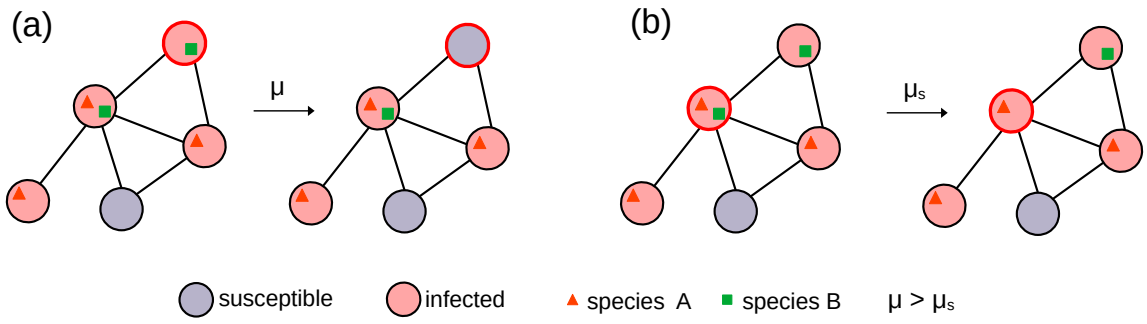

Figure 3.6 – Illustration of the annihilation events in the 2SCP. Panel (a) shows the case when the node (marked with a red border) is singly occupied, and panel (b) shows the symbiotic case, when the node is doubly occupied.

Considering a mean-field approach, the equations in terms of the probabilities of the nodes ρ_0 vacant, ρ_A occupied by one species A, ρ_B occupied by one species B, and

ρ_{AB} doubly occupied are given by

$$\frac{d\rho_0}{dt} = \rho_A + \rho_B - \lambda\rho_0\rho_T \ , \tag{3.18}$$

$$\frac{d\rho_A}{dt} = -\rho_A + \rho_{AB}\mu_s + \lambda\rho_0\phi_A - \lambda\rho_A\phi_B \ , \tag{3.19}$$

$$\frac{d\rho_B}{dt} = -\rho_B + \rho_{AB}\mu_s + \lambda\rho_0\phi_B - \lambda\rho_B\phi_A \ , \tag{3.20}$$

$$\frac{d\rho_{AB}}{dt} = -2\mu_s\rho_{AB} + \lambda(\phi_A\rho_B + \phi_B\rho_A) \ , \tag{3.21}$$

where $\rho_T = \rho_A+\rho_B+2\rho_{AB}$ is the total prevalence and the auxiliary variables $\phi_A = \rho_A+\rho_{AB}$ and $\phi_B = \rho_B + \rho_{AB}$. Considering symmetric solutions $\rho_A = \rho_B = \rho$ and the closure equation $\rho_A + \rho_B + \rho_0 + \rho_{AB} = 1$, we get only two independent variables, ρ and ρ_{AB}. So, equations (3.21) and (3.19) become, respectively

$$\frac{d\rho_{AB}}{dt} = -2\mu_s\rho_{AB} + 2\lambda\rho^2 + 2\lambda\rho\rho_{AB} \ , \tag{3.22}$$

and

$$\frac{d\rho}{dt} = -\rho + \rho_{AB}(\mu_s + \lambda - 4\lambda\rho - \lambda\rho_{AB}) - 3\lambda\rho^2 + \lambda\rho \ . \tag{3.23}$$

Taking the stationary solutions ($\dot{\rho} = 0$) of these two equations, it is possible to find the trivial solution $\overline{\rho} = \overline{\rho}_{AB} = 0$. Also, the nontrivial one for Eq. (3.22) is

$$\overline{\rho}_{AB} = \frac{\lambda\overline{\rho}^2}{\mu_s - \lambda\overline{\rho}} \ , \tag{3.24}$$

that can be used to find the nontrivial solution for ρ, obtaining

$$\overline{\rho} = \frac{\mu_s[2(1-\mu_s) - \lambda + \sqrt{\lambda^2 - 4\mu_s(1-\mu_s)}]}{2\lambda(1-\mu_s)} \ . \tag{3.25}$$

The condition for physically acceptable solutions is

$$\lambda \geq \sqrt{4\mu_s(1-\mu_s)} \ . \tag{3.26}$$

Let us work on Eq. (3.26). For the transition to occur, $\sqrt{4\mu_s(1-\mu_s)}$ may reach a maximum. So, we may compute $d(\sqrt{4\mu_s(1-\mu_s)})/d\mu_s$ to get $\mu_s \geq 1/2$ and so $\lambda_c = 1$. Also if we make a Taylor expansion of Eq. (3.25) around λ_c, and considering $\mu_s \geq 1/2$,

we get

$$\overline{\rho} \simeq \frac{\mu_s(\lambda - \lambda_c)}{2\mu_s - 1} + \mathcal{O}(\lambda - \lambda_c)^2 \ . \tag{3.27}$$

This linear growth was also observed in the context of the standard CP and indicates a continuous phase transition.

Now, let us consider the case in which $\mu_s < 1/2$. To maintain the condition of Eq. (3.26) we observe that for $\lambda_c = \sqrt{4\mu_s(1-\mu_s)}$, $\overline{\rho}$ is immediately positive. Thus, instead of a smooth variation of the order parameter, it changes abruptly to a non-zero value - this marks a discontinuous phase transition. However, it is possible to verify that for $\sqrt{4\mu_s(1-\mu_s)} < \lambda < 1$, $\overline{\rho} = 0$ is stable under small perturbations or locally stable [99]. So the steady state solution depends on the initial conditions $\rho_A(0)$ and $\rho_B(0)$. If $\rho_A(0) = \rho_B(0) \lessapprox 1$, $\lambda = \lambda^- = \sqrt{4\mu_s(1-\mu_s)}$ and if $\rho_A(0) = \rho_B(0) \gtrapprox 0$ we have $\lambda = \lambda^+ = 1$. This represents a bistable region delimited by the spinodal curves. Fig. 3.7 shows the numerical solution for the density of doubly occupied sites using the initial conditions mentioned above. The two generated curves delimit the bistable region.

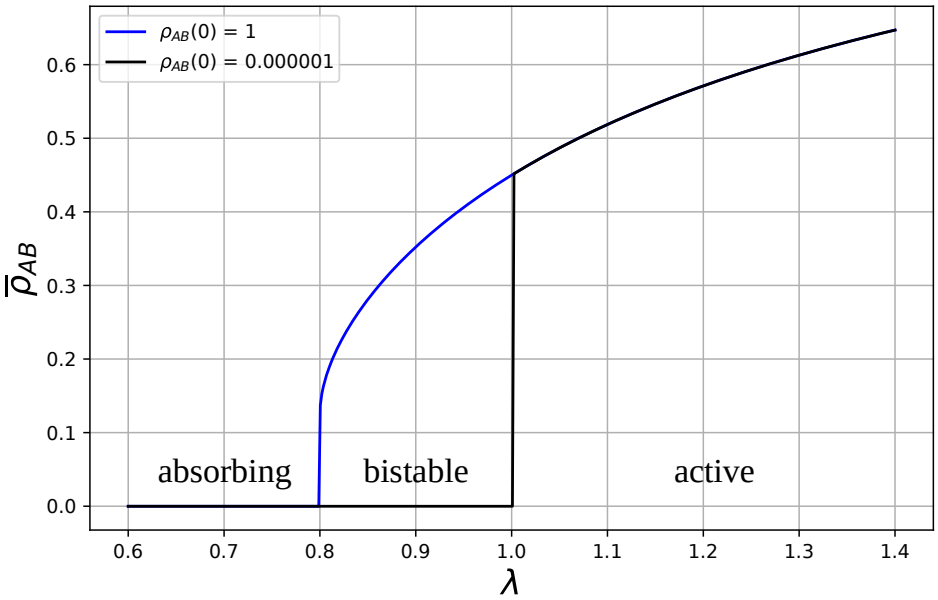

Figure 3.7 – Numerical solution of the mean-field equation for ρ_{AB} as a function of the infection rate using $\mu_s = 0.2$ for two different initial conditions.

These analyses were conducted within the context of the mean-field approach, which provides valuable insights into understanding the phenomena. However, when slightly more realistic contact distributions are considered, the equations fail to predict the correct thresholds and must be adapted. This adaptation may take the form of

the heterogeneous mean-field approach, as presented in [103] for the 2SCP. Furthermore, an even more detailed approach is possible using the homogeneous pairwise mean-field method introduced in [104]. Adaptations in the mean-field modeling will be discussed in Sec. 3.2.4.2.

3.2.3 Quenched Contact Process

Before presenting the modified version of the CP, let us first present the concept of quenched disorder. The term quenching comes from a technique in materials science and engineering, involving the rapid cooling of a material to improve its properties, such as by trapping its impurities in place. A seminal work addressing the role of quenched disorder in magnetic systems was conducted by Robert B. Griffiths in 1969 [105], in his study of the Ising model. In this paper, instead of considering a fully occupied lattice with Ising spins, he examined the case in which some spins were missing, representing nonmagnetic impurities. The occupation of spins occurs with probability p, such that the critical point may become a critical extended region depending on this parameter p.

Possible reasons for quenched disorder to happen are random impurities, defects, or irregularities in the system, which cause rare spatial regions, as illustrated in Fig. 3.8. These regions introduce singularities in the free energy in an extended parameter space region close to the phase transition, known as Griffiths Phase (GP) [106]. This effect is especially relevant in zero-temperature quantum systems [107], for instance, in which the global phase transition is smeared or rounded.

At a standard transition, a non-zero order parameter arises from a collective effect, marked by a diverging correlation length at the critical point. In contrast, in a system with relevant defects, different regions will order independently at varying temperatures. As a result, the global order will form in an inhomogeneous way, making the transition rounded. This idea can be extended to non-equilibrium systems, and smeared phase transitions were also observed in the CP model with quenched disorder [108, 109].

For a standard CP model, already discussed, if we consider an RRN with nodes having degree $m = 3$, the critical point will be around $\lambda_c = 1.63$, as shown in Fig. 3.9 (a). Also, starting from an initial condition in which all nodes are infected, the density ρ will decay exponentially in time towards the steady state for the off-critical regimes, and as a power law in the critical point, as pictured in panel (b).

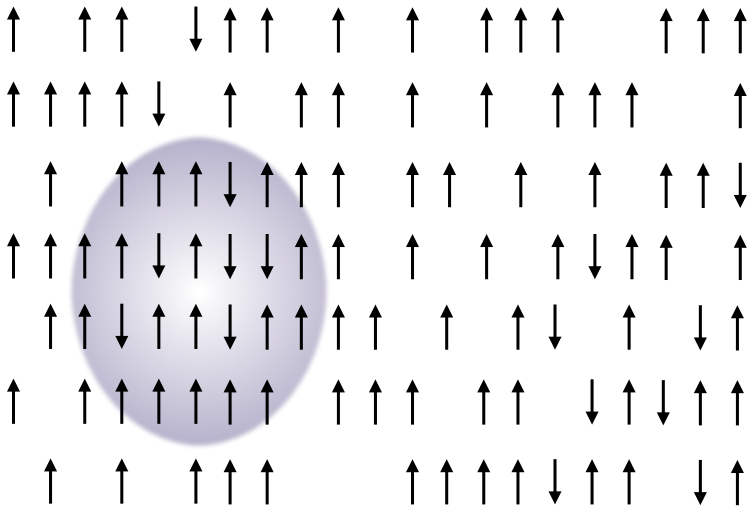

Figure 3.8 – Illustration of a rare region fully occupied by spins, while the rest of the lattice presents vacancies or defects. Inspired on Ref. [106].

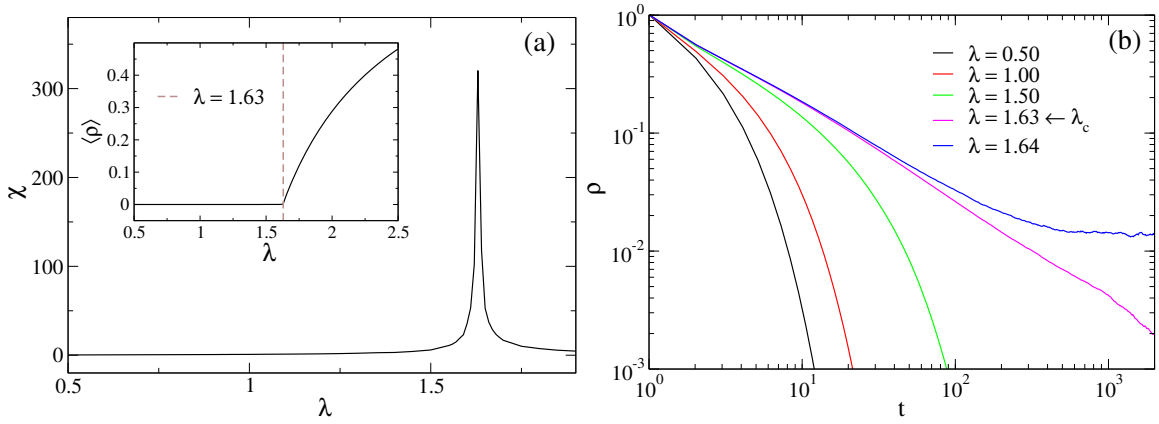

Figure 3.9 – CP model in a RRN with size $N = 10^5$ and degree $m = 3$. (a) Susceptibility and average quasi-stationary density of infected nodes as a function of infection rate. (b) Decay in time for the density of infected nodes for different values of infection rate.

However, this scenario changes significantly if disorder is introduced into the model. The Quenched Contact Process (QCP) is defined as follows [14]. Considering a network structure, a fraction q of the nodes will be randomly chosen to be type-II and have an infection rate λr, with $0 \leq r \leq 1$. The remaining ones will have an infection rate λ, these are called type-I. We considered $r = 0$ so that the q fraction of nodes will not be able to infect their neighbors. This will introduce quenched disorder in the system. As

detailed in Ref. [14], the type-I nodes will pass through a percolation transition at

$$q_{\text{perc}} = 1 - \frac{1}{\langle k \rangle} \ , \tag{3.28}$$

with $\langle k \rangle$ being the average node degree of the network structure. If $q > q_{\text{perc}}$, the activity will not be globally sustained since the type-I clusters are finite and type-II nodes can not infect others, and the system does not present an active phase. Thus, above the $q > q_{\text{perc}}$, the decay of ρ will be in power-law with varying exponents θ: $\rho(t) \sim t^{-\theta(q,\lambda)}$, forming an extended region of criticality.

For a numerical example, Fig. 3.10 shows the decay curves for a QCP in an RRN with $m = 3$, for which the percolation parameter is $q_{\text{perc}} = 2/3$. Using $q = 0.9$, it is possible to observe the range of curves following the power-law behavior and showing the existence of an extended region of critical behavior. It is important to emphasize that the network is the same as in Fig. 3.9. Thus, the introduction of quenched disorder in the system led to a Griffiths phase.

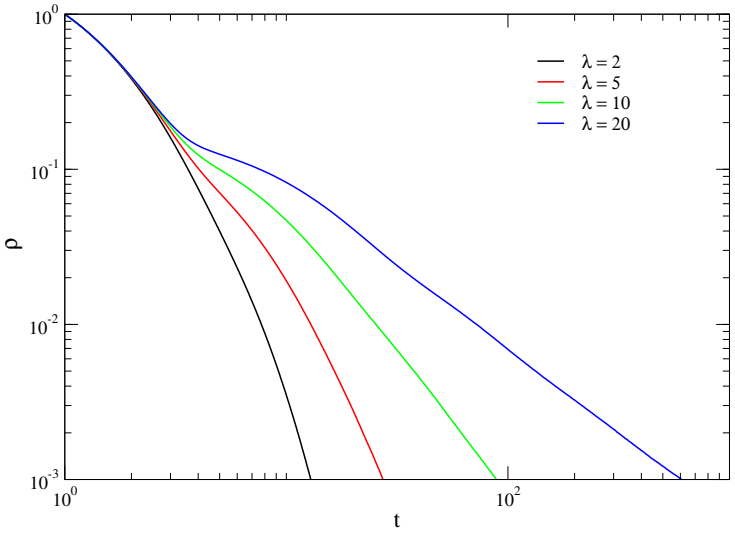

Figure 3.10 – Density of infected nodes decay curves using different infection rates for the QCP model in an RRN with size $N = 10^5$ and degree $m = 3$. The network is the same as in Fig. 3.9, but with the introduction of quenched disorder, an extended region of criticality replaces the clean critical point.

Other structures can also present GP running the QCP model, such as Erdős-Rényi networks [14], which will be addressed in Ch. IV. Also, non-hierarchical modular networks showed GP when considering topological disorder [110]. This last result supports the brain criticality hypothesis via GP [111], discussed in Ch. VI.

3.2.4 Susceptible-Infected-Susceptible model

The susceptible-infected-susceptible (SIS) model is an approach to modeling spreading phenomena. It classifies each node into a compartment based on its state. The possible states are susceptible (if the node can be infected) and infected, if the node currently transmits the disease to its susceptible nearest neighbors. The transitions between these states occur through events illustrated in Fig. 3.11. A node becomes infected upon contact with infected neighbors with rate λ per contact, in which λ is called the infection rate. The healing event is spontaneous and happens at a rate μ.

Considering continuous-time Markovian formulation, a Poisson process can be assumed, where the probability of a node remaining in the infected compartment for a time t is $P_{\text{inf}}(t) = \mu e^{-\mu t}$, leading to an average infectious period of $\langle t \rangle = \mu^{-1}$ [5]. Details on the algorithm OGA employed for SIS simulations are in the Appendix C.

In Fig. 3.11, the quantity ρ represents the density of infected nodes, given by $\rho = N_i/N$, where N_i is the number of infected nodes. ρ is also called the epidemic prevalence. Note that the configuration $\rho = 0$ is an absorbing state, since once the system reaches this state, the dynamics are frozen due to the absence of spontaneous infections. Thus, it is necessary to perturb the system for the dynamics to continue active [112]. These perturbations can be, for instance, the reactivation of the last infected node or the reactivation of the most connected node, allowing the system dynamics to proceed. Different strategies for perturbing the system to drive it into a quasi-stationary state are discussed in Appendix B.

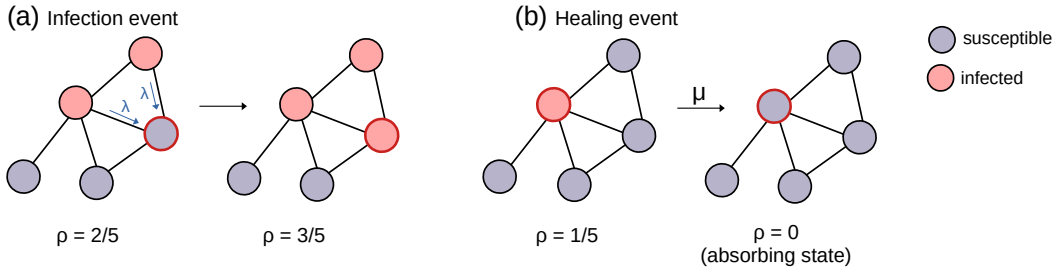

Figure 3.11 – Illustration of the infection (a) and healing (b) event in the SIS model on a network structure. The absorbing state occurs if all the nodes are susceptible and the dynamics of the system become trapped.

3.2.4.1 Critical exponents for SIS in lattices

Despite its simplicity, this model is known to exhibit important critical features [80]. For instance, ρ is an order parameter, as varying the infection rate causes the system to transition from an inactive (absorbing) phase to an active (endemic) one at $\lambda = \lambda_c$, where λ_c is the epidemic threshold. One possible approach to study this phase transition is through the critical exponents (see Sec. 3.1).

Starting from different initial conditions, two simulation strategies can be performed. The first one is the homogeneous initial state simulation, which is useful for determining the critical point and some critical exponents. The second one, the seed simulation, contributes to computing other critical exponents. Both methods will be discussed in sequence. We tested it in regular networks using the SIS model, which is equivalent to the Contact Process model by rescaling the infection rate as λ/k when the network is homogeneous, which means the degree of all nodes in the network k is constant. The universality class for it is still DP, whose critical exponents are well known in the literature.

Homogeneous Initial State Simulation

The initial condition in this case is a fully occupied lattice, or in terms of spreading phenomena, all nodes are infected. The density of infected individuals ρ as a function of time must be computed and averaged through many runs. To understand how the size of the system influences the analysis of the critical exponents, let us consider the following. Besides the correlation length ξ, the relaxation time t_{rlx}, which will be explained ahead, also diverges as $\lambda \to \lambda_c$. These two divergencies are characterized by two different critical exponents, $\nu_\perp$ and $\nu_{||}$, defined as [4]

$$\xi \propto |\lambda - \lambda_c|^{-\nu_\perp} \quad \text{and} \quad t_{\text{rlx}} \propto |\lambda - \lambda_c|^{-\nu_{||}} \ . \tag{3.29}$$

Finite-size effects can influence the analysis if the lateral system size L is of the same order of magnitude as or smaller than ξ. These effects become less evident if we use $L \gg \xi$, since the active state will be practically stable, allowing the order parameter to fluctuate around a stationary value [2]. Additionally, the correlation length is known to scale at the critical point as

$$\xi(t) \sim t^{1/z} \ , \tag{3.30}$$

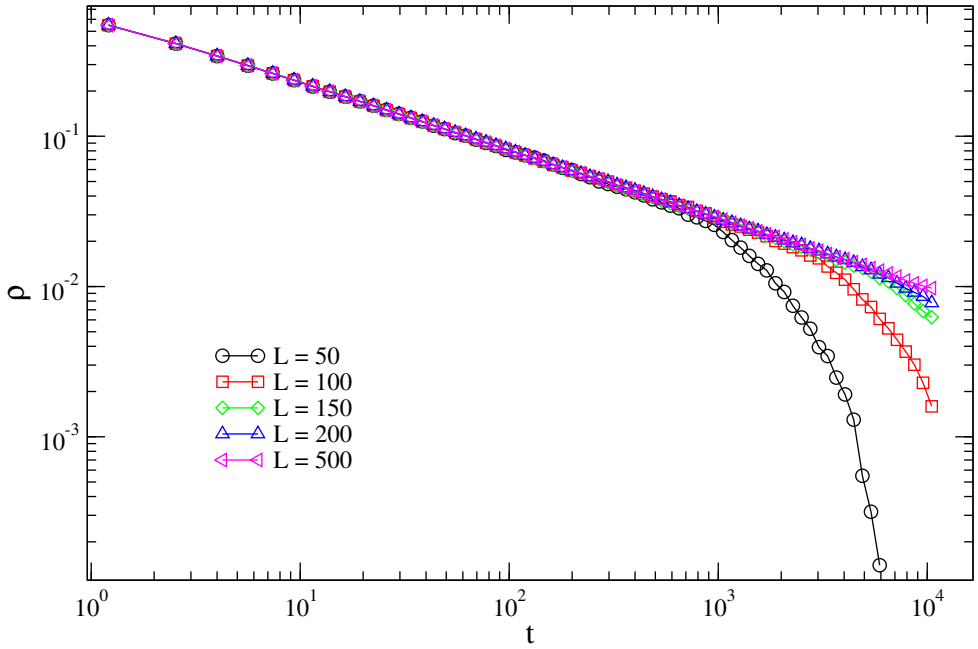

Figure 3.12 – Homogeneous initial state simulation - density of infected individuals as a function of time for different lattice sizes. The curves were generated using the critical control parameter $\lambda_c = 0.412175$ and averaged over 1000 runs.

in which $z = \nu_{||}/\nu_{\perp}$ is the dynamical exponent and assumes the value $z = 1.7660(16)$ for DP universality class in two dimensions. At criticality, the density of infected individuals decays following the power law

$$\rho(t) \sim t^{-\alpha}, \tag{3.31}$$

with $\alpha = \beta/\nu_{||}$ being a critical exponent that assumes the value $\alpha = 0.4505(10)$ with $\beta = 0.5834(30)$ for the DP universality class [2]. In finite systems, due to the non-vanishing probability of reaching an absorbing state, equations (3.30) and (3.31) break down when the ξ is comparable to the lateral size L. The finite-size effects will become less appreciable after a typical relaxation time t_{rlx} that scales with the system size as $t_{\text{rlx}} \sim L^z$. These finite-size effects can be observed in Fig. 3.12, as L increases, the curves approach the power law decay in Eq. (3.31).

In this case, the critical value for the control parameter is already known: $\lambda_c^{CP} = 1.6488(1)$ [4], so for the SIS model, $\lambda_c^{SIS} = 0.412175$. An efficient approach to determine the epidemic threshold is to plot the decay curves as a function of time for different values of infection rate and large sizes, where finite size effects are negligible for the investigated time scale. This method is illustrated in Fig. 3.13, with the inset zooming in on the curves for $\lambda \approx \lambda_c$. For the curve corresponding to the critical value, the decay follows Eq. (3.31) asymptotically.

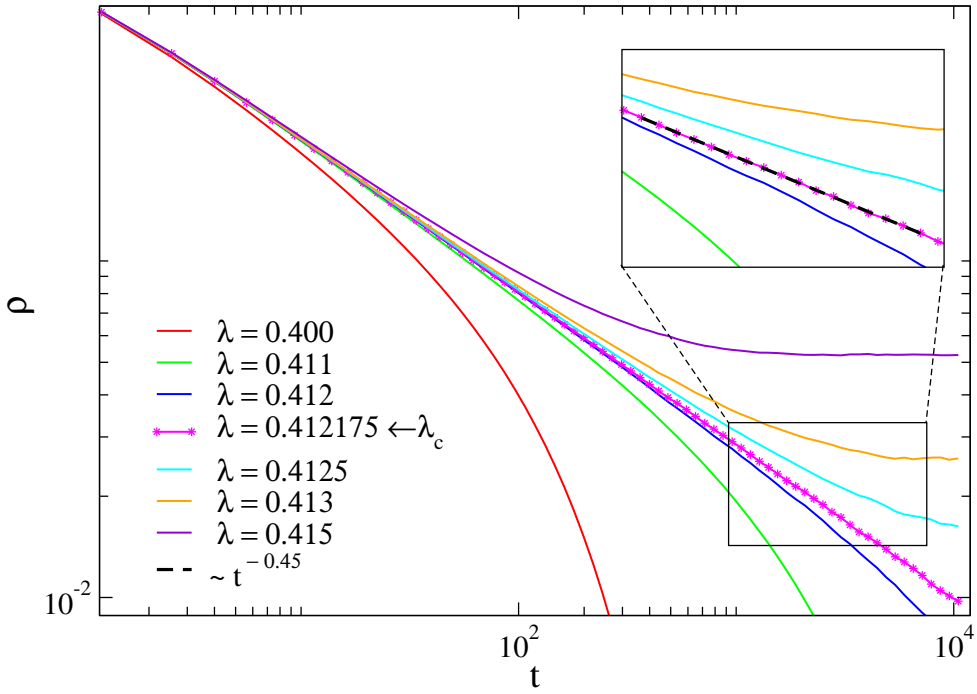

Figure 3.13 – Homogeneous initial state simulation - density of infected individuals. The inset is a zoom near the critical curve, in magenta color with the star symbols. The lattice has size $L = 500$, the total time is $T = 10^4$, and the number of samples varies from 10000 for subcritical curves to 500 for the supercritical ones.

Seed Simulation

In this type of simulation, the lattice begins with a single infected individual, while all other sites are susceptible. The cluster of infected sites then expands from this initial condition, which serves as a seed. Three time-dependent quantities can be measured and averaged over surviving runs.

The survival probability, $P_{sur}(t)$, is computed by counting the fraction of samples that remain active at time t over all samples. The number of active sites is denoted by $N_a(t)$ and is used to calculate $R_s^2(t)$, which represents the mean square displacement from the original seed, that is, the average distance between all infected sites and the seed. At the critical point, these three quantities follow the power laws

$$P_{sur}(t) \sim t^{-\delta} \ , \qquad N_a(t) \sim t^{\Theta} \ , \qquad R_s^2(t) \sim t^{2/z}. \tag{3.32}$$

in which δ, Θ, and z are critical exponents. For the DP universality class, these values are $\delta = 0.4505(10)$, $\Theta = 0.2295(10)$, and $z = 1.7660(16)$ for $d = 2$.

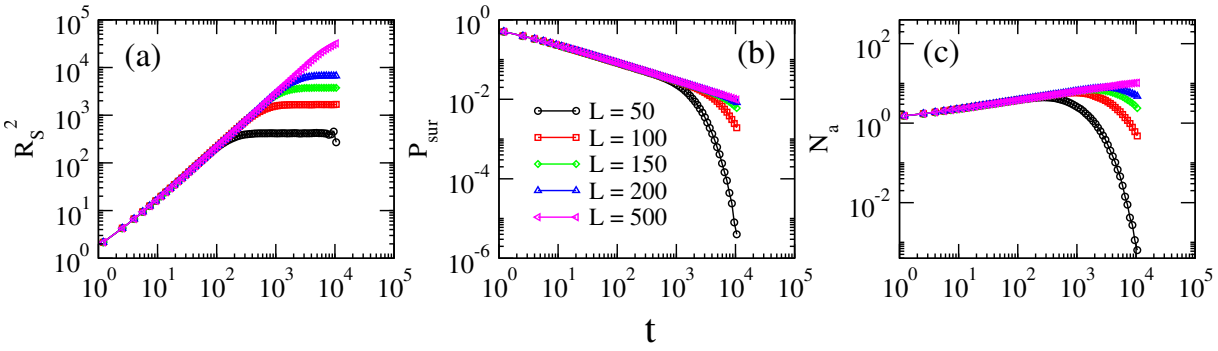

Figure 3.14 – Seed simulations for the SIS model on square lattices of different sizes. Averages over 5.10^5 samples were used. The infection rate is the critical value $\lambda_c = 0.412175$.

Considering again the SIS model on a square lattice, the three above-mentioned quantities were computed for different lattice sizes using the curves at the critical point. This is shown in Fig. 3.14, where it is possible to observe that as the size of the system increases, the finite-size effects become less evident. For the size $L = 500$, even with $R_s^2(t)$ showing finite size effects, the power-law behaviors in $P_{sur}(t)$ and $N_a(t)$ are not highly influenced by size for the simulation time used, approaching the decay of Eq. (3.32).

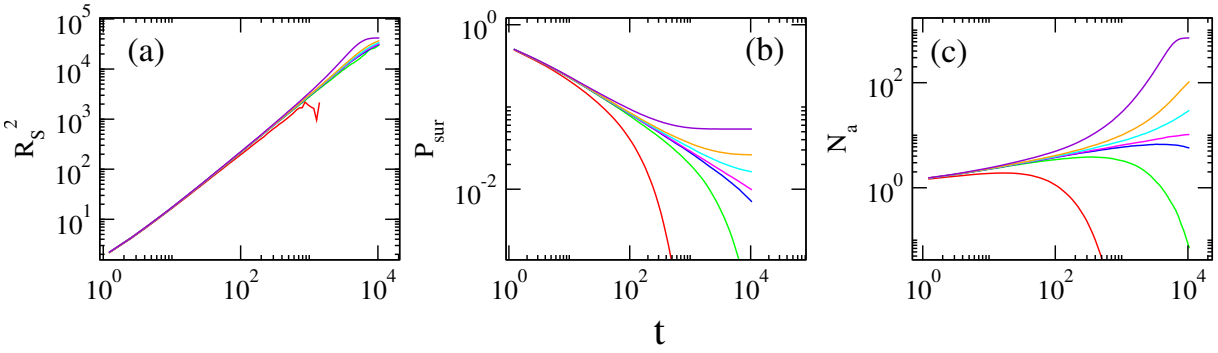

Figure 3.15 – Seed simulations for the SIS model in a $L = 500$ lattice. Colors are the same used in Fig. 3.13 and correspond to the same infection rate values.

Another analysis involves determining the critical point by plotting different values of λ for a system size large enough that finite-size effects become negligible, as shown in Fig. 3.15. The number of active sites, presented in Fig. 3.15(c), is the most sensitive quantity for detecting deviations from criticality. This can be observed by analyzing the magenta curve, which appears to correspond to the critical value. In a qualitative analysis, one can infer that this curve is the one that most closely follows the expected power-law behavior, while the subcritical curves deviate downward and the supercritical

ones deviate upward. For a more precise determination of the curve corresponding to the critical point of the transition, a quantitative analysis is necessary, such as computing the local slope. Additionally, a larger system than the ones used would provide more accurate results.

3.2.4.2 Network Epidemiology

Among the many dynamic processes that can be investigated using networks, spreading phenomena are particularly relevant. For instance, the spread of airborne infections depends on contact patterns. Moreover, the number of contacts within a population can be highly heterogeneous. These two features can be captured by analyzing social contacts as network structures within a simple framework [96]. Furthermore, network structure plays an important role in determining how spreading phenomena behave. Scale-free networks have been shown to lead to a zero epidemic threshold in basic epidemic models, meaning that infections can propagate in these networks regardless of the infection rate [113]. Therefore, networks are a key ingredient in modeling the spread of infectious diseases [5]. Since epidemiology deals with the incidence, distribution, and control of diseases, the term *network epidemiology* is appropriate to describe its connection to network theory.

Understanding how network structure affects SIS dynamics is an important topic of investigation, and it will be addressed from two perspectives in the following text. First, this analysis will be approached through different mean-field formulations. Then, the activation mechanisms responsible for driving the transition in the SIS model will be discussed.

Homogeneous mean-field

The homogeneous mean-field approximation, already mentioned in this chapter, is widely used in non-equilibrium phase transitions [2]. The simplest approach is homogeneous mixing. This means that individuals in the network are considered to be identical and well-mixed. They all interact with each other completely at random so that each individual in a given compartment is treated indistinguishably from the others in the same compartment [5]. Assuming this, the dynamical equation for ρ is

$$\frac{d\rho}{dt} = \underbrace{-\mu\rho}_{healing} + \underbrace{\lambda k\rho(1-\rho)}_{infection}, \tag{3.33}$$

in which we can use $\mu = 1$ without loss of generality. Considering $t \to \infty$, two stationary solutions can be found: $\overline{\rho}_1 = 0$ and $\overline{\rho}_2 = 1 - 1/(\lambda k)$. Performing stability analysis, we get that $\overline{\rho}_1$ is stable for $\lambda < 1/k$ and $\overline{\rho}_2$ is stable for $\lambda > 1/k$, meaning that the epidemic threshold for the homogeneous mean-field approximation is $\lambda_c = 1/k$. Thus, the system asymptotically reaches an absorbing phase for $\lambda < \lambda_c$, and an active phase appears and $\rho \to \overline{\rho}_2$ otherwise. Note that this formulation does not take the network structure into account.

Heterogeneous mean-field

The previous approximation can be improved by considering the heterogeneity in the degrees of the nodes in the network, following a heterogeneous mean-field (HMF) approach [114]. In the HMF framework, all nodes of degree k are considered statistically equivalent, implying that we compute the fraction of nodes of degree k that are infected ρ_k. Additionally, this approximation assumes that nodes of degree k are connected to nodes of degree k' with probability $P(k'|k)$ [5]. Thus, Eq. (3.33) is modified, leading to the following corresponding dynamical equation

$$\frac{d\rho_k}{dt} = -\rho_k + \lambda k(1-\rho_k)\sum_{k'} P(k'|k)\rho_{k'}, \tag{3.34}$$

so that the total density of infected individuals can be computed using $\rho = \sum_k \rho_k P(k)$. Thus, the procedure is to perform a linear stability analysis of the absorbing state by expanding Eq. (3.34) to the leading order, giving

$$\frac{d\rho_k}{dt} = \sum_{k'} J_{kk'}\rho_{k'}, \quad \text{with} \quad J_{kk'} = -\delta_{kk'} + \lambda k P(k'|k), \tag{3.35}$$

where $J_{kk'}$ is the Jacobian matrix. We know that $\overline{\rho_k} = 0$ is a stationary solution of Eq. (3.34), and it is unstable if at least one eigenvalue of the Jacobian matrix is positive [5]. We can rewrite the Jacobian matrix as $J_{kk'} = -\delta_{kk'} + \lambda C_{kk'}$, where $C_{kk'} = kP(k'|k)$ is the connectivity matrix. For uncorrelated networks, this matrix takes the form $C_{kk'} = kk'P(k')/\langle k\rangle$ [115]. Thus, an eigenvector equation can be written as $\sum_{k'} C_{kk'}v_{k'} = \Lambda v_{k'}$, so that one of the possible eigenvectors of $C_{kk'}$ is $v_k = k$ with eigenvalue $\Lambda = \langle k^2\rangle / \langle k\rangle$.

Let us consider positive-definite matrices (all entries are positive or zero) that are also irreducible, meaning that they can not be decomposed into smaller sub-matrices. Reducible adjacency matrices occur, for example, for networks presenting more than one connected component, which is not the case under consideration. For these non-negative irreducible matrices, the Perron-Frobenius theorem states that their largest eigenvalue is unique. Also, there is one eigenvector associated with this eigenvalue that has all elements non-negative, and it is the only such eigenvector [9]. Therefore, $\Lambda = \langle k^2 \rangle / \langle k \rangle$ is the largest eigenvalue of $C_{kk'}$, and so $-1 + \Lambda\lambda$ is the largest eigenvalue of $J_{kk'}$. Thus, the absorbing state will be an unstable solution when $-1 + \Lambda\lambda > 0$, and the epidemic will enter an active phase if $\lambda > \lambda_c = \langle k \rangle / \langle k^2 \rangle$, which is the epidemic threshold under the HMF approximation. It is interesting to note that for a homogeneous case, i.e., a regular network, we have $\langle k^2 \rangle = \langle k \rangle^2 = k^2$, leading to an epidemic threshold of $\lambda_c = 1/k$, and recovering the result obtained in the homogeneous mean-field case.

As discussed in Ch. II, for scale-free networks with $2 < \gamma < 3$, the second moment of the degree distribution diverges as the size of the network increases, leading to a vanishing HMF epidemic threshold in the thermodynamic limit. For $\gamma > 3$, $\langle k^2 \rangle$ is finite, and so is the λ_c predicted by HMF. However, this result contradicts both rigorous [116] and numerical [30] findings, which predict a vanishing epidemic threshold for power-law degree-distributed networks in this regime as well. This suggests that an alternative approximation should be considered to capture this behavior.

Quenched mean-field

Another mean-field approximation can be considered by stating that all nodes are statistically independent and the network is fixed. This approximation is known as the microscopic mean-field approach or the individual-based mean-field. Another term for this is the 'quenched mean-field' (QMF), which is the one used in this text. This approach takes into account the detailed topological structure of the network [117]. Thus, the dynamical equation is given by

$$\frac{d\rho_i}{dt} = -\rho_i + \lambda(1 - \rho_i) \sum_j A_{ij}\rho_j \ , \tag{3.36}$$

in which A_{ij} is the adjacency matrix defined in Ch. II, accounting for connections between node i and its neighbors j. Thus, the second term, concerning the infection event,

computes the probability that node i is susceptible, multiplied by the probability that any of its neighbors is infected, times the infection rate [5].

The procedure to obtain the epidemic threshold is similar to the one employed in HMF, but now the Jacobian matrix assumes the form $J_{ij} = -\delta_{ij} + \lambda A_{ij}$. Using the stability analysis of the stationary solution of Eq. (3.36), it is possible to verify that the epidemic threshold is given by $\lambda_c = 1/\Lambda_{\max}$, where $\Lambda_{\max}$ is the largest eigenvalue of A_{ij}. Chung *et al.* in [118] computed the largest eigenvalue of the adjacency matrix for power-law uncorrelated graphs, leading to the following epidemic thresholds [33]

$$\lambda_c \simeq \begin{cases} 1/\sqrt{k_{\max}} & , \quad \gamma > 5/2 \\ \langle k \rangle \,/\, \langle k^2 \rangle & , \quad 2 < \gamma < 5/2 \end{cases} , \tag{3.37}$$

that predicts a vanishing λ_c for power-law degree-distributed networks with different exponents. This happens because, as discussed in Ch. II, for these networks following $P(k) \sim k^{-\gamma}$ with $2 < \gamma < 3$, the second moment of the distribution diverges as $N \to \infty$.

The approximated expressions for the epidemic threshold given in Eq. (3.37) show good agreement with extensive simulations [30]. However, it is important to note that in both the HMF and QMF approaches, the probability that a node is infected is calculated, neglecting dynamical correlations between nodes. Therefore, a more accurate comparison between analytical and numerical results can be achieved by considering an extension of this approach, called the Pair Quenched Mean-Field (PQMF), in which the dynamics between pairs of nodes are considered rather than only individual nodes [119].

In summary, one of the central interests in studying network epidemiology is to compute estimates for the epidemic threshold, above which the system undergoes a transition from an inactive phase to an active one. Additionally, analyzing how this threshold behaves as the system approaches the thermodynamic limit allows us to study the phase transition. Yet, how does this phase transition occur? What are the mechanisms responsible for driving the system into an active state, with an extensive number of nodes becoming infected?

Activation Mechanisms

To answer the question raised in the last subsection, let us begin by considering the ASPT. For the SIS model, the density of infected nodes is the order parameter. In regular

lattices, the system relaxes toward a fluctuating steady state, and an infinite cluster of active (infected) nodes emerges for a finite value of $\lambda \geq \lambda_c$ in the thermodynamic limit [2]. Thus, for these homogeneous structures, the epidemic exhibits a collective activation, involving the whole lattice. However, in heterogeneous networks, hubs play a fundamental role in the spreading dynamics of networks [113], leading in some cases to a vanishing epidemic threshold, as discussed in the previous subsection.

The role played by hubs in the activation of epidemics was tackled by Boguña *et al.* in [120]. This issue was also addressed in detail by Ferreira *et al.* in [121], where the authors show that the influence of hubs on the spreading dynamics depends on two key quantities: the hub lifetime and the hub mutual infection time. The hub lifetime, τ_k^{rec}, is defined as the average time required for a hub of degree k to reach a configuration in which both the hub and all of its leaves are susceptible, assuming the initial condition as the hub infected and the leaves susceptible. This quantity is also known as activity lifespan. Modeling the hub as a star graph, the authors show that $\tau_k^{\text{rec}} \sim \exp(ak\lambda^2)$ for the SIS model, where a is a constant. The hub mutual infection time $\tau_{kk'}^{\text{inf}}$ is the time scale with which an infected hub of degree k (source) infects a susceptible hub of degree k' (target) distant from each other, as illustrated in Fig. 3.16. The approximated expression for that is $\tau_{kk'}^{\text{inf}} \sim 1/\lambda$. If $\tau_k^{\text{rec}} \gg \tau_{kk'}^{\text{inf}}$, then infections within the hubs persist much longer than the time required for hubs to infect each other, and the epidemic transition is governed by the dynamics of hub activation.

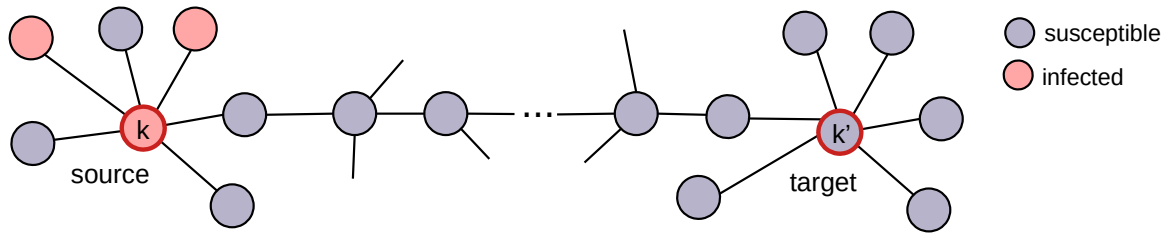

Figure 3.16 – Illustration of two hubs connected by nodes of arbitrary degree. The infection starts in the source node of degree k and gets to the target, which is a susceptible hub of degree k'. Inspired in [121].

Although hubs often have a strong impact on epidemic spreading, their influence can depend on whether they are located in the periphery of the network or embedded within its central core. Kitsak *et al.* showed that, in certain cases, the most effective

spreaders are not necessarily the nodes with the highest degree. Instead, nodes situated in the core of the network, identified through a k-core (or k-shell) decomposition, may play a more central role in driving the spread [122]. A similar analysis is made for SIS dynamics in [123], in which the authors explore the competing activation mechanisms that can be present in uncorrelated networks.

The procedure of k-core decomposition is illustrated in Fig. 3.17, where nodes are assigned integer labels k_S based on their remaining degree during an iterative pruning process. This process has the following steps: (i) starting from the original graph, one removes all the nodes with degree $k = 1$, and this action is repeated until there are only nodes with degree $k \geq 2$. The removed nodes constitute the $k = 1$-core; (ii) the next step is to successively remove all nodes having degree $k = 2$, until no one is left, and the removed nodes will belong to the $k = 2$-core; (iii) the process is repeated until, in a given interaction, all nodes in the network are removed; at this moment, the maximum k-core has been identified. In Fig. 3.17, the maximum k-core has degree $k_s = 3$.

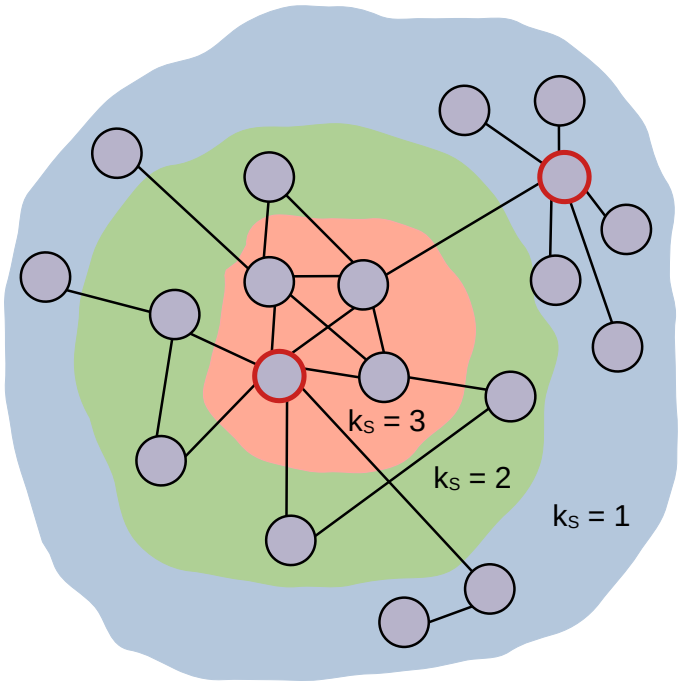

Figure 3.17 – Illustration of k-core decomposition in a network. The red-framed nodes are the hubs. They are localized in different shells, and consequently, they have contrasting influences on the spreading. Inspired in [122].

The maximum k-core has been shown to be crucial to spreading dynamics. Castellano and Pastor-Satorras [123] showed that considering a value of the infection rate corresponding to a globally active network, if the hubs are isolated from the rest of the network, they would be inactive for this λ, while the maximum k-core analyzed apart would be active. This indicates that the transition to the active phase is triggered by this densely connected core of the network. The identification of the most influential spreader structures in the network has a theoretical purpose in understanding how the network becomes activated and undergoes a phase transition. Nevertheless, a more practical motivation is related to immunization strategies to target the super-spreaders, which are not always the hubs.

3.3 Concluding remarks

Starting from basic notions of equilibrium phase transitions, this chapter has progressed to non-equilibrium systems characterized by absorbing state phase transitions. The rich critical behavior of spreading processes has been discussed, from critical exponents to the activation mechanisms that drive the transition in the quasi-stationary prevalence. The methods and concepts presented here will provide the groundwork for the following chapters.

IV Visibility Graphs for spreading phenomena

Related publications:

J. T. Moraes and S. C. Ferreira, *Visibility graphs of critical and off-critical time series for absorbing state phase transitions*, Phys. Rev. E 108, 044309, 2023 [31].

J. T. Moraes and S.C. Ferreira, *Strong localization blurs criticality of time series for spreading phenomena on networks*, Phys. Rev. E 111, 044302, 2025 [32].

A vast diversity of complex systems can be described through sequences of time-ordered values of a given observable. Sampling adjacent points in time naturally introduces correlations that can be investigated using mathematical and statistical models, a process commonly referred to as time series analysis [16]. Time series problems arise in a wide range of fields. In natural phenomena, the time series approach can be used to forecast average daily temperatures, which strongly influence the weather derivatives market [124]. Additionally, characterizing variations in time series of wind speed can be relevant to the study of wind energy generation [17].

In social systems, such as financial markets, the complexity of internal elements and external factors acting on them constitutes a dynamical process that is difficult to understand [125]. Still, the statistical properties of certain observables seem to be universal, as they appear similar across different markets. Thus, observables such as transaction prices or values of market indices constitute time series that can be used to analyze volatility, which measures how likely a quantity is to fluctuate [126]. Also in this context, time series of bilateral trade between countries can be shown to be affected by the adoption of a currency union [18].

Time series are used extensively in biological systems. In particular, the analysis of electroencephalogram (EEG) measurements can be relevant for detecting the dynamical manifestations of epilepsy in the brain [19]. EEG signals can also help understand the effects of anesthesia, sleep apnea, and Alzheimer's disease, to name a few applications [20]. Also, as will be mentioned in Ch. VI, blood oxygenation level-dependent (BOLD) time series can be used to map activity in the brain and support the critical brain hypothesis [47].

An epidemic spreading in a population is a complex system combining social and biological aspects. In epidemiology, the measure of the fraction of a population currently infected is called prevalence. These time series can be helpful for strategies in epidemic surveillance, estimating the size of the infected group, and aiding in epidemiological forecasting [127].

These examples illustrate the broad applicability of time-ordered data in understanding complex systems. However, reverse engineering to identify the underlying process that generates the behavior observed in a time series remains a challenge [21]. One method in this direction is phase-space reconstruction using a single coordinate, originally proposed in the context of turbulent fluids [128]. This technique was improved by the delayed-coordinate embedding method, which enables the identification of strange attractors present in time series [129]. The reconstructed attractor is expected to preserve the properties of the original attractor in the system. Once the attractor is reconstructed, various measures can be used to characterize it, such as the fractal dimension, the largest Lyapunov exponent, and measures of entropy. These measurements can be applied to understand the brain using EEG signals, for instance [20]. However, it is important to note that phase-space reconstruction involves determining parameters that are not known a priori and requires careful analysis.

Another possibility in time series analysis is mapping the time-ordered data onto a graph and analyzing this structure instead. As extensively discussed in Ch. II, complex networks offer a vast toolbox of measurements and analytical methods. Thus, a complex network approach to time series analysis presents a promising alternative for solving problems that have not been successfully addressed by other methods [22]. There are different ways of transforming time series into networks. For instance, using the idea of recurrence in phase space, proximity and transition networks can be constructed [130]. Although helpful in some cases, these two approaches may lead to a significant loss of information from the original systems and depend on many parameters for their construction.

A different approach is based on the convexity of successive observations in univariate time series data, mapping them onto visibility graphs (VG). The VG approach has attracted great interest due to its simple application: the network is constructed based on a geometric criterion and requires no parameters. The generated VG preserves many characteristics of the original time series and can provide relevant insights into the underlying system, such as identifying regime shifts and dynamical transitions [22].

The present chapter elaborates on the use of VG for analyzing synthetic prevalence time series generated from spreading models discussed in previous chapters. This text aims to show how the VG method provides information on the criticality of the time series [31], as well as localization in the original structures where the spreading process takes place [32].

4.1 Construction and applications of a visibility graph (VG)

Mapping time-ordered data onto graph structures enables the use of graph-theoretical measures to characterize the time series. The method proposed by Lacasa et al. in [23] consists of treating the data points in a time series $y(t)$ as nodes. Two of these nodes are connected in the resulting graph if their corresponding values on the time series y_a and y_b have visibility, that is, if a straight line can be drawn between them without intersecting any intermediate point y_c. In mathematical terms, the visibility criterion is given by

$$y_c < y_b + (y_a - y_b)\frac{(t_b - t_c)}{(t_b - t_a)} = A. \tag{4.1}$$

This expression comes from the geometric condition that three points (t_a, y_a),(t_b, y_b), and (t_c, y_c) in a plane are collinear if

$$\begin{vmatrix} t_a & y_a & 1 \\ t_b & y_b & 1 \\ t_c & y_c & 1 \end{vmatrix} = 0 \ , \quad \text{with} \quad t_a < t_c < t_b. \tag{4.2}$$

Thus, the three points will lie on a straight line in the plane if $y_c = A$, with A given by Eq. (4.1). Therefore, for the points $y_a(t_a)$ and $y_b(t_b)$ to have visibility, we must have $y_c(t_c) < A$ for $t_a < t_c < t_b$. A schematic illustration of the visibility criterion is shown in Fig. 4.1, along with a VG generated from a time series of 20 randomly generated points. In this figure, one can observe the correspondence between the data points in the series and the nodes in the VG. Points with high visibility in the time series become hubs in the corresponding VG. Note that not all the largest values necessarily have high visibility, as for example, point 20 in the time series. So, visibility also depends on the neighborhood of the given point.

Concerning computational implementation, if we directly apply Eq. (4.1), the

computational complexity of the algorithm is $O(t^2)$ for a time series of t points, since all-to-all connections must be checked. However, some optimizations can be performed to reduce this complexity and allow the simulations to run in a feasible amount of time. Details of the computational implementation of the VG algorithm are discussed in Appendix D.

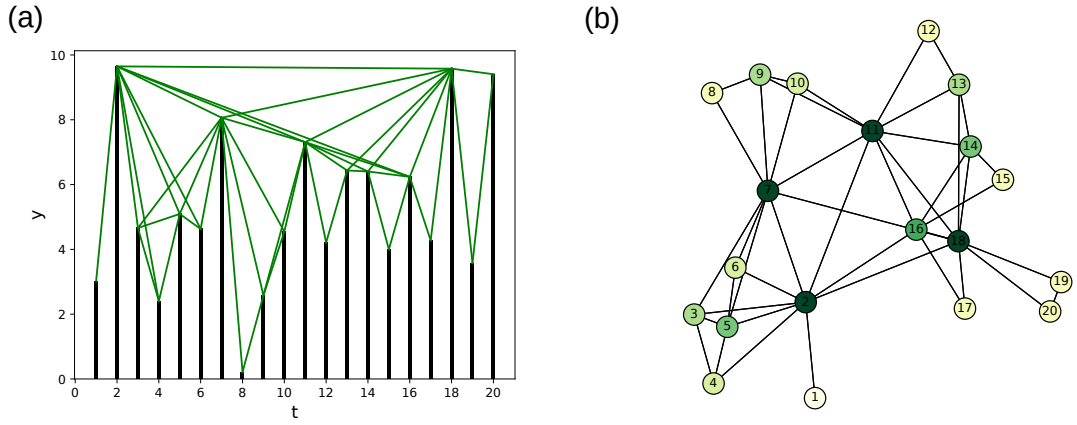

Figure 4.1 – Visibility graph (b) built using the time series in (a), which consists of 20 randomly generated numbers between 0 and 10. Lines in (a) illustrate the visibility criterion of Eq. (4.1). Node colors change from light to dark green as the degree increases.

The graph structure generated using this method will always be undirected and connected (since each node sees at least its nearest neighbors), and it will also be invariant under affine transformations of the time series, such as rescaling of the vertical or horizontal axes [23]. Additionally, the generated VG will inherit characteristics of the original time series. For instance, periodic signals generate regular VG structures, whereas random time series, such as white noise[1], lead to VGs with an exponential degree distribution [22], as will be discussed in the following.

Furthermore, fractal time series, such as those generated from Brownian motion, have been shown to map into scale-free VGs [23]. To explore this feature further, let us generalize the analysis by considering Fractional Brownian motion (fBM). In fBM, time series follow $x(bt) = b^H x(t)$, where H is the Hurst exponent. If $H > 0.5$ ($H < 0.5$), the time series will show persistence (antipersistence) [131]. The one-step memory Brownian motion is recovered when $H = 0.5$. Lacasa *et al.* [24] conjectured that H is related to the

[1] Time series generated from uncorrelated random variables, in which all periodic oscillations (all frequencies) are present with equal strength [16].

exponent of the degree distribution γ (with $P(k) \sim k^{-\gamma}$) of the generated VG as

$$\gamma = 3 - 2H \ , \qquad 0 < H < 1. \tag{4.3}$$

In Fig. 4.2, we analyze fBM series generated using the Davies-Harte method [132], with a fBM Python library available in [133]. We compute time series for three different values of the Hurst exponent: $H = 0.3$, $H = 0.5$, and $H = 0.7$, as shown in panel (a) of this figure, together with a white noise signal. In panel (b), the degree distribution for the VG generated from the white noise decays exponentially, in agreement with [23]. Also in this panel, it is possible to observe that the higher the Hurst exponent, the heavier the tail of the degree distribution, as expressed by Eq. (4.3).

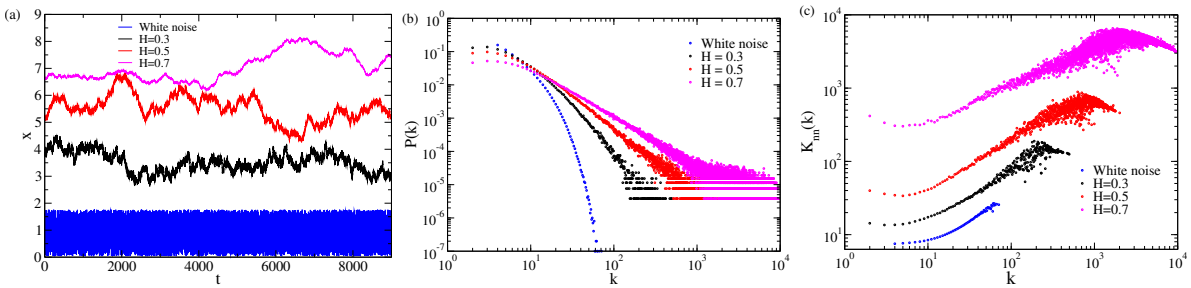

Figure 4.2 – (a) Example of time series of fBM for different values of Hurst exponent H and white noise. Time series were scaled to a variance of 1 and shifted to improve visibility. (b) Degree distribution and (c) average neighbor degree of the corresponding VG of the series shown in (a). Time series of 2^{18} points were considered.

In panel (c) of Fig. 4.2, the average degree of the nearest neighbors as a function of the degrees is presented for the white noise and fBM time series using the different values of the Hurst exponent. This quantity, already discussed in Ch. II, expresses the degree correlations of the network, and a more complex dependence on the degree can be observed compared to the degree distributions. We observe that as the value of H increases, a shift in the behavior of $K_{\mathrm{nn}}(k)$ becomes more evident. For a large range of low degrees, the graph presents assortative degree correlations, passes through neutral assortativity for high degrees, and becomes disassortative for even higher degrees. This happens because, since the fractal time series exhibits peaks and valleys of all scales, peaks of intermediate size can obstruct the visibility of valleys and smaller peaks. This means that the higher a peak is, the more visibility points it can access. Due to the finite length of the series, this hierarchical structure saturates around the correlation time, leading to

the emergence of a neutral regime. Peaks with very large visibility are rare, but they can see wide segments of the series, encompassing many valleys and small peaks with low visibility, which in turn decreases the average visibility of nearby points. This mechanism explains why nodes with extreme visibility exhibit disassortative behavior. As will be discussed in the next sections, these characteristic patterns of the degree correlations will play a central role in our VG analysis.

The fact that the VG inherits properties of the system that generated the time series has led to its use in several applications across very different fields. For instance, the VG approach has been used to analyze geophysical time series [25] and turbulent flows [134]. Additionally, it has been used to investigate Alzheimer's disease through EEG signals [26, 27]. More recently, a modification of the original VG algorithm was employed to investigate cardiac disorders in [28]. Therefore, the VG method has been shown to be applicable in diverse situations.

4.2 Criticality in epidemic models through VG

Determining whether a given time series in a real system is associated with a critical regime may be challenging. However, we found that analyzing the VG metrics can be a handy tool for tackling this issue. We investigated the ASPT present in the CP model through synthetic time series of epidemic prevalence ρ, which is the fraction of infected individuals in the population, as mentioned in Ch. III. The CP model on d-dimensional hypercubic lattices has already been extensively investigated, and the critical points for its dynamics are known with accuracy for different dimensions. Table 4.1 shows the values of the epidemic threshold with uncertainty in the last digit [2].

d	1	2	3	4
λ_c	3.29785	1.64877	1.31686	1.19505

Table 4.1 – Critical point values for CP model in d-dimensional hypercubic lattices with uncertainty in the last digit [2].

Examples of a prevalence time series are shown in panel (a) of Fig. 4.3, in which we computed the quasi-stationary prevalence series for the CP model running on a $d = 2$ lattice of side $L = 500$. Different values of the infection rate were used to address critical and off-critical regimes of the transition. The time series were scaled to unit variance and shifted for better visualization. It is possible to observe that the critical time series present a fractal aspect with a wide range of wavelength fluctuations, while the off-critical ones are

characterized by short-wavelength fluctuations. At this point, it is worth mentioning that for all analyses that follow, we consider time series of $t = 10^6$ points equally spaced with resolution $\delta t = 1$. Also, the measures for the VG were averaged using ten samples of time series to generate the VG. Considerations on finite-size effects of the VG are discussed in Appendix D.

Panel (b) of Fig. 4.3 shows the degree distribution of the VG generated from the time series shown in panel (a). The curves related to the off-critical regimes are very similar, and the black one related to the critical regime shows a slightly heavier tail. Despite this difference, a much more evident distinction can be made through the degree correlations of the VG. To analyze them, we use the average degree of the nearest neighbors, as shown in panel (c) of the same figure. For the three regimes shown in this panel, the VG presents assortative degree correlations for low degrees. However, only the critical curve shows a change in its pattern, approaching a neutral correlation as the degree increases. This behavior is analogous to the one discussed for the fBM time series when compared to the white noise signals. Note that the disassortative regime present in the $H = 0.7$ fBM curve does not happen here due to finite-size effects, but it is expected to be observed in much larger systems and longer series.

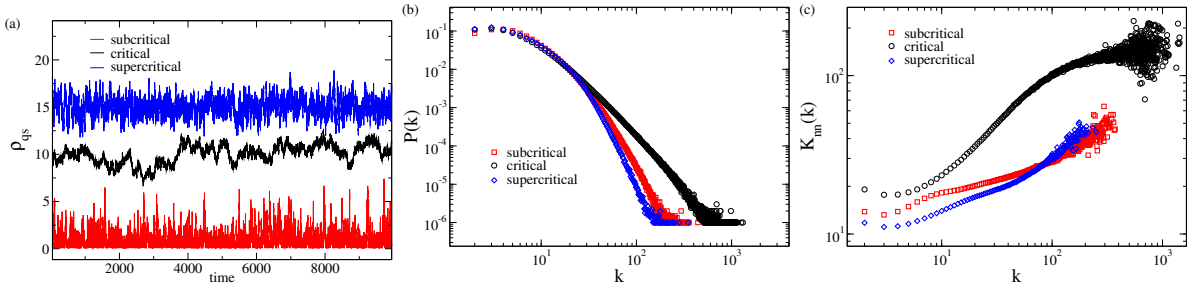

Figure 4.3 – CP model in a two-dimensional lattice of side $L = 500$. (a) Time series of epidemic prevalence for critical ($\lambda = 1.6487$), subcritical ($\lambda = 1.48$), and supercritical ($\lambda = 1.76$) regimes. The time series were scaled to unit variance and shifted to improve the visualization. (b) Degree distribution and (c) average degree of the neighbors for the VGs obtained in subcritical, critical, and supercritical phases. Time series with 10^6 points are considered.

The disassortative pattern expected for VGs generated from time series in the critical regime appears if we increase the dimension of the lattice, as shown in Fig. 4.4. To improve visualization and comparison of the patterns in different dimensions, the curves of $K_{\rm nn}(k)$ were rescaled by 2^{d-1}. At $d = 4$, the VG presents the shift to disassortative degree correlations observed in the fractal time series discussed for the fBM. The upper critical

dimension of the DP universality class is $d = 4$, above which the mean-field exponents hold. In the next section, the same VG analysis will be employed for high-dimensional systems, where the mean-field behavior is expected to be accurate.

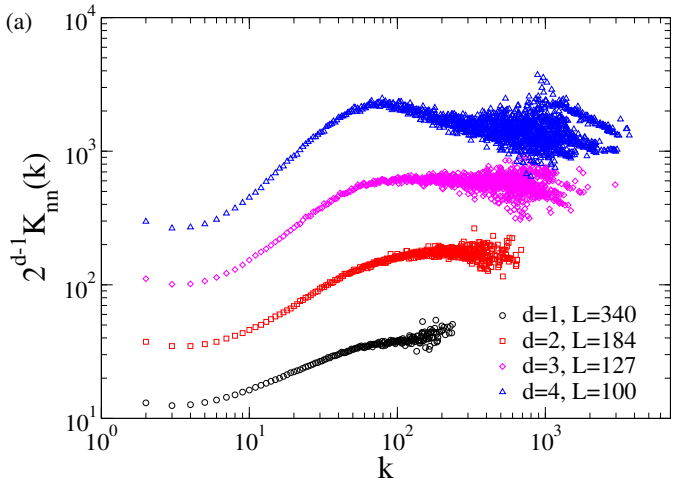

Figure 4.4 – CP model in lattices of different dimensions. The average degree of the nearest neighbors for the VG generated from the time series of prevalence. Curves are generated using different dimensions and sizes, scaled by 2^{d-1} to improve visibility. The sizes are chosen such that $L^z = 10^4$ for all dimensions.

Figure 4.5 shows the results for the CP on a 4-d lattice with size $L = 50$ and different values of infection rate. While the degree distributions of the VGs, in panel (a), do not show an expressive difference in the qualitative behavior for different λ, the degree correlations of the VG, in panel (b), clearly separate between critical and off-critical regimes, even when considering only slightly different values of the infection rate. This characterizes the disassortative VG as a hallmark for critical time series in our analysis [31].

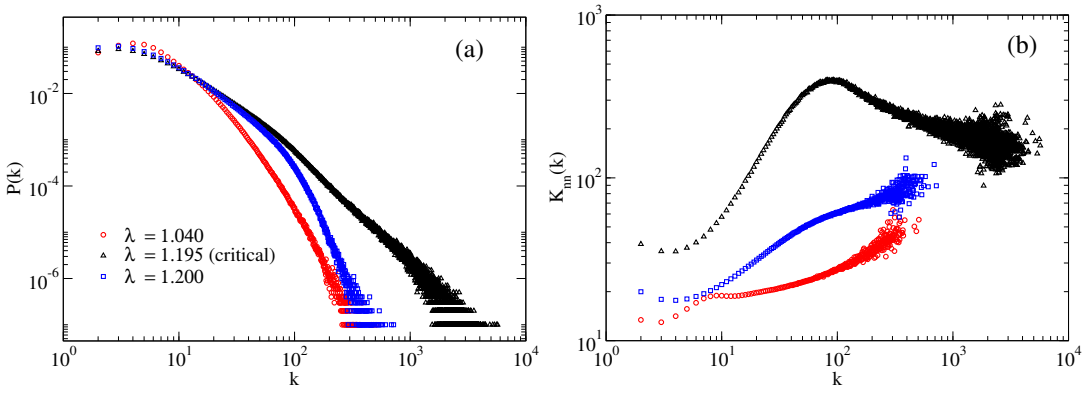

Figure 4.5 – CP model in 4-d lattices with size $L = 50$. Panel (a) shows the degree distributions and panel (b) the degree correlations for the VG generated from the prevalence time series using different infection rates.

We now consider the two-species contact process (2SCP) presented in Ch. III. In this model, depending on the symbiotic healing rate μ_s, the system will undergo a discontinuous phase transition for $d \geq 4$. Time series of prevalence for the 2SCP undergoing discontinuous and continuous transitions were obtained on an RRN of size $N = 10^5$ with degree $q = 4$. A fully active initial state is considered, implying that all nodes are initially doubly occupied, and the steady state corresponds to the upper spinodal (see Fig. 3.7 in Ch. III). Computing the total quasi-stationary prevalence as a function of the infection rate, we can observe the two above-mentioned transitions in panel (a) of Fig. 4.6.

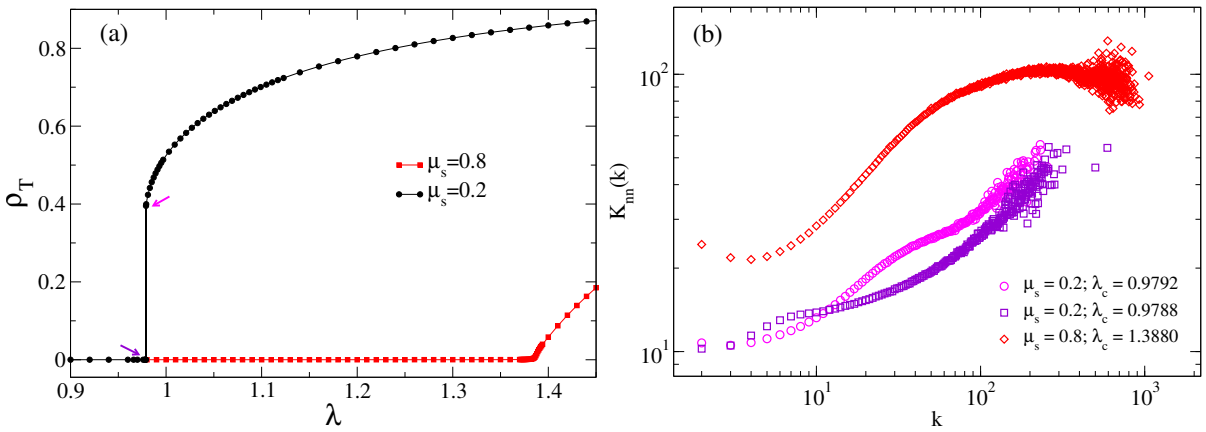

Figure 4.6 – The 2SCP model in a RRN with size $N = 10^5$ nodes and degree $k = 4$. Panel (a) shows the phase transitions in this model for different symbiotic reduced healing rates $\mu_s = 0.8$ (continuous) and $\mu_s = 0.2$ (discontinuous). The degree correlations of VG for the two transitions are shown in panel (b). The transition points for continuous and discontinuous cases are $\lambda_c = 1.3880(5)$ and $\lambda_c = 0.9790(2)$, where uncertainties in the last digit are given in parentheses. Two curves are presented for the discontinuous case: one slightly below and the other slightly above the transition point.

The degree correlations of the VG generated from time series in both examples of transitions are shown in panel (b) of Fig. 4.6. While the curve for the continuous transition exhibits the asymptotic disassortative degree correlations typical of critical series, the same does not happen for the discontinuous transition. Time series taken using values slightly above and below the transition point generate VG that exhibit only assortative patterns. Thus, even close to the transition point, no disassortative degree correlations can be observed in the 2SCP model. This evidence shows how the VG method is also able to distinguish between a critical and a noncritical ASPT.

Now, we confront two different structures for the epidemic model to evolve: a 2-d lattice and a RRN, both homogeneous and having the same degree $q = 4$. The

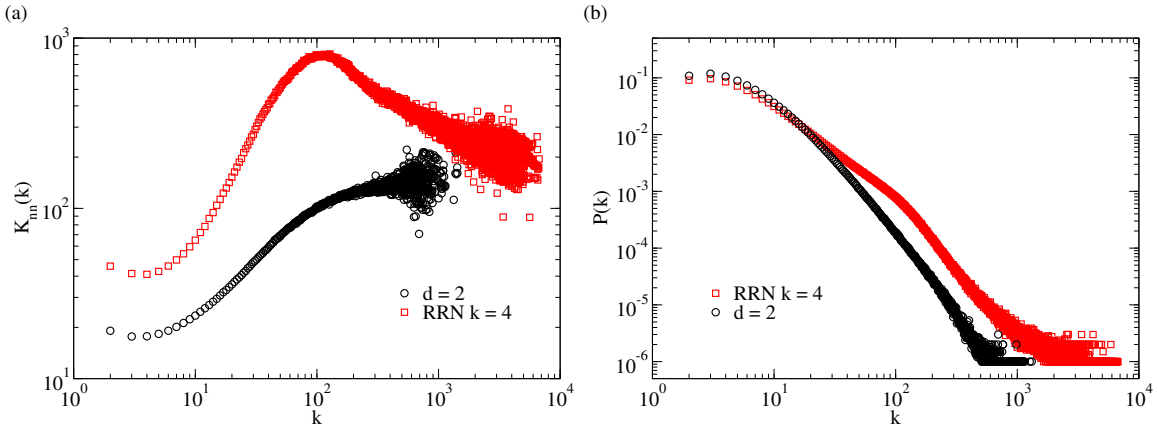

Figure 4.7 – Comparison of the CP model on RRN and a square lattice, both having $k = 4$ nearest neighbors. (a) The average degree of the nearest neighbors and (b) degree distribution of the VGs are presented. The system size is $N = 10^7$ nodes for RRN ($\lambda_c = 1.25808$) and $N = 500 \times 500$ for the square lattice ($\lambda_c = 1.64877$). An average over ten time series with 10^6 points.

degree distributions of the VG generated from the critical time series related to the CP in these structures do not show a significant difference in their patterns, as shown in panel (b) of Fig. 4.7. On the other hand, very distinct outcomes are observed in the degree correlations in panel (a) of the same figure, with the curve for the RRN obeying the signature conjectured for critical time series. This result highlights the potential of the degree correlations in identifying criticality in the time series when compared to the degree distributions.

4.3 Investigating localization in the original networks using VG

The previous section focused on identifying critical time series generated by dynamical processes evolving on homogeneous structures, such as lattices and random regular networks. Now, we extend this analysis by considering heterogeneous substrates for the epidemic models to evolve, in order to investigate how the original network structure influences the critical signature of the VG degree correlations. The results in this section are published in [32].

As discussed in Ch. III, the presence of hubs and densely connected nodes in networks directly influences the mechanisms of epidemic activation [123]. Furthermore, in low-dimensional systems, structural disorder can affect critical phenomena by altering the nature of the phase transition, either through the smearing of the critical point [109] or the introduction of Griffiths phases [135]. In this section, we consider only complex

networks (high-dimensional), where disorder effects are not expected to play a significant role in changing the criticality of the system in the thermodynamic limit. However, these disorder effects remain important to analyze due to finite-size effects in the network sizes we simulate. Therefore, accounting for localization and disorder in the original heterogeneous network is necessary when investigating its criticality.

Let us begin by considering collective activations of epidemics, in which the transition from an absorbing phase to an active one occurs due to contributions from a finite portion of the network to the fluctuations of the order parameter. This type of transition is observed in the SIS model on homogeneous structures. Since all nodes have the same degree k, the SIS model maps onto the CP critical dynamics, differing only in the epidemic threshold, given by $\lambda_{c_{SIS}} = \lambda_{c_{CP}}/k$ [110]. Figure 4.8 presents the analysis of the SIS model on an RRN. In panel (a), the transition is depicted through the average quasi-stationary prevalence and the susceptibility, both as functions of the infection rate, with the latter peaking at the critical point. Panel (b) shows the degree correlations of the VG generated from the prevalence time series using different values of the infection rate. Once again, we observe the degree correlation as an indicator of critical time series, with the asymptotic disassortativity standing out as a hallmark of criticality. For the remaining analyses, only time series in the critical regime will be considered.

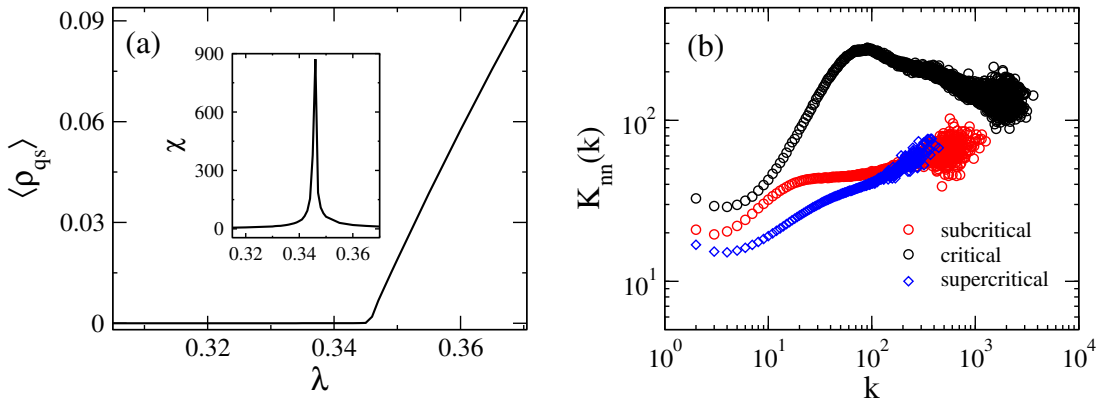

Figure 4.8 – The SIS model in a RRN of size $N = 10^6$ and degree $k = 4$.(a) Average quasistationary prevalence (the order parameter) as a function of the infection rate. The inset shows that the susceptibility as a function of the infection rate presents a peak at the critical value $\lambda = \lambda_c$. (b) Average degrees of the nearest neighbors of the VG generated from the prevalence time series in subcritical ($\lambda = 0.34$), critical ($\lambda = 0.346$), and supercritical ($\lambda = 0.352$) regimes.

Collective activation can also be investigated in heterogeneous networks, for which we considered two cases. The first is the SIS model on annealed networks with a power-

law degree distribution, where node connections are probabilistic and rewired at each time step. In this setting, collective activation occurs because all nodes interact with each other. The second case is the CP model on networks generated by the UCM model, which is known to exhibit collective activation at a finite epidemic threshold [121]. The VG generated from critical time series in these two cases yields degree correlations shown in Fig. 4.9. The asymptotic disassortative behavior of the average degree of nearest neighbors becomes more evident as the size of the original network increases, for both (a) the SIS model on an annealed network and (b) the CP model on a quenched scale-free UCM network. Therefore, for collective activation, the heterogeneity in the network does not alter the criticality signature of the VG degree correlations.

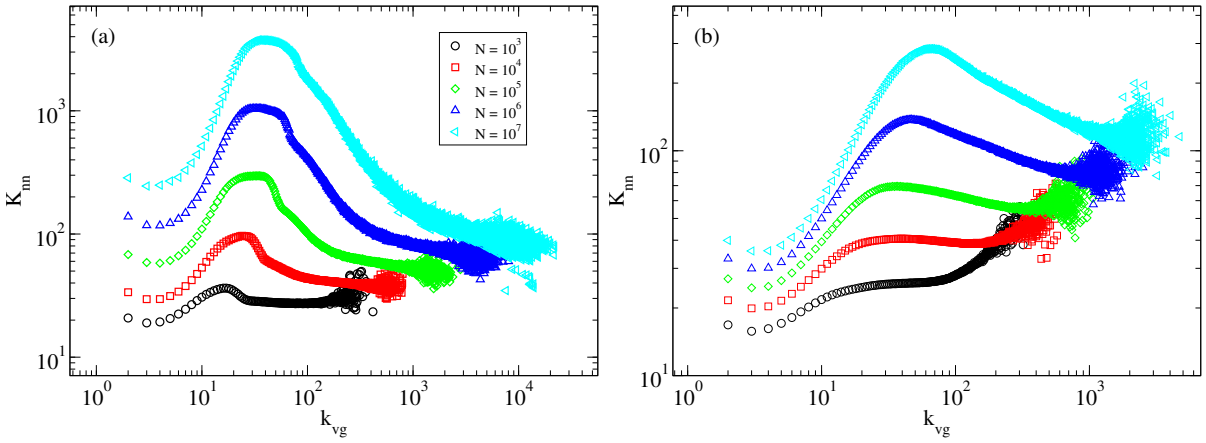

Figure 4.9 – Analysis for collective activation. Average degree of the nearest neighbors of the VG generated from the critical time series of (a) the SIS model on annealed and (b) the CP model on quenched UCM networks of different sizes N, both with power-law degree distribution with exponent $\gamma = 2.75$, minimal degree $k_0 = 3$, and upper cutoff $k_c = 2\sqrt{N}$. Averages over ten time series of $t = 10^6$ points were considered for a single substrate network realization.

Now, let us consider the SIS model in quenched heterogeneous networks, such as those generated by the UCM model with a power-law degree distribution. In these networks, subextensive parts play an important role in the activation mechanisms. Considering UCM networks with exponent $2 < \gamma < 2.5$, the epidemic is activated within a densely connected structure that contains the hubs. This structure can be identified by computing the maximum k-core decomposition, as mentioned in Ch. III. In this case, the hubs interact directly within this innermost core and spread the epidemic to other parts of the network. In our analysis, we used a UCM network with exponent $\gamma = 2.25$ and various sizes. Panel (a) of Fig. 4.10 shows the degree correlations for the VG generated

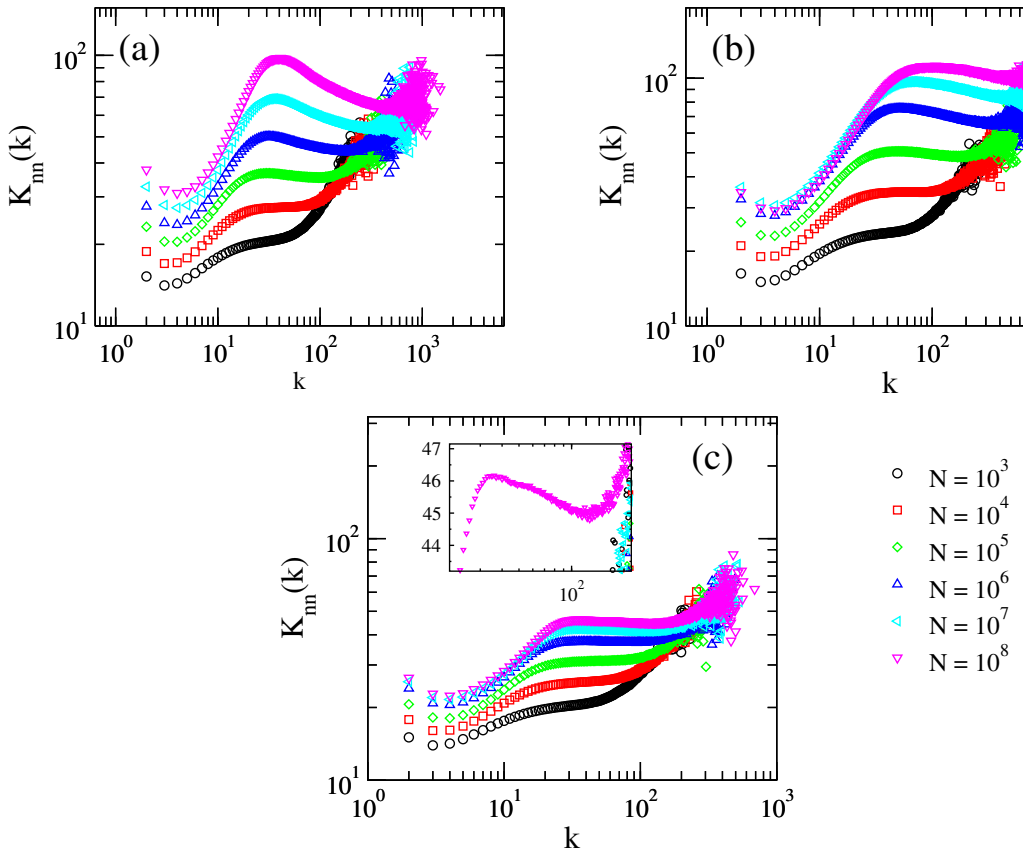

Figure 4.10 – Average degree of the nearest neighbors for the VG generated from critical time series of prevalence for the SIS model in UCM networks of different sizes with exponent (a) $\gamma = 2.25$, (b) $\gamma = 3.5$, and (c) $\gamma = 2.75$. The inset in (c) shows a zoom for the $N = 10^8$ network, with a semi-log scale. For $\gamma < 3$, a structural cutoff $k_c = 2\sqrt{N}$ is used while a rigid cutoff $k_c = 3N^{1/\gamma}$ is considered for $\gamma = 3.5$. Averages over five samples of substrate networks for each size and ten time series with $t = 10^6$ points were considered.

from the SIS model in these networks. It is possible to observe a critical behavior very similar to the collective case, with disassortative degree correlations emerging asymptotically for large degrees. The scenario starts to change when we use UCM networks with $\gamma = 2.75$, in which the activation mechanism is triggered by long-range mutual infections among the hubs. It is worth noting that in these networks, the hubs are sparsely distributed, so the SIS dynamics will generate loosely interacting regions composed of the hubs and their neighbors. In these regions, the epidemic activity will be localized and will persist for long periods, which grow exponentially with the hub degree. This mechanism allows the infection to spread among the hubs through paths of nodes with low degree. The behavior of VG degree correlations for SIS in these networks can be observed in Fig. 4.10(c). A neutral pattern emerges in the average degree of the nearest neighbors, and a disassortative behavior is observed only for sizes $N = 10^8$, as shown in the inset.

For the $\gamma > 3$ case, the networks will present outliers with degrees much larger than the other nodes in the network. This occurs due to their highly fluctuating natural cutoff, $\langle k_{\max} \rangle \sim N^{1/(\gamma-1)}$, which is much smaller than the structural cutoff we used for the other UCM networks, $k_c = 2\sqrt{N}$. This case leads to multiple transitions and strong localization in the network, and it will be addressed separately later in the text. Therefore, to handle this issue, we first consider a rigid cutoff for the degrees as $k_c = N^{1/\gamma}$. This substantially suppresses the fluctuations, allowing us to unambiguously determine the epidemic threshold for generating the VG. The results for SIS with $\gamma = 3.5$ and a rigid cutoff are presented in Fig. 4.10(b), and the behavior of the degree correlations is very similar to the $\gamma = 2.75$ case. These last two results provided an insight: the localization generated by the sparsely distributed hubs was blurring the criticality signature we have observed, with the disassortative correlations barely appearing only in the largest investigated size.

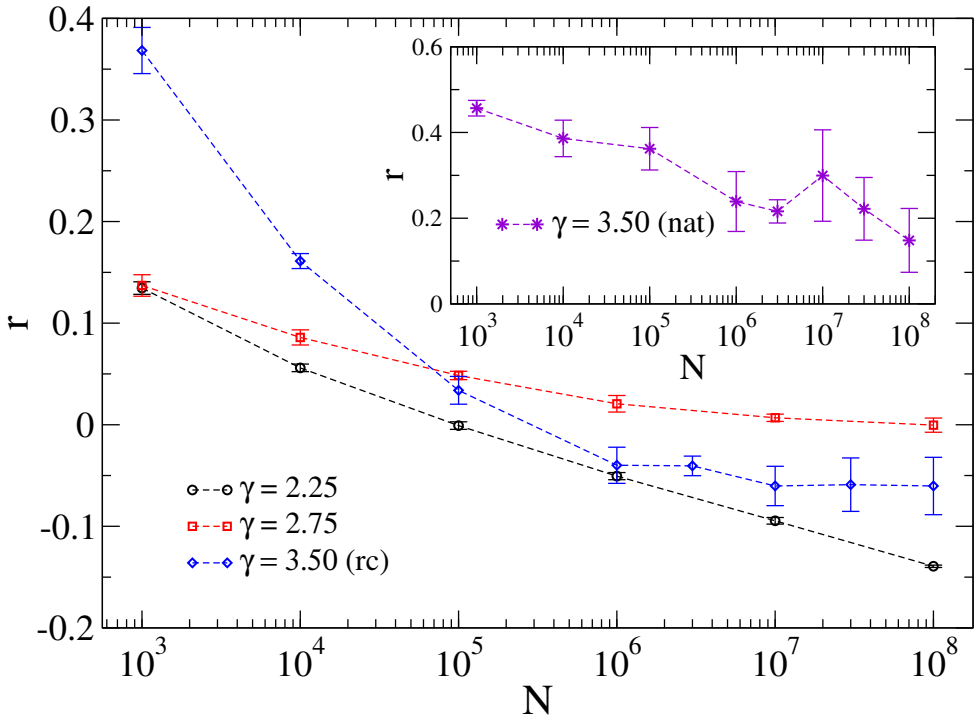

Figure 4.11 – Pearson correlation coefficient of the VG as a function of the network size for the critical time series obtained with SIS dynamics on UCM networks of different degree exponents. Structural ($k_c = 2N^{1/2}$) and rigid ($k_c = 3N^{1/\gamma}$) cutoffs were used for $\gamma < 3$ and $\gamma > 3$, respectively. The inset shows the Pearson coefficient for the VG corresponding to the UCM network with $\gamma = 3.5$ and natural cutoff. Averages over five samples of networks for each size and ten time series with $t = 10^6$ points were considered.

Still working with the UCM networks discussed earlier, we observe in Fig. 4.10 that the criticality signature is not evident for $\gamma > 2.5$, but it is expected to emerge for sufficiently large systems. To analyze the possibility of disassortative degree correlations emerging asymptotically, we computed a modified version of the Pearson coefficient (r), discussed in Ch. II. This coefficient indicates assortativity (disassortativity) if $r > 0$ ($r < 0$), and neutral correlations if $r \approx 0$. For analyzing the multiple pattern shape of the curves of degree correlation of the VG, we define the partial Pearson coefficient determined from the degree distribution $P(q)$ and the average nearest neighbors $K_{nn}(q)$ as [10]:

$$r = \frac{1}{\sigma^2}\frac{\langle q^2\rangle}{\langle q\rangle}\left[\frac{\langle K_{nn}q^2\rangle}{\langle K_{nn}q\rangle} - \frac{\langle q^2\rangle}{\langle q\rangle}\right], \tag{4.4}$$

in which

$$\sigma^2 = \frac{\langle q^3\rangle}{\langle q\rangle} - \frac{\langle q^2\rangle^2}{\langle q\rangle^2}. \tag{4.5}$$

Here, $\langle\cdots\rangle$ means partial average constrained to $q > q_0$:

$$\langle f\rangle = \sum_{q=q_0}^{q_{\max}} f(q)P(q) \tag{4.6}$$

where q_0 is a lower bound degree chosen to exclude the lower degree nodes. The standard Pearson coefficient is recovered when $q = q_{\min}$. Using the expression defined by Eq. (4.4), we analyzed the finite-size scaling of this partial Pearson coefficient, as shown in Fig. 4.11. There is a pattern change that always occurs in the VG: it starts with assortative correlations and then shifts to disassortative or neutral behavior. To account that, we set $q_0 = 2\langle k_{\rm VG}\rangle$ for the scale-free UCM networks and $q_0 = 6\langle k_{\rm VG}\rangle$ for those with $\gamma = 3.5$. This choice ensures the exclusion of the initial assortative degree correlation regime, which is common to all VG (critical or not). In this figure, we observe that for $\gamma = 2.25$, a negative coefficient arises even in small networks and becomes more negative as the size increases, confirming the criticality signature. To analyze the case of $\gamma > 2.5$, we use an extrapolation considering $r = r_\infty + aN^{-b}$, which shows that the coefficient converges very slowly towards a value slightly negative $r_\infty \approx -0.023$ for sizes $N > 10^8$. For $\gamma = 3.5$ with a rigid cutoff, a more disassortative coefficient $r_\infty \approx -0.087$ is obtained, while for the case $\gamma = 2.25$, a high disassortative VG with $r_\infty \approx -0.37$ is found. The exponent b in finite-size scaling is not a universal quantity. This analysis provides better intuition about how the criticality signature emerges asymptotically in the networks investigated. Still,

a question remains: how is localization interfering with the visualization of the critical behavior?

Delving deeper into the localization effects, we now analyze the case of the UCM network with $\gamma > 3$ and a natural cutoff for the degrees. In these networks, the sparsely distributed outliers lead to independent active domains in the subcritical regime, which can be observed as multiple peaks in the susceptibility curves [136]. These multiple transitions are shown in the top panel of Fig. 4.12, where we used three different network samples of size $N = 10^7$. We selected three samples as examples because these networks may present outliers of very different sizes, resulting in distinct localization patterns across samples. Two well-resolved peaks can be seen in panel (c) of this figure: the first corresponds to the activation of outliers, while the second is associated with the activation of the whole network. The arrows in these panels indicate the infection rate values used to generate the VG, whose degree correlations are shown in the bottom panels (the arrow colors match the $K_{\mathrm{nn}(k)}$ curves). The bottom panels display only assortative degree correlations, which were previously associated with off-critical regimes. Even when outliers are absent, as in panel (b), disassortative correlations are not observed. This analysis is complemented by the finite-size scaling of the partial Pearson coefficient, shown in the inset of Fig. 4.11. This inset reveals large error bars across the five network samples analyzed, and it remains unclear whether the coefficient will decay to a negative value for sizes larger than $N = 10^8$. Thus, we observe that the localized activity produced by the outliers blurs the criticality signature in the network sizes investigated.

An extreme case of strong localization can be investigated by considering an RRN containing a hub with degree $k_{\mathrm{hub}} = \sqrt{N}$. Here, we aim to mimic the behavior observed in the analysis of $\gamma = 3.5$ and natural cutoff networks, but in a simplified network where local and global activation can be clearly separated, as shown in Fig. 4.13. The inset of this figure shows that, as expected, the local activation of the network (marked by the blue arrow) leads to an assortative VG. However, the critical pattern changes drastically compared to a pure RRN (see Fig. 4.8). We observe that, even though the global transitions in both cases of RRN (pure and with hub) occur at the same epidemic threshold, the disassortative correlations do not appear when the network is affected by strong localization, such as the presence of a hub. This demonstrates how localized structures in the original network can alter the criticality signature in the system.

As our final analysis, we consider a type of disorder, which may replace the critical

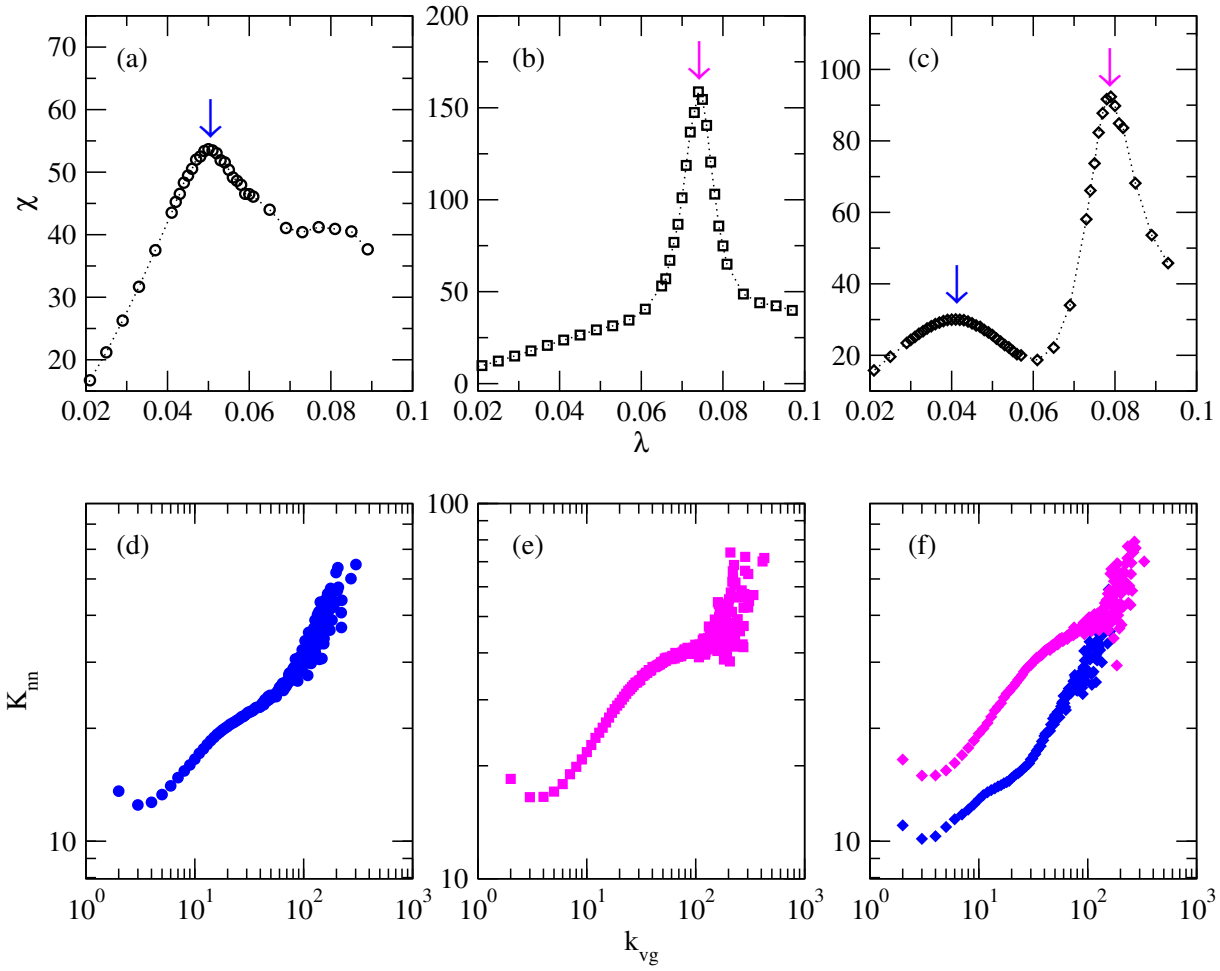

Figure 4.12 – Top panels: susceptibility as a function of infection rate for an SIS model in three different samples of UCM networks with degree exponent $\gamma = 3.5$, a natural cutoff, and size $N = 10^7$. Bottom panels: average degree of the nearest neighbors for the VGs generated from the time series computed at the infection rates given by the susceptibility peaks indicated by the arrows in the top panels. A total of ten time series with $t = 10^6$ points were considered for a single substrate network realization.

point with an extended region of criticality, known as Griffiths phases. This situation arises when the disorder is strong enough to create regions in the network that activate independently. A model exhibiting a GP, discussed in Ch. III, is the diluted or quenched contact process (QCP). We evolve the QCP on ER networks of size $N = 10^5$ with a dilution parameter $q = 0.9$, which produces a well-resolved extended critical region[2]. The inset of Fig. 4.14 shows the prevalence power-law decay for $\lambda = 20$, averaged over 10^3 dilution realizations with a fully active initial state. The colored curves overlaid on the black averaged curve represent five sample realizations, illustrating the decay for

[2] This extended region can be observed in Fig. 1 of Ref. [14].

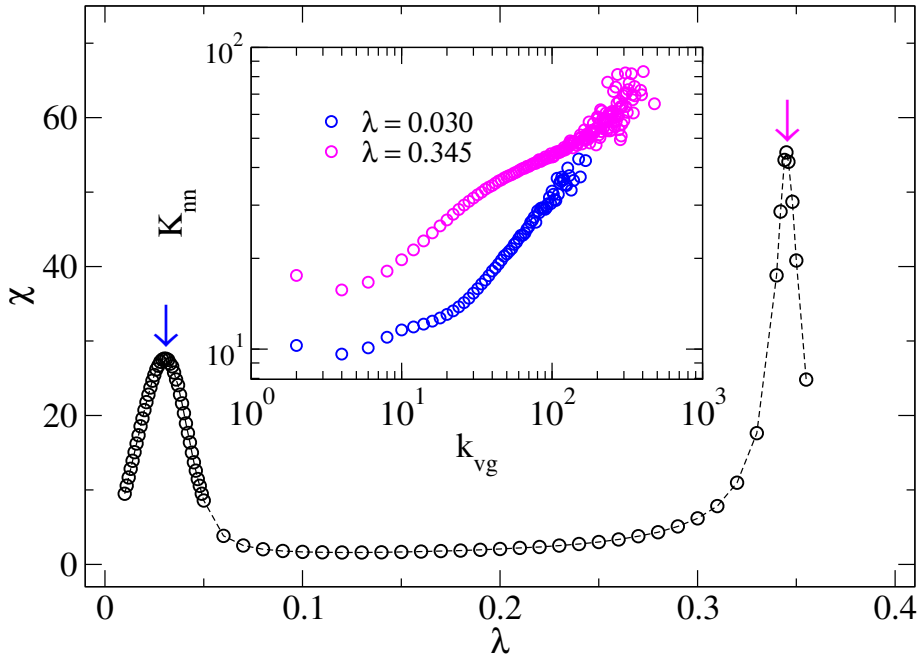

Figure 4.13 – Susceptibility as a function of the infection rate for the SIS dynamics on a RRN of size $N = 10^7$ where all nodes have degree $k = 4$ except a hub with degree $k_{\text{hub}} = \sqrt{N}$. The inset shows the average degree of the nearest neighbors for the VG generated from the prevalence time series computed with the infection rates corresponding to peaks of susceptibility shown in the main panel. A total of ten time series with $t = 10^6$ points were considered for a single RRN realization.

individual disorder samples. The time series, taken in the quasi-stationary regime, were used to compute the VG and their respective degree correlations, as shown in the main plot of Fig. 4.14. All samples exhibit strong assortativity. This highlights a substantial difference compared to the critical signatures of the standard CP (see Fig. 4.9(b)). The localization induced by disorder in this model drastically alters the degree correlation patterns, shifting them to assortative, in a clear analogy to the strong localization caused by outliers.

Therefore, we observe that strong localization, whether caused by outliers or other types of disorder, can blur the criticality signature in the time series, even when the system is poised at the actual critical point (or within a critical region). However, the VG method remains effective for detecting criticality through time series in systems with structural heterogeneity, if localization is not extreme. False negatives may occur when critical systems are subject to strong localization. Nevertheless, the method did not yield any false positives; whenever the criticality signature appeared, the system was indeed critical.

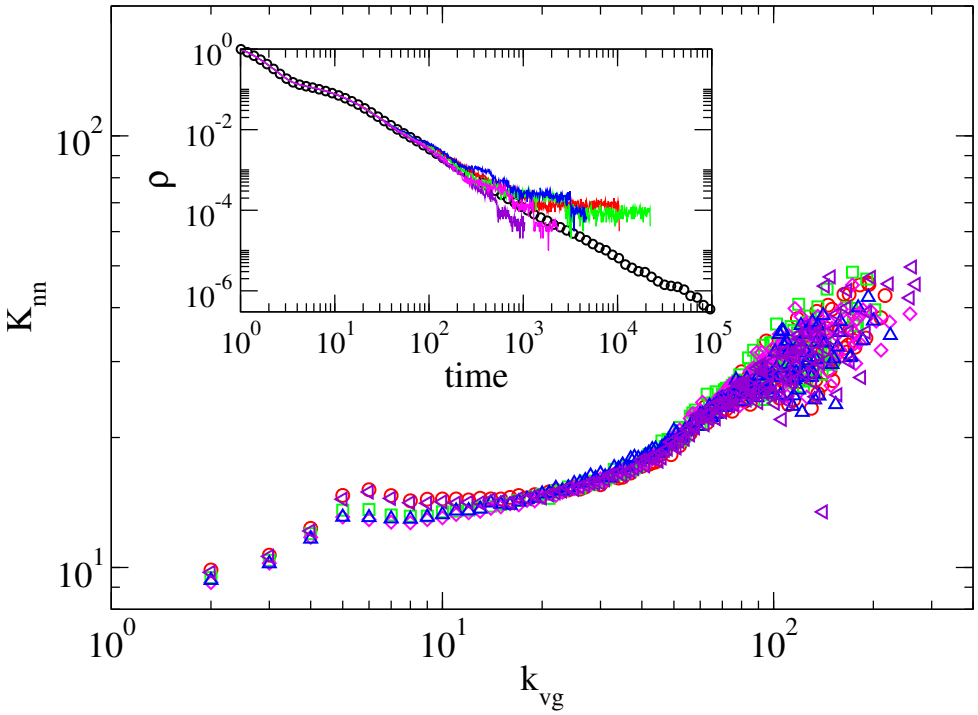

Figure 4.14 – Average degree of the nearest neighbors for VGs generated from the quasi-stationary time series of prevalence for the five disorder realizations shown in the inset. The inset shows the prevalence decay over time for a diluted contact process in an Erdős-Rényi network with size $N = 10^5$ and average degree $\langle k \rangle = 3$ using an infection rate of $\lambda = 20$ and dilution $p = 0.9$. In the inset, the black symbols are an average over 10^3 dilution realizations, which present the power-law decay, while curves depicted by lines of different colors show the decay for five randomly chosen dilution realizations.

4.4 Concluding remarks

The VG mapping has emerged as a modern approach for time series analysis. In this chapter, we aimed to explain its construction and demonstrate its applicability across diverse fields of investigation. Additionally, we explored the use of VG in analyzing a specific complex system: epidemic spreading on networks. We showed how degree correlations can capture features of the original system that the degree distribution does not accurately distinguish. We presented the disassortative degree correlations of the VG as a hallmark of criticality and extended this analysis to cases where criticality may be blurred by strong localization effects. As a future perspective for the work detailed in this chapter, we intend to apply the VG degree correlation method to investigate time series generated from real systems.

V Intermittent Networks

The previous chapter investigated spreading phenomena on static networks to generate time series of epidemic prevalence. Still within the context of epidemic propagation, some questions may arise. What is more effective in avoiding contagion: reducing the number of contacts for long periods or entering quarantine for shorter durations? These questions involve the duration of social interactions, which static approaches cannot adequately account for. Therefore, in the present chapter, a simple approach for temporal networks will be considered.

In 2020, the world faced a severe pandemic scenario when it was urgent to determine which strategy would prevent economic collapse while ensuring that hospitals could meet the demand for healthcare assistance. Research on complex networks and epidemic spreading has played a fundamental role in providing insights into this issue [64]. As already elucidated in the previous chapters, the network structure is crucial for understanding the evolution of disease spread [113]. However, static models do not capture one of the essential aspects of social interaction: the temporal dimension.

The temporal aspects of interactions are important not only for considering the sequence of events but also for accounting for their duration. When dealing with disease propagation, the duration of an interaction is decisive for infection. However, our contacts are not uniformly distributed over time. For instance, the duration of social contacts observed in real data may be highly heterogeneous, with interactions happening in bursts [38, 39]. In general, an individual spends much more time in contact with their friends and work colleagues than with their dentist or a delivery driver. Yet, a delivery driver has many short-term interactions. Could this be relevant in disease-spreading dynamics?

Therefore, we aim to study a network structure that accounts for the temporality of interaction sequences and their duration. We investigate the effects of contact reduction versus the restricted isolation of individuals by introducing temporal dynamics in links and nodes, respectively. Furthermore, this work also takes a theoretical approach concerning criticality. By investigating intermittency in lattices, we aim to verify whether the absorbing phase transition present in the SIS model changes its critical exponents in comparison to the SIS model in static lattices. This analysis raises the possibility of temporal Griffiths phases (TGP) [40] arising from temporal disorder introduced by intermittency.

5.1 Temporal network approach based on renewal theory

As discussed in Chapter III, network epidemiology was a hallmark in introducing a new way of understanding disease spreading. Considering static networks made it possible to infer many crucial characteristics of spreading phenomena, such as the measurement of the epidemic threshold, for instance [30]. Although this approach remains relevant, more realistic scenarios include the consideration of temporal interactions between individuals. Temporal networks, also known as time-varying or temporally varying networks, describe many real systems in which the number of links or nodes changes over time, or situations where the rate of link activation is time-dependent [36]. Temporal networks naturally slow down disease spreading [137, 138], since contacts are interrupted, meaning that static models tend to overestimate disease spread [34].

One possible way to incorporate time into network modeling is to consider a static structure as a substrate and allow contacts to evolve under some dynamical process [139]. A static distribution of contacts is suitable since, for many social networks, contacts do not significantly change over time. Even though the birth and death of links can be considered for certain applications [35], individuals tend to maintain a relatively stable number of well-established contacts, or even fixed ones, as in static networks. The strategy is then to consider that these contacts are not active all the time. We investigated two ways to implement temporality: by applying the activity change process to either the nodes or the links. Activity here is related to the two possible states: the node or link can be active in the network and thus can participate in the occurring dynamics. If the node or link is inactive, it is as if it were momentarily removed from the network, since it will not participate in the dynamical process. We refer to networks following this procedure as **intermittent networks**.

As illustrated in Fig. 5.1, starting with a predefined network structure, we can define node-intermittent (NI) or link-intermittent (LI) networks. In the former case, nodes follow a dynamic activation/inactivation process. When a node is inactivated, all its associated links are automatically inactivated as well. This would correspond to a complete quarantine of an individual during a time interval. The second possibility addresses temporal dynamics of the links, where only a reduction in an individual's contacts occurs.

This framework has already been explored, focusing solely on the link turnover approach [140], highlighting the differences between non-Markovian epidemic models and

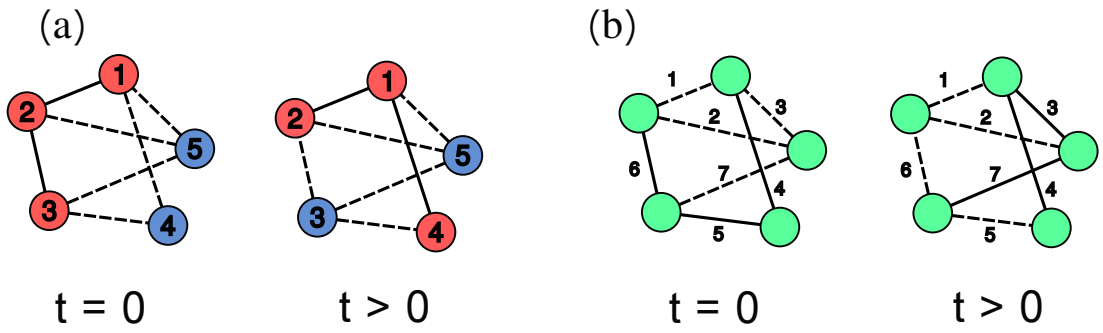

Figure 5.1 – Illustration of intermittent networks. Node intermittency is considered in (a), in which the red nodes are active and the blue ones are inactive. For link intermittency in (b), the continuous lines represent active links, and the inactive ones are dashed lines.

non-Markovian temporal networks. The node turnover perspective was examined by considering a dynamic temporal network [141] theoretically and using real-data interactions for setting the temporal parameters [142]. However, to the best of our knowledge, no study has been dedicated to comparing these two previously mentioned approaches. According to our findings, the activity patterns of nodes are extremely important for spreading, whereas link intermittency induces only trivial changes in the epidemic scenario. This will be discussed in detail in this chapter.

Introducing intermittency in the dynamics of the network seems straightforward since many examples of bursting sequences can be found in real data. Burstiness, or bursty behavior of a system, can be defined as the intermittent change in activity or the frequency of events. An event can be, for instance, the contact between two individuals or an email being sent [37]. One of the first observations of an inter-event time distribution exhibiting a power-law tail was in email exchanges [143]. This behavior has also been observed in mobile phone calls [144, 145] and face-to-face interactions between individuals at academic conferences [38] and among high school students [39].

In our method, events are defined as changes in the state of a link or node. An illustrated example is shown in Fig. 5.2, where nodes and links alternate between active and inactive states over time. We begin by randomly assigning the states of nodes or links so that, at the start of the dynamic process, the states are uniformly distributed. Note that this approach, differently from the previous studies [140, 141], the events are not the contact sequences, but the changes in the state of a node or link. This perspective captures the essence of the original idea of this work, which is to consider the duration of

interactions. Additionally, we ensure that the number of contacts and individuals remains constant, so that no new nodes are added nor new connections are created.

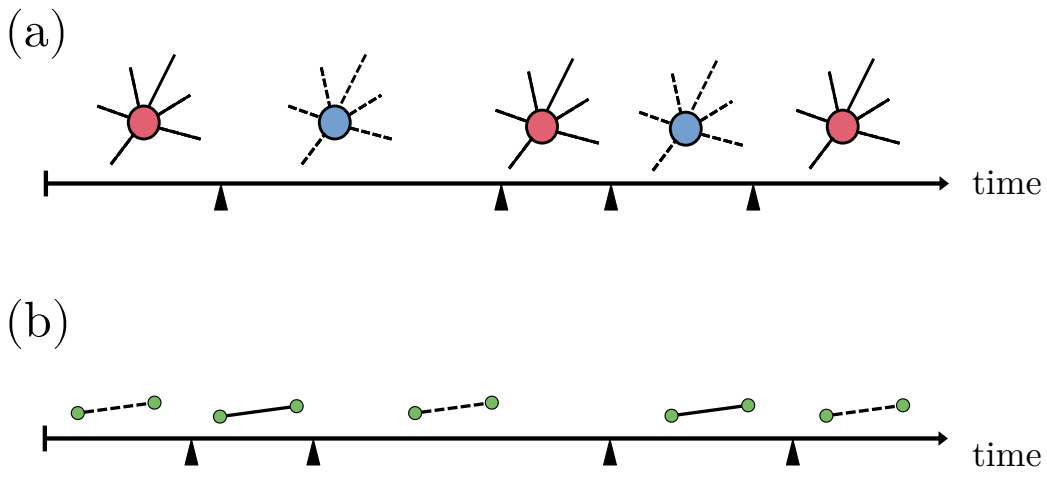

Figure 5.2 – Representation of intermittent events. The events are the change of state of a node or link, pictured by the black arrows pointing to the line. For NI in (a), the red nodes are active, and the blue ones are inactive. In (b), the LI is represented by an active link with a continuous line and an inactive one with a dashed line.

Let us analyze possible temporal distributions of interactions. Some models consider that human activity happens at a constant rate, meaning that the events follow Poissonian distributions over time [146]. Once these events are stochastically distributed, they can be characterized as a point process. The time interval between two events is called waiting time or inter-event time. Uniformly random activity can be modeled by the Poisson process, in which the probability of an event occurring is Markovian or time-independent [35].

5.1.1 Poisson Process

Considering Δt as the time window duration between events, q is defined as the probability that an event occurs inside Δt. Thus, the rate for an event to occur is $\alpha = q/\Delta t$, which is well-defined if $q \to 0$ as $\Delta t \to 0$. This implies that, for sufficiently small Δt, no multiple events happen and the event sequence follows a Poisson process [36].

It is simple to derive the inter-event time distribution, named $\psi(\tau)$, in a Poisson process. If the probability of observing n events in the $[0, t]$ time window is $p(n, t)$ we have $q = p(1, \Delta t) = \alpha \Delta t$ and also $1 - q = p(0, \Delta t) = 1 - \alpha \Delta t$. Thus, for $n \geq 1$,

$$p(n, t + \Delta t) = \underbrace{p(n, t)p(0, \Delta t)}_{n \text{ events in } [0,t] \text{ and no event in } [t, t+\Delta t]} \underbrace{+}_{\text{or}} \underbrace{p(n-1, t)p(1, \Delta t)}_{n-1 \text{ events in } [0,t] \text{ and one event in } [t, t+\Delta t]} , \tag{5.1}$$

leading to the following

$$p(n, t + \Delta t) = p(n, t)(1 - \alpha \Delta t) + p(n - 1, t)\alpha \Delta t \ . \tag{5.2}$$

Reorganizing the terms and taking $\Delta t \to 0$, we get the master equation for a Poisson process as

$$\frac{dp(n, t)}{dt} = \alpha p(n - 1, t) - \alpha p(n, t) \ . \tag{5.3}$$

If $n = 0$, the first term on the right is zero, and the remaining equation can be solved considering that no event occurs in $t = 0$, that is to say $p(0, 0) = 1$. The solution gives

$$p(0, t) = e^{-\alpha t}, \tag{5.4}$$

which is the probability that no event occurs in $[0, t]$. Thus, according to equation 5.2, the probability that the first event happens in $[t, t + \Delta t]$ is $p(0, t) - p(0, t + \Delta t)$. Applying this idea to the inter-event time between two consecutive events τ, we get

$$p(1, \tau + \Delta t) = p(0, \tau) - p(0, \tau + \Delta t). \tag{5.5}$$

Considering the distribution of the inter-event times to be $\psi(\tau) = p(1, \tau + \Delta t)/\Delta t$, it follows that

$$\psi(\tau) = -\frac{dp(0, \tau)}{d\tau}, \tag{5.6}$$

because

$$\frac{dp(0, \tau)}{dt} = \lim_{\Delta t \to 0} \frac{p(0, \tau + \Delta t) - p(0, \tau)}{\Delta t} \ . \tag{5.7}$$

Hence $\psi(\tau) = \alpha e^{-\alpha \tau}$, meaning that the inter-event times in a Poisson process follow an exponential distribution.

The average inter-event time is given by

$$\langle \tau \rangle = \int_0^\infty \tau \psi(\tau) d\tau \ . \tag{5.8}$$

Thus, for the exponential distribution, $\langle \tau \rangle = 1/\alpha$, and this is to say that the events occur randomly but at a constant rate α. However, this is violated in many examples of real data [37], and it is necessary to consider an extension of the Poisson process called **renewal process**.

5.1.2 General distribution of inter-event times

As the data availability improved in both quantity and quality, more evidence emerges contrasting with Poissonian models for human activities [37]. From e-mail exchanges [143] to phone calls [145], the inter-event intervals between these actions seem to follow heavy-tailed distributions. The reasons for the emergence of this behavior point to, among other possibilities, a priority-based queuing dynamic that people tend to follow [147]. The aim of this chapter is not to investigate the mechanisms that generate the bursting interactions but to understand how they affect the dynamic processes underlying these interactions.

An interesting example is the spread of computer viruses. For real data on email exchanges, it was shown that the long waiting times between the sending of emails directly influence the duration of computer virus outbreaks [148]. Furthermore, it is important to note that, differently from biological viruses, computer viruses do not undergo genetic mutations. However, their general behavior is similar, emphasizing that understanding human interactions is crucial to multiple types of spreading phenomena.

One possible way to model inter-event times following heavy-tailed distributions is by turning to renewal processes[1]. Considering events that occur randomly in time, the renewal property establishes that different inter-event times τ are independent of each other and follow the same distribution $\psi(\tau)$. If $\psi(\tau) = \alpha e^{-\alpha\tau}$, the Poisson process is recovered, but if $\psi(\tau) = \delta(\tau - \tau_0)$, the events occur periodically [36].

Fig. 5.3 illustrates the difference between homogeneous and heterogeneous distributions of events, both with the same average inter-event time. In the first case, a Poisson

[1] A complete and mathematically rigorous approach to renewal processes can be found in [149].

process, the events are almost evenly spaced over the timeline, whereas in (b), they occur in bursts, with long waits between some events.

Figure 5.3 – Representation of events generated by (a) exponential and (b) power-law distributions, both with the same average inter-event time $\langle\tau\rangle = 0.1$. The power law distribution follows Eq. (5.10), and the parameters are $\beta = 2.5$ and $\tau_0 = 0.01$.

In other chapters, power laws were introduced for generating heavy-tailed distributions in the degrees of the nodes, for example. In the context of events randomly distributed over time, distributions as $\psi(\tau) \sim \tau^{-\beta}$ are known to provide bursts of activity, and the exponent may vary as $1 \leq \beta \leq 2.7$ in some examples of real data [147, 150].

Therefore, this inter-event time distribution will dictate the activity pattern of either nodes or links in our simulations. By changing the exponent β, we can tune how heterogeneous the interactions are. For instance, for $2 < \beta < 3$, besides the bursting behavior, very long inter-event times such as $\tau \gg \langle\tau\rangle$ may occur, meaning that some nodes or links can be active or inactive for extended intervals of time.

To understand the impact of the β exponent in our analysis, it is important to compare inter-event time distributions with the same minimum τ_0 and average inter-event time $\langle\tau\rangle$. To accomplish this, we considered a distribution with tuning parameters, given by $\psi(\tau) = A(\tau + a)^{-\beta}$, with a normalization constant that can be found by computing

$$\int_{\tau_0}^{\infty} A(\tau + a)^{-\beta} d\tau = 1 \ . \tag{5.9}$$

It follows that

$$\psi(\tau) = (\beta - 1)(\tau_0 + a)^{\beta-1}(\tau + a)^{-\beta}, \quad \tau > \tau_0. \tag{5.10}$$

As for the Poisson process, the average inter-event time can be computed using Eq. (5.8)

$$\langle\tau\rangle = \frac{a + \tau_0(\beta - 1)}{\beta - 2}. \tag{5.11}$$

Therefore, in this equation, a is a parameter that allows us to vary β, keeping the average and the minimal inter-event times fixed.

The following results are based on the above-mentioned methodology, which consists of starting with a static backbone network for the acquaintances of each node and introducing a temporal aspect to the interactions by intermittently activating and inactivating the nodes or links. This is achieved by considering state-change events as a renewal process. The inter-event time distribution considered is given by Eq. (5.10), which captures the heterogeneity in contact interactions and constitutes the primary motivation for this work. The details on the implementation of intermittency in static backbone networks are discussed in Appendix E.

5.2 Exploring the inter-event time distribution in node-intermittent homogeneous networks

Considering the network topology in which a dynamic process takes place is fundamental. For example, as discussed in Chapter III, some structures in the original network have a crucial impact on the spreading of the epidemic. However, in this first analysis, we do not consider the heterogeneity of degrees in the backbone network, to consider only the relevant temporal aspects of the intermittency. Thus, it is possible to investigate the effects of the inter-event time distribution without worrying about structure, which will be considered in the sequence of the chapter.

We run the SIS model on node-intermittent RRNs of size $N = 10^5$ for different inter-event time distributions and compare them to the static case. Fig. 5.4 shows the susceptibility as a function of the infection rate for four values of average inter-event times. For each of them, we vary the exponent β from 2.3 to 3.8. Two main observations can be made. The first is that as $\langle\tau\rangle$ increases, the epidemic threshold decreases and approaches the corrected static value $\lambda^* = 2\lambda$. This corrected value is because we make a rescale in the epidemic threshold for the static networks. In the following, we clarify what this rescaled static network means, since this term will appear throughout the remainder of the text. The intermittency in both nodes and links follows the same distribution for activation and inactivation times. The event only changes the current state. Since spreading simulations start in a stationary regime for node or link activation/deactivation

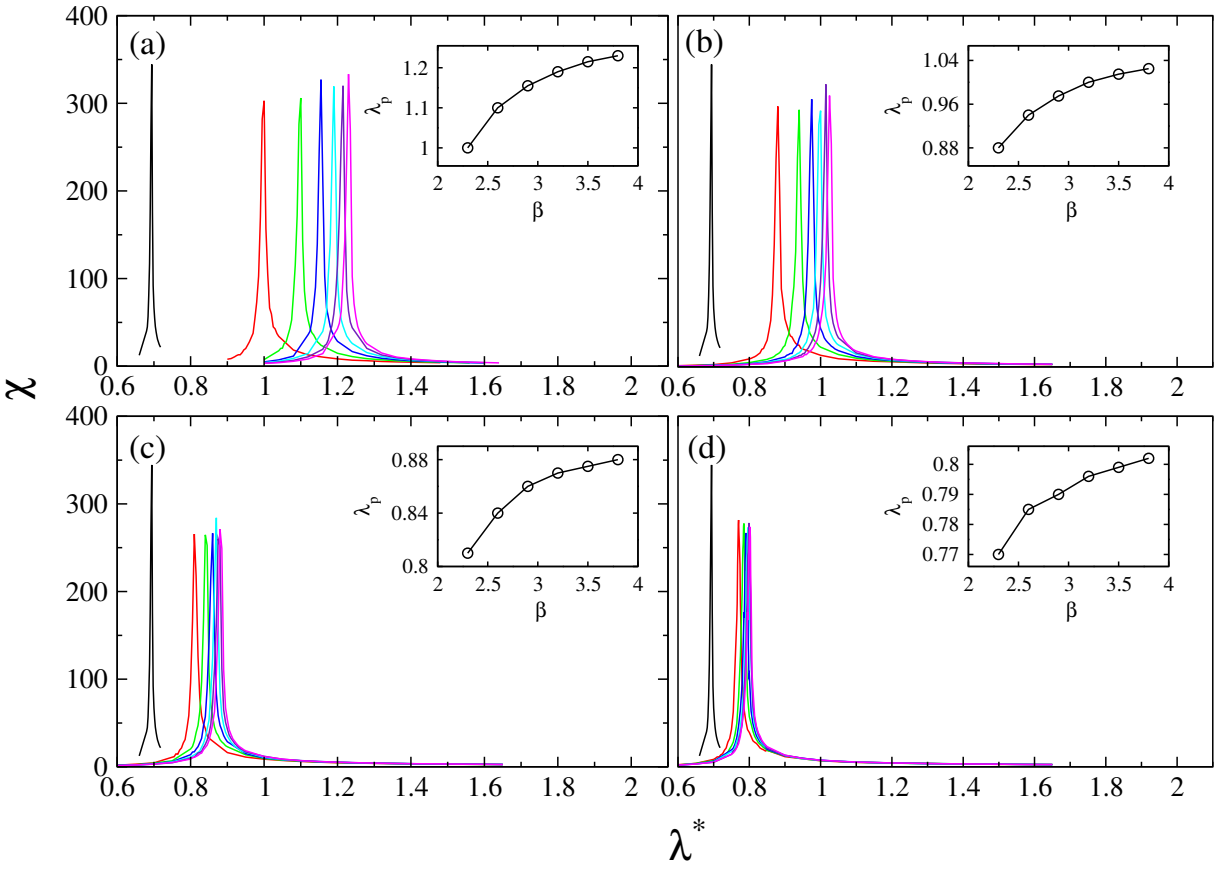

Figure 5.4 – Susceptibility as a function of infection rate for SIS model in RRN of size $N = 10^5$ and degree $m = 3$. Panels (a) - (d) refer to four values of average inter-event times: 0.5, 2, 6, and 15. The colors represent the different exponents of inter-event time distribution as in Eq.(5.10). The exponent β is incremented by 0.3 from 2.3 (red curves) to 3.8 (magenta). The insets present the epidemic threshold corresponding to the susceptibility peak as a function of β. All curves use $\tau_0 = 0.05$. The black curve corresponds to the static network rescaled by $\lambda^* = 2\lambda$.

dynamics, and the inter-event times are distributed with the same rates for both states, on average, nodes are half of the time active and half inactive. A network in which the nodes are inactive for half of the simulation time corresponds to a static network with half the infectivity and, thus, a doubled epidemic threshold. Therefore, when comparing the thresholds of the NI and static networks, it is suitable to compare with $\lambda^* = 2\lambda$.

The second observation is that the influence of the β exponent on the epidemic threshold is stronger when $\langle\tau\rangle$ is smaller, and the curves for different β vary less from each other for large average inter-event times. This possibly occurs because, for large $\langle\tau\rangle$, the nodes remain active for much longer periods, resembling the static case. Surely, the nodes also spend more time inactive, since the same distribution is used for activation and

inactivation. Thus, on average, the time a node is active or inactive is split half-and-half. However, only the active states are relevant for infections in the SIS dynamics. To better visualize this approximation of the intermittent curves to the static one, we compute the difference between the epidemic threshold (susceptibility peak) for the intermittent networks ($\lambda_{P_{NI}}$) and the rescaled static network (λ_P^*). This difference approaches zero as $\langle\tau\rangle$ increases, for the two limiting cases of inter-event time distributions considered in this work: $\beta = 2.3$ and $\beta = 3.8$, as shown in Fig. 5.5.

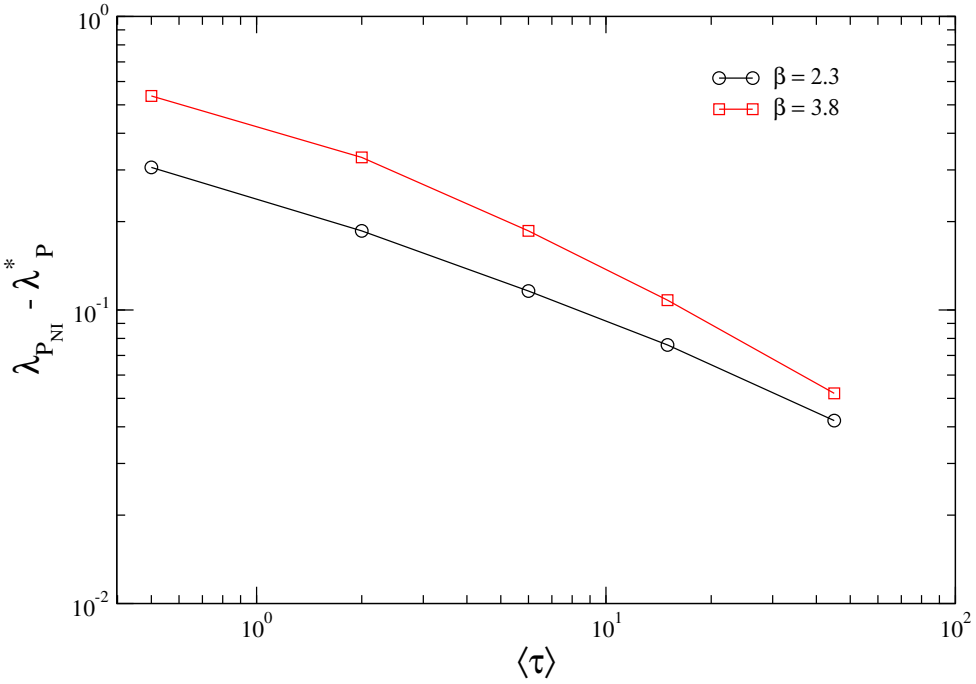

Figure 5.5 – Approaching of the epidemic threshold to the corrected static value as $\langle\tau\rangle$ increases for the SIS model on RRN networks with $N = 10^5$ and degree $m = 3$. $\lambda_{P_{NI}}$ is the value of the infection rate for the peak of the susceptibility for the node intermittent networks, and λ_P^* is the same quantity but for the rescaled static curve. The peak values were taken from the curves of Fig. 5.4.

This analysis allows us to make some remarks on how inter-event time distributions affect epidemics. The epidemic threshold increases if the inter-event time is low, suggesting that short average periods of complete isolation can help mitigate the spread. This occurs because when a node is infected and quickly inactivated, it will not be able to spread the infection. Also, less heterogeneous distributions ($\beta = 3.8$) have a stronger effect in increasing the epidemic threshold, because fewer long periods of activity occur in this kind of distribution.

5.3 Node-intermittent heterogeneous networks

Now, we analyze the effect of node intermittency in power-law degree-distributed networks generated using the UCM model. As discussed in Ch. III, depending on the exponent of the degree distribution, the activation mechanisms of the SIS model are different. Thus, we considered two cases: $\gamma = 2.25$, with activation triggered by the maximum k-core, and $\gamma = 3.5$, in which the outliers possibly present in the networks cause multiple transitions, as discussed in Sec. 4.3. For node intermittency, we present simulations for inter-event time distributions with exponent $\beta = 3.7$ and $\langle\tau\rangle = 0.5$, because this combination led to the highest epidemic threshold among the values we investigated[2]. Thus, for an finite-size scaling analysis, we simulate the SIS model in both static and node-intermittent networks of sizes varying from 10^3 to 10^7, as shown in Fig. 5.6. Both networks use the cutoff degree $k_c = 2\sqrt{N}$, and all static networks' curves are rescaled by $\lambda^* = 2\lambda$.

It is worth mentioning that the network structure is the same, meaning that it was generated from the same degree distribution, and the same links were used, both for the intermittent and static cases. This is especially important in the $\gamma = 3.5$ case, since in these networks, fluctuations sometimes lead or not the occurrence of outliers and, consequently, of multiple transitions. Thus, we chose a network sample in which the multiple transitions take place to verify the effect of intermittency.

Node intermittency has little effect in UCM networks with $\gamma = 2.25$. As panel (a) of Fig. 5.6 shows, there is an increase in the epidemic threshold due to intermittency for all investigated sizes. However, the scaling of the threshold as a function of size, shown in the inset, is the same for static and intermittent networks, both vanishing with the same scaling law. An interesting behavior occurs for intermittency in UCM networks with $\gamma = 3.5$. In this case, the multiple transitions characteristic of static structures with $N > 10^6$ are suppressed by the intermittency, and the susceptibility curves show only clean transitions characterized by a single sharp peak.

An explanation for this is proposed in Fig. 5.7, in which the curves for the epidemic lifespan of a node-intermittent star graph start to separate from the static case for $k_{\text{hub}} > 10^3$. Since the hubs in the UCM networks have a degree comparable to the degree cutoff

[2] Combinations of $\beta = 2.5$, $\langle\tau\rangle = 2$ are shown in Sec. 5.4

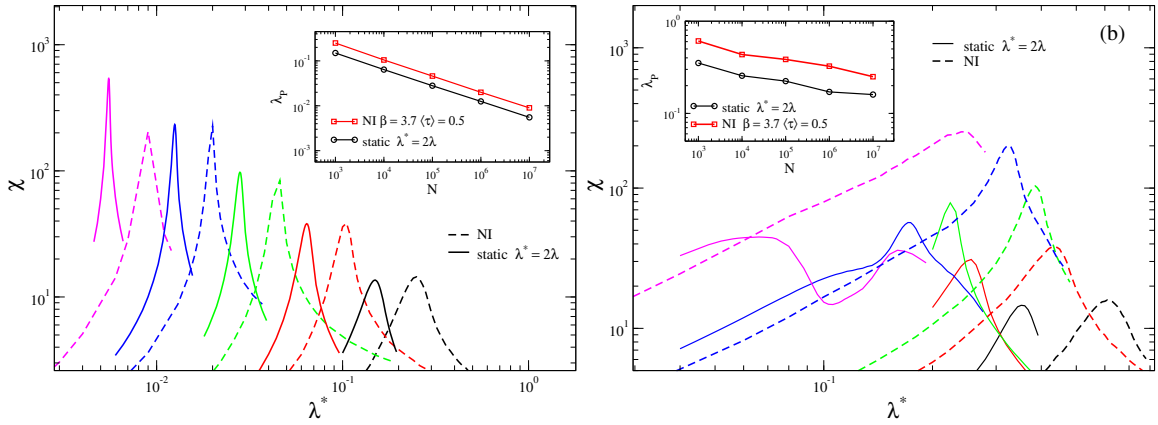

Figure 5.6 – Susceptibility as a function of rescaled infection rate $\lambda^* = 2\lambda$ of the SIS model in both static (solid line) and node intermittent (dashed line) UCM network with exponent (a) $\gamma = 2.25$ and (b) $\gamma = 3.5$. The network sizes increase from 10^3 (black) to 10^7 (magenta). The insets show the infection rate for the peak of the susceptibility as a function of the network size for both static and intermittent cases. All intermittent networks were generated using $\beta = 3.7$ and $\langle\tau\rangle = 0.5$.

$k_c = 2\sqrt{N}$, this means that for network sizes from $N = 10^6$, the activity lifespan of the hubs can be much lower than expected in static cases. For networks with $\gamma < 2.5$, intermittency does not affect the dynamics much since the hubs are embedded in densely connected structures - the maximum k-core. As discussed in Sec. 3.2.4 of Ch. III, for these networks the epidemic is sustained by the maximum k-core. However, for $\gamma > 2.5$, the isolated hubs play an essential role in the epidemic activation mechanism. As also discussed in Sec. 3.2.4, the time for the infection starting from a given source hub to get to another hub (target) is much greater than the time the infection lasts in the hub and its vicinity. This infection time can be severely changed if we consider node intermittency. Periods of intermittent inactivation can make a significant difference in the phase transition in the SIS model.

5.4 Link vs. node intermittency

So far, we have investigated only the case in which nodes follow a dynamic process of intermittent activity. However, as mentioned at the beginning of this chapter, many similar studies have considered the links to be intermittent. In this section, we aim to elaborate on how node intermittency can be more relevant for containing the spread than merely inactivating the links.

Let us consider the epidemic lifespan discussed in Ch. III, which is an important measure for epidemic spreading models, related to the time an infection lasts in a star graph. Fig. 5.7 compares link and node intermittency in star graphs and their static counterparts. In all intermittent cases, an infection rate of $\lambda = 0.1$ was used, and the curves were averaged over 10^5 realizations. For both low (a) and high (b) values of $\langle\tau\rangle$, link intermittency behaves similarly, being insensitive to different β exponents. These curves also follow the same exponential behavior expected for static networks. The link intermittency curves lie between those of the static star graphs (in magenta and brown). However, rescaling the static curve with $\lambda = 0.1$ by $k^*_{\rm hub} = 2k_{\rm hub}$ causes it to collapse onto the link intermittent curves, indicating that the change in epidemic lifespan promoted by link intermittency is trivial, as the next results will reinforce.

The scenario changes with node intermittency. The curves initially agree with the static case with $\lambda = 0.05$ (magenta curve) but begin to deviate for $k_{\rm hub} > 10^3$. For average inter-event times comparable to the infectious period $\mu^{-1} = 1$, the lifespan grows following a power-law. In contrast, for $\langle\tau\rangle \gg \mu^{-1}$, the lifespan appears to saturate.

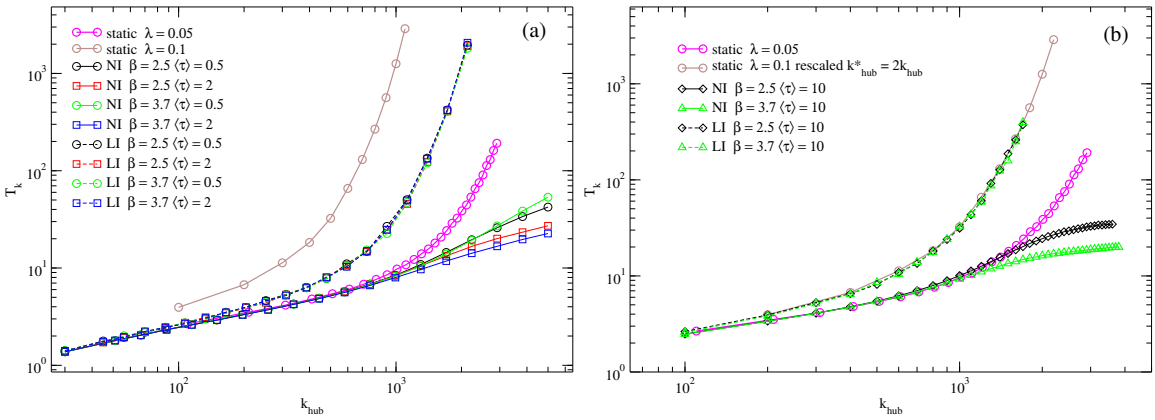

Figure 5.7 – Activity lifespan for SIS model in star graphs as a function of its number of leaves ($k_{\rm hub}$). Static curves are shown using two different infection rates. All intermittent cases use $\lambda = 0.1$. Panel (a) shows the intermittent cases for $\langle\tau\rangle$ comparable to the infectious period $\mu^{-1} = 1$. Panel (b) uses $\langle\tau\rangle \gg \mu^{-1}$.

In Fig. 5.8, we show the comparison between node/link intermittency and the static cases, in which we considered both all links and only half of the links active. This figure presents the analysis for both models: SIS (a) and SIR (b). We show that link intermittency corresponds to the static case with half of the links active, meaning that temporal heterogeneity plays no role in increasing the epidemic threshold. This also implies that intermittently reducing contacts as a strategy for controlling the spread is as

effective as removing half of the links from the original contact network.

On the other hand, our results show that keeping a node isolated from all its neighbors, even for short periods, can be significantly more effective in controlling the spread, since the epidemic threshold is increased. Also, this increase is not trivial. By trivial, we mean that, as there is no preferred state in the intermittency, the nodes stay active and inactive for equal times on average, so the expected epidemic threshold would be twice the static case. However, for node intermittency, the observed epidemic threshold is greater than simply reducing the infection rate proportionally. Furthermore, considering a combination of two values of β and $\langle\tau\rangle$, we observe that, for node intermittency, the epidemic threshold is greater for shorter inter-event times and less heterogeneous inter-event time distributions. For link intermittency, there is no effect of these parameters on the SIS dynamics, in agreement with Fig. 5.7.

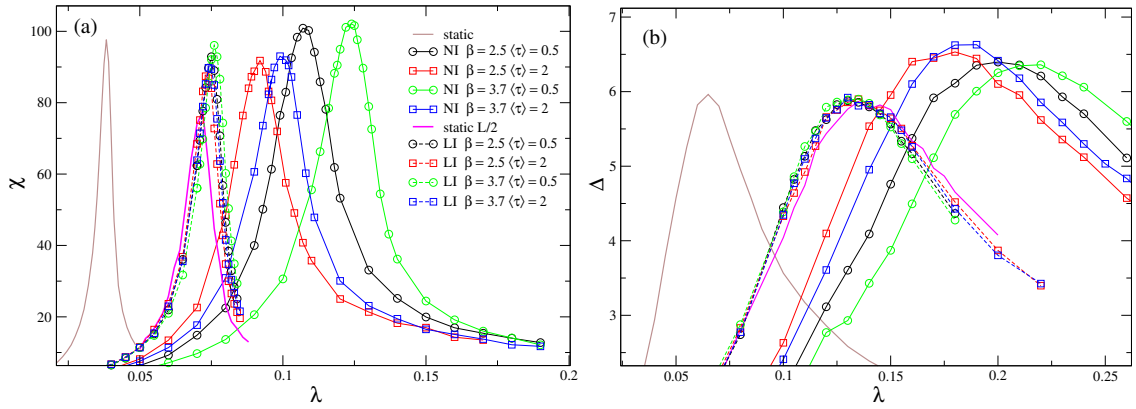

Figure 5.8 – Susceptibility (a) and variability (b) as a function of infection rate for static and intermittent networks using SIS and SIR models, respectively. The original network is a UCM with exponent $\gamma = 2.75$ of size $N = 10^5$ nodes for panel (a) and $N = 10^4$ for panel (b). Colors in panel (a) have the same label as panel (a).

This is a theoretical work, and further analyses are needed. However, the analyses developed in the last sections offer interesting insights. First, the epidemic threshold increases when less heterogeneous distributions are considered, meaning that the long inter-event times found in scale-free inter-event time distributions can be problematic for containing the spread. The epidemic threshold also increases when the average inter-event time decreases, since, on average, there is less time for infections to occur. Of course, nodes or links also spend less time inactive, but only the active state affects the SIS dynamics. Furthermore, heterogeneity itself plays a role in spreading: extreme periods of activity during which an agent can transmit the pathogen, followed by many

short periods of intermittent activity, have a much greater impact than an agent infecting repeatedly but only at intermediate time intervals. Another takeaway is the importance of node inactivation for reducing the spread. Link intermittency resembles the reduction of contacts experienced during the last pandemic. However, our results suggest that a more effective strategy is the complete isolation of a node (e.g., through the use of well-adjusted masks) for some - not too heterogeneous - time intervals.

5.5 SIS criticality on intermittent lattices

As our final analysis of the effect of intermittency on dynamic processes in networks, we once again consider a homogeneous structure: lattices. The motivation for this choice is to investigate whether intermittency alters the phase transition of the Contact Process in lattices, discussed in Chapter III. One possible approach to studying phase transitions is computing the critical exponents through simulations.

Section 3.2.1 discussed the Contact Process, which belongs to the directed percolation universality class and whose solution and analysis can be approached using the mean-field approximation. However, if the system has a dimension $d < d_c$, as in a square lattice ($d = 2$), the critical behavior is strongly modified by fluctuations and correlation effects, making it necessary to apply approximated methods for its study [2].

The computation of critical exponents using homogeneous initial state and seed simulations was discussed in Sec. 3.2.4. The same analysis will be applied to the node intermittent lattices. To investigate the role of temporal heterogeneity, we consider two different inter-event time distributions. In all cases, the lattice size used is $L = 500$, the minimal inter-event time is $\tau_0 = 1$, and the average inter-event time is $\langle\tau\rangle = 5$. Before proceeding with the critical exponents simulations, we must estimate the approximated value of the epidemic threshold. Thus, we compute the average quasi-stationary prevalence and the susceptibility, both as a function of infection rate, as shown in Fig. 5.9. As observed in the network analysis, the less heterogeneous distribution computed using $\beta = 3.5$ gives the higher epidemic threshold. Also, both distributions shift the threshold in comparison to the rescaled static case.

For the homogeneous initial state simulation, we used two different sizes of lattice, $L = 200$ and $L = 500$, which is useful to analyze the finite size effects. It is possible to observe in Fig. 5.10 that indeed $L = 200$ deviates from the $L = 500$ curves for the

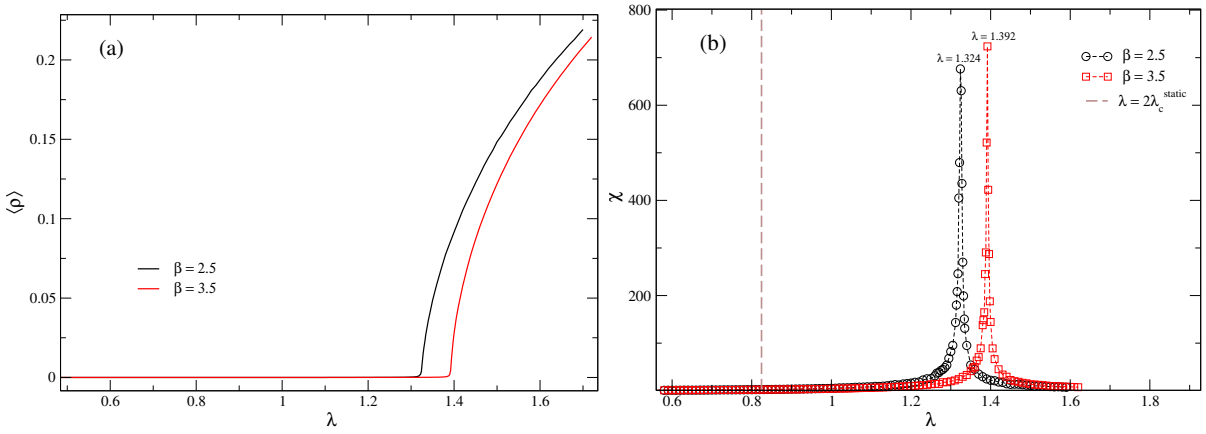

Figure 5.9 – Average quasi-stationary prevalence (a) and susceptibility (b) as a function of infection rate for SIS on two NI lattices of $L = 500$. The inter-event time distributions were computed for two different exponents, both using $\tau_0 = 1$ and $\langle\tau\rangle = 5$.

simulation time we use. The curves corresponding to the critical infection rate would deviate less from each other if the epidemic threshold were not size-dependent. However, to ensure that finite-size effects are not interfering with the analysis in this figure, larger sizes would be used. So, we can not affirm that the size $L = 500$ is the most appropriate for analyzing the decay of ρ to identify precisely the epidemic threshold. Still, the figure gives a picture of the behavior of this quantity. Also in Fig. 5.10, panel (a) corresponds to $\beta = 2.5$ and (b) to $\beta = 3.5$, and only through visual inspection is it not possible to distinguish between the curves to point out exactly which one is following a power law behavior, characteristic of the critical curve.

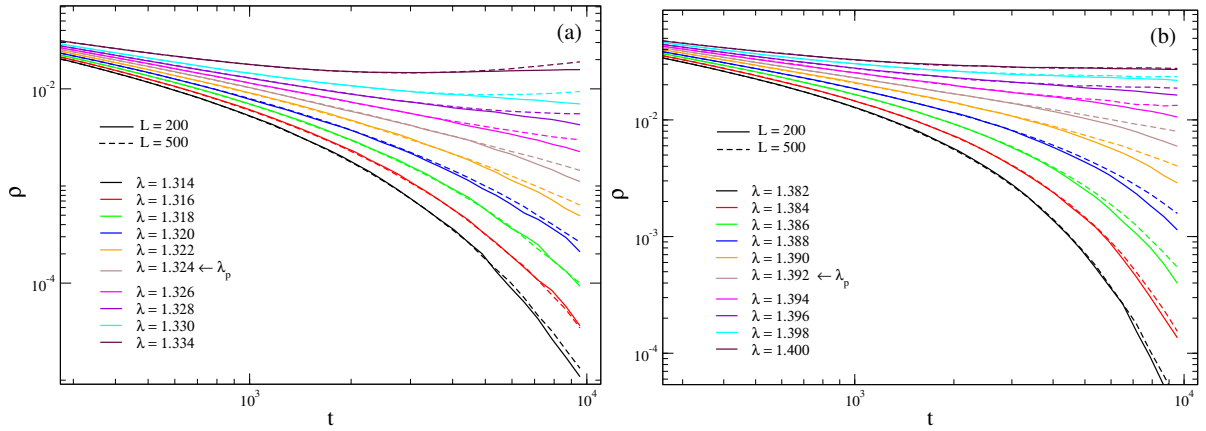

Figure 5.10 – Homogeneous initial state simulations for lattices of different sizes. The inter-event time distributions we computed using $\beta = 2.5$ in (a) and $\beta = 3.5$ in (b). In both cases $\tau_0 = 1$ and $\langle\tau\rangle = 5$. All the curves are averages over 10^4 samples.

If we turn to the seed simulations, the quantities are plotted in Fig. 5.11 for a NI lattice of size $L = 500$. The top panels refer to inter-event time distributions using $\beta = 2.5$ and the bottom one using $\beta = 3.5$. One direct observation is that bottom panels resemble the analysis performed in static lattices as in Fig. 3.15. As the values of the infection rate are the same as in Fig. 5.10, it is possible to note that the curve (the brown one) is the one corresponding to the value pointed by the susceptibility in Fig. 5.9; this is especially clear in the number of active sites in Fig. 5.11(f). However, this conclusion does not hold for the top panels of Fig. 5.11, where no curve exhibits a clear power law behavior in the number of active sites, which can be seen in panel (c).

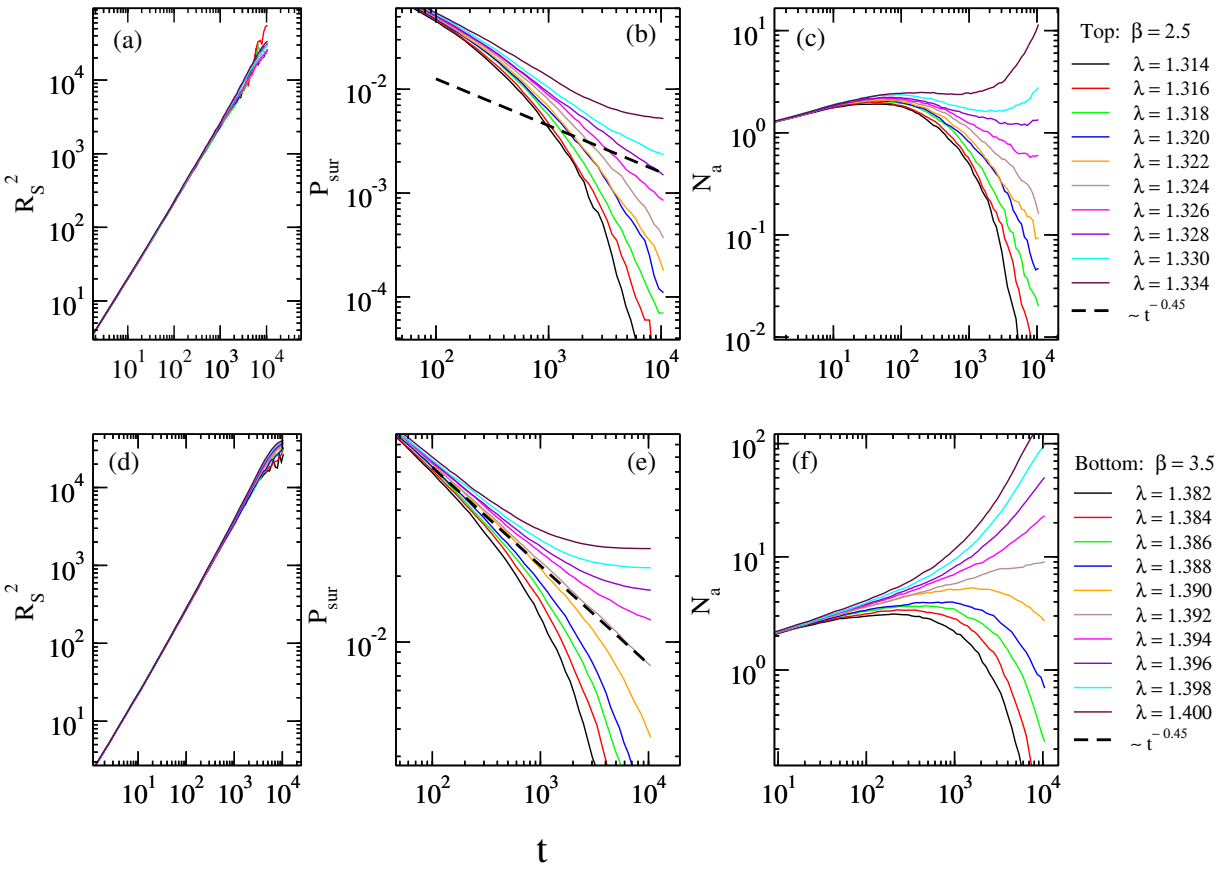

Figure 5.11 – Seed simulation for a NI lattice of size $L = 500$. The inter-event time distributions were computed using $\beta = 2.5$ in the top panels and $\beta = 3.5$ in the bottom panels. In both cases $\tau_0 = 1$ and $\langle\tau\rangle = 5$. All the curves are averages over 10^5 samples.

Therefore, the case of intermittent lattices with $\beta = 3.5$ appears to be comparable to the SIS model on static lattices, as the critical behavior shown in the bottom panels of Fig. 5.11 is very similar to that discussed in Sec. 3.2.4, within the context of the DP universality class. However, the case of highly heterogeneous inter-event time distributions,

characterized by $\beta = 2.5$, remains unclear. The top panels of Fig. 5.11 reveal a modification of the DP critical behavior. One possible explanation for this is the occurrence of temporal Griffiths phases (TGP). The Griffiths phase (GP) has already been discussed in Ch. III, where it arises from spatial rare regions, leading to extended critical regions in the parameter space of the phase transition. The temporal counterpart, TGP, reverses the roles of space and time: in GP, spatial disorder leads to generic scaling as a function of time, while in TGP, temporal disorder leads to generic scaling as a function of system size [40]. Reference [151] investigates the possibility of TGP in the contact process (CP) with temporal disorder introduced through time-dependent infection and healing rates. One of the analyses presented is the computation of the survival probability as a function of time, $P_{\text{sur}}(t)$, where the authors show that, for different values of the control parameter, no curve follows the power law expected at criticality.

A similar analysis can be carried out for intermittent networks. For the $\beta = 3.5$ case, the black dashed line in Fig. 5.11(e) matches the expected critical behavior, decaying with an exponent $\alpha = 0.45$, which is typical of the DP universality class [2]. In contrast, for $\beta = 2.5$, the same decay does not appear to match any of the analyzed curves (see Fig. 5.11(b)), suggesting that the critical exponent may change in this case. It is worth emphasizing that a more quantitative analysis is needed, such as the computation of the local slope of all curves with proper statistical treatment. Still, we may hypothesize that the intermittency induced by highly heterogeneous inter-event time distributions is a strong candidate for introducing temporal disorder into the system, which would explain the modified critical behavior as a manifestation of TGP.

5.6 Concluding remarks

In this chapter, we presented an analysis of spreading processes in intermittent networks, in which the temporal aspect of interactions was considered. We found that link intermittency is equivalent to a trivial reduction of contacts in static networks, while node intermittency exhibits a much richer behavior, both in practical and theoretical terms. Sections 5.2 to 5.4 comprise the first part of this work, which is being prepared for submission as an article. We expect to submit it for publication soon. Section 5.5 constitutes the second part and will be treated separately, as further analyses are needed.

VI Critical behavior of the brain

Related publication:

J. T. Moraes *et al*, *Self-tuned criticality: Controlling a neuron near its bifurcation point via temporal correlations*, Phys. Rev. E 107, 034204, 2023. [51]

Our behavior, feelings, and thoughts can be seen as emergent properties of our intricate biological hardware: the brain. Over the years, scientists have dedicated much effort to unraveling the mysteries behind this system. Physics initially contributed a mechanistic view of the world to this task. However, as more information became available, a reductionist approach proved insufficient. The brain needed to be viewed as a complex system. Given that the brain is a complex system, is it ordered or chaotic? On one hand, the brain needs to maintain some level of order to ensure proper functioning in response to stimuli. On the other hand, it requires some degree of disorder to adapt to environmental changes, i.e., it should have flexibility. The likely outcome is that the brain is balanced between these two opposing states, or in statistical mechanics terms, it should operate at criticality [152].

Evidence supporting the criticality of the brain is extensive, with new findings continually reinforcing the hypothesis. These are pieces of a larger puzzle: how does this happen? The most accepted idea is that the brain self-organizes to criticality over many years of evolution through adaptation mechanisms [52]. Criticality is strongly related to optimal functioning [48] and performance in the brain via information transfer [42]. Thus, the brain may have evolved to be poised at a critical point. Or could it instead operate within a critical region [111]?

The human brain consists of about 100 billion neurons connected by around 100 trillion synapses [49]. These connections are organized at many scales of space and time, with different functions. Although the nervous system has been studied for decades, many questions remain. The emergence of consciousness and the challenges in treating and preventing dementia are among these open topics. Alzheimer's disease (AD) is a type of dementia that affects behavior, memory, and thinking, and sometimes severely

impacts daily tasks [153]. In 2006, there were 26.6 million cases of Alzheimer's disease worldwide, and this number could increase fourfold in the coming decades [154]. While AD has treatments, there is still no cure. This is just one of the many challenges in neuroscience, making a deeper understanding of the brain an urgent research area.

Thinking of the building components of the brain, a network structure can be perceived. Neurons are connected through synapses, forming an intricate anatomical web. Although we cannot yet access the entire real network, advances in mapping brain connections have increased [155]. In addition, much information can be extracted from the fully mapped brains of animals such as the *C. elegans* [156] and, more recently, the adult fruit fly [157]. Thus, network science has become a valuable tool in organizing the pieces of the puzzle of the critical brain. Moreover, understanding the operation and functioning of the brain is an important step towards more effective therapeutic approaches for neurological and brain diseases [75].

Although the idea that the neuronal elements of the brain form a network has been known since the nineteenth century, the ability to map the actual structure is relatively recent. The study of brain structure changed dramatically with the advent of connectomics, a field driven by advances in methods for measuring and visualizing brain organization [158]. The term "connectome" refers to the brain's cellular wiring diagram, defining a matrix that contains the pairwise anatomical connections between neural elements of the brain [75]. Also, it is important to consider functional networks, which map the brain's network structure by measuring the correlation between the activity of neuronal units [159].

This chapter is dedicated to shedding light on some of these topics. In the 2022 first semester, I did a research internship in *Universidad Nacional de San Martín* - Argentina, in the Center for Complex Systems and Brain Sciences (CEMSC^3)[1]. Part of the research conducted there, investigating individual neuron low-dimensional models, was published in 2023 [51]. This work showed how it is possible to implement a control strategy, already discussed in the context of high-dimensional models, to low-dimensional approaches, for instance, using maps to model the neurons. The results of this work will also be treated in the present chapter.

[1] CEMSC^3 stands for *Centro de Estudios Multidisciplinarios en Sistemas Complejos y Ciencias del Cerebro.*

6.1 Paths to criticality in the brain

The ability to monitor the activity of thousands of nerve cells or observe the average activity in a large fraction of the whole brain has brought a decisive change in neuroscience. The century-old approach of mapping individual neurons, while still relevant and successful in precisely describing neuronal behavior, is giving place to a more collective view of interacting neurons. Thus, statistical physics approaches have become increasingly necessary for understanding the brain [83]. The construction of statistical models for biological systems, such as the brain, directly from real data sets has been a successful approach. The remarkable outcome is that these generated models seem to be poised at a critical regime [160].

A breakthrough evidence for critical behavior in the brain came in 2003 with the experiments of Beggs and Plenz on neuronal avalanches [42]. In this study, they observed that spontaneous activity in cortical networks is consistent with a branching process [161]. This behavior was already known for different systems, such as earthquakes and forest fires, where if one unit in the system exceeds a threshold, it causes other units to do the same, and the cascade of events propagates through the entire system, these cascades are also called avalanches. Beggs and Plenz observed avalanches of activity, both in size and lifetime, using cortical networks *in vitro*, and these avalanches followed a power-law distribution, suggesting that the system operates near a critical point [43]. In 2009, an *in vivo* study showed a similar pattern for avalanches of spontaneous activity using microelectrodes in the cerebral cortex of two awake monkeys [44]. This result was consistent across different cortical areas, reinforcing the evidence that power-law behavior is not limited to reduced systems but is also observable in various regions of the brain. Another *in vivo* study recorded action potential avalanches from the cerebral cortex and hippocampus of rats, finding that the brain operates near a temporally complex regime, which collapses during anesthesia [45].

In 2010, Chialvo pointed out that the power-law patterns observed in neuronal avalanches, along with other results of emergent complex neural dynamics, could not be well explained without criticality concepts [50]. However, brains should share fundamental laws of nature that could be better understood by analyzing larger spatiotemporal brain data [50]. In this context, using large-scale brain hybrid modeling, Haimovici *et al.* showed that brain structure can support the dynamics observed in fMRI recordings only

at criticality [48]. Despite the simplicity, when confronted with real fMRI, this model was able to show that the brain at the resting state (i.e., not performing any task) is a system poised at criticality [48]. This was accomplished through hybrid modeling, in which the authors implemented the model using the Hagmann connectome [155] as a network substrate.

Therefore, the brain criticality hypothesis is supported by the aforementioned examples, among others [46, 47, 41]. It states that only operating at the edge of chaos, biological systems could perform complex computations necessary for survival. The ability of a system to be robust against changes in the environment and to adapt to the same changes seems to be mutually exclusive, but living systems are perceived as adaptive and robust at the same time. Back to the classical theory of dynamical systems, given two close initial conditions, the maximum Lyapunov exponent measures how fast the solutions diverge in time [58] as

$$|\delta X(t)| \sim e^{\lambda t}|\delta X(0)| \ , \tag{6.1}$$

in which $|\delta X(t)|$ is the distance between the trajectories at time t, $|\delta X(0)|$ is the distance between the initial conditions, and the exponential rate of divergence λ is the Lyapunov exponent. A positive maximum Lyapunov exponent may be taken as an indicator that the system is chaotic. But, what if the Lyapunov exponent is zero? In this case, the system is said to be quasi-periodic or at the edge of chaos. If the system has $\lambda \approx 0$, the system can be easily driven from a stable and periodic state to a chaotic phase. For the chaotic phase, under strong perturbations, the system rapidly explores large regions of phase space. By sampling extended volumes of phase space, the system increases its chances of discovering new solutions compatible with the altered environment, allowing it to adapt.

Therefore, at the edge of chaos, systems can balance between two extreme phases: active (chaotic) and quiescent (ordered). Critical dynamics offer a precise balance between these two unfavorable tendencies, and for the brain, it enables effective information processing [43], also maximization of memory [162] and sensitivity to stimuli [163]. Still, given that living systems are poised on the edge of chaos, how did evolution select to operate in this state? This is an intriguing question and the explanations of the mechanisms that lead to criticality are a vast field of research. In this context, two important paths to criticality will be discussed ahead.

Self-organized Criticality

Let us first consider a simple model: the sand pile model presented in 1987 by P. Bak and collaborators [164]. Imagine grains of sand being deposited on a flat surface. As the grains form a pile, its slope will increase until it reaches a critical value at which avalanches of sand will start to happen. Once the slope of the pile decreases, more sand can be deposited until the critical slope is reached again, and so on. This process makes the sand pile self-organize towards a critical slope [58]. This model was considered to contain the essence of Self-Organized Criticality (SOC) [52], which is strongly related to the explanation of the critical behavior of the brain. However, it is important to emphasize that, over the years, the scaling behavior and other critical aspects of the sand pile model could never be fully determined [165].

Still, the idea of SOC being one of the possible explanations for criticality in the brain remains relevant [166]. P. Bak, in [52], presented an interesting argument about why the brain should be critical: if it is exposed to an external signal, such as an image, this signal serves as an input and must be able to access any necessary information to process it. Thus, the brain could not be subcritical, where only a limited amount of information would be accessed. It could not be supercritical either, since in that case, any input would lead to explosive branching processes, connecting all information at once. Therefore, the brain must operate in a critical state, where information propagates only as necessary. This is related to the way we learn. Adaptive learning models have emphasized the possibility of the brain choosing the strongest synapses and depressing the inadequate ones, leading to a permanent counterbalancing that may seem analogous to a critical state [167] so that criticality arises inherently from the dynamics of synaptic activity through self-organization [168].

There are still open questions about the generality and capacity of SOC to explain certain critical features [169, 165]. Yet, strategies in optimization [170] and control of complex systems [166] are research topics of current interest that are based in SOC. This last example will be better discussed in section 6.3.

Extended critical regions

Research using data on brain blood oxygenation level-dependent (BOLD) signals found evidence of a phase transition [47]. The authors considered the normalized size of

the largest active cluster, i.e., the largest connected group of voxels with BOLD signals above the threshold, as the order parameter and the number of active sites as the control parameter. A sharp increase in the order parameter and increased variability were observed for a given control parameter, indicating a second-order phase transition. However, through further analysis, the authors found that the control parameter tends to remain near the critical values rather than settling at a single point. This raises the question: what if, instead of an exact critical point, there is an extended critical region?

Using an integrate-and-fire neural network model, researchers showed how hierarchical modular networks (HMNs) affect SOC [171]. Brain networks are known to exhibit modularity, making the study of these networks particularly relevant [75, 110]. The authors found that in modular networks, the critical region was extended, making SOC more robust to variations in model parameters.

Another analysis in this direction compared activity propagation in HMNs with simulations in both human and *C. elegans* connectomes. The results also point to an extended critical region, and the authors propose the presence of Griffiths phases [111].

The existence of a broad Griffiths phase in brain dynamics allows power-law scaling and enhanced responses to stimuli to persist over a wide range of parameters. It is worth noting that the idea of brain criticality via Griffiths phases adds another piece to the puzzle rather than replacing SOC. In fact, a theory for self-organization into a wide region separating order from chaos emerges as a new paradigm [111].

6.2 An individual neuron model

Although large-scale modeling is relevant and realistic, a much simpler approach can be employed to capture neuro-like behavior in its essence, for instance, using maps. While differential equations describe the system's evolution in continuous time, difference equations, also called maps, use discrete time steps and can be very useful for analyzing chaotic and periodic solutions in complex systems [99].

When modeling the brain, a starting point should be to reproduce, at least minimally well, the functioning of neurons and how they communicate with each other. The basic operation of neurons involves the generation of an action potential, which is transformed into a chemical message. When this message crosses the gap between two neurons, they communicate through synapses [172].

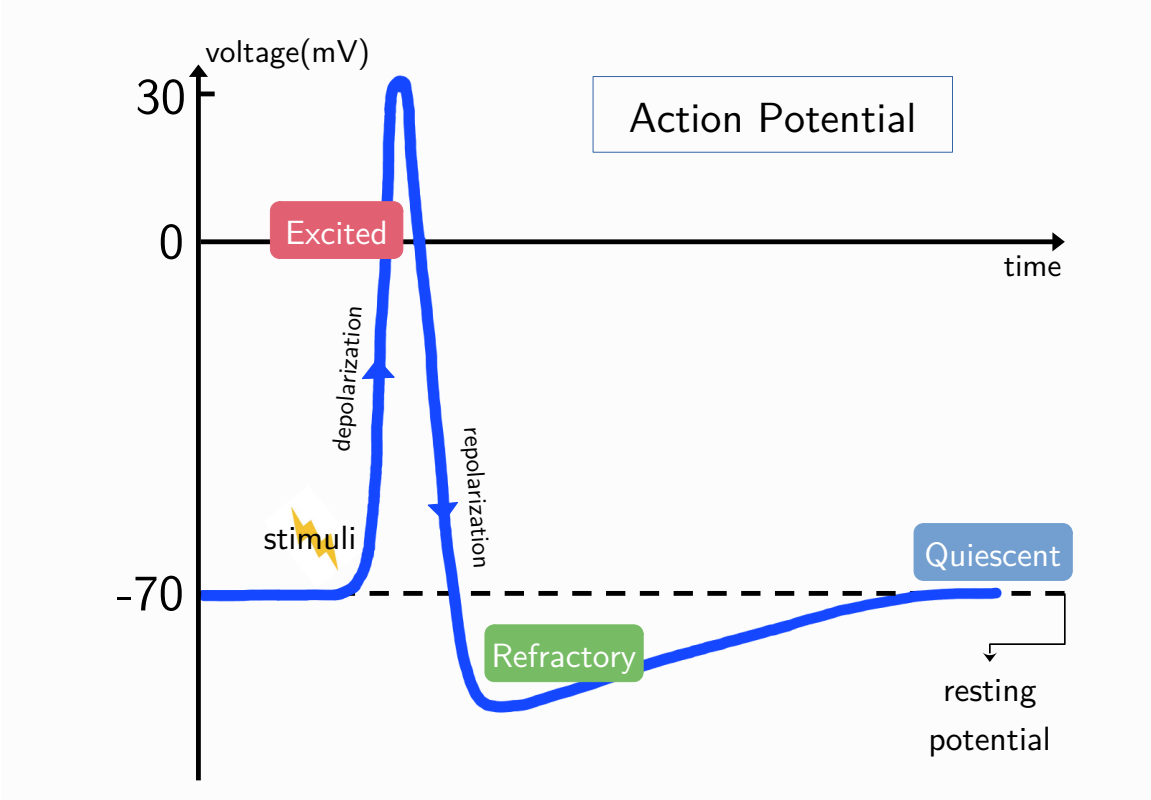

Figure 6.1 – Illustration of action potential in nerve cells' membrane. The neuronal states are dictated according to the voltage values.

The action potential, illustrated in Fig. 6.1, is an electrical signal that travels through the neuron and determines its state. If the voltage is around $-70,\text{mV}$, the neuron is in the resting (quiescent) state. When it receives stimuli, such as from neighboring neurons, the voltage increases. Once it reaches a threshold value ($-50,\text{mV}$), the neuron begins to depolarize, and the voltage reaches a peak, characterizing the excited state. After firing, the voltage decreases, and the neuron enters a refractory state until the membrane potential is restored to the resting level. During this refractory period, the neuron cannot fire again. This process is driven by calcium and potassium channels in the nerve cell membrane.

One of the attempts to model neuronal activity using maps [173] was proposed by Chialvo in 1995 [174]. In this work, the author considered four global properties that the model should satisfy:

i. The equilibrium point of the system, called the resting state, is reached in the absence of external perturbations and must be a global attractor.

ii. The phase space must have two domains, called subthreshold and suprathreshold. Small perturbations do not alter the stability of the global attractor in the subthreshold domain, while sufficiently large perturbations drive the system to the suprathreshold domain, where the state variables visit larger regions of the parameter space before eventually returning to the resting state.

iii. The system may not respond in the same way for a given period to any external perturbation (refractory period), so the minimum amplitude of a perturbation applied during this period must be a function of time.

iv. With a constant bias input, the system presents two possibilities depending on the parameters used: periodic oscillations or chaotic dynamics.

Accounting for these global properties, it is possible to mimic generic neural kinetics, explained in the context of Fig. 6.1, using two state variables. Thus, the two-dimensional Chialvo map (CM) is given by the following equation

$$\begin{aligned} x_{n+1} &= f(x_n, y_n) = x_n^2 \exp(y_n - x_n) + k \\ y_{n+1} &= g(x_n, y_n) = a y_n - b x_n + c \end{aligned} \tag{6.2}$$

in which x and y are the activation and recovery-like variables, respectively. Three constants are used: $a < 1$ is the time constant of the recovery, $b < 1$ is the activation dependence of the recovery process, and c sets the fixed point of the recovery variable. Parameter k represents an additive perturbation (bias) that will make the system bifurcate from a fixed point to a limit cycle or chaotic bursting, depending on its value. The time evolution of the activation variable is shown in Fig. 6.2 for both the excitable and chaotic regimes.

One of the possible analyses that can be performed for the maps is the computation of the corresponding nullclines, defined as the curves in which $x_{n+1} = x_n$ and $y_{n+1} = y_n$ [99]. For the Chialvo map, the asymptotic behavior of any initial condition will be represented in the phase plane by the vector field defined through the nullclines

$$x_f = x_f^2 \exp(y_f - x_f) + k \qquad \text{and} \qquad y_f = \frac{c - b x_f}{(1 - a)} \, . \tag{6.3}$$

Therefore, this perspective can be used to study single neuronal activity since the model effectively reproduces generic excitable dynamics, including the resting state,

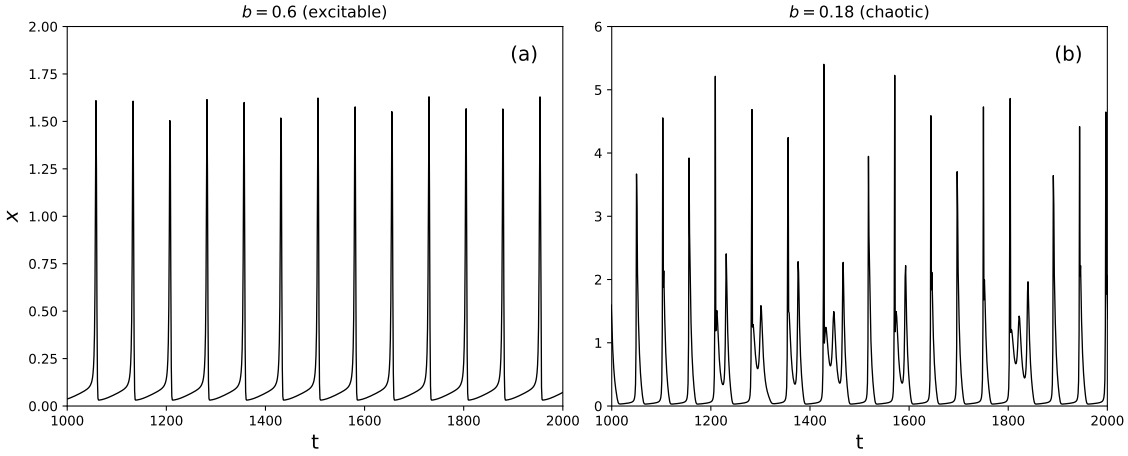

Figure 6.2 – Solution of Eq. (6.2) for the activation variable for a time interval of 10^3 iteration steps. Panel (a) shows the excitable regime using $k = 0.03$ and (b) $k = 0.025$ is used for the chaotic solution. For both panels $a = 0.89$ and $c = 0.28$.

membrane action potential, refractory period, and the periodic or chaotic behavior of the state variables. It is possible to observe the similarity of the pattern exhibited by the action variable in Fig. 6.2(a) for the excitable regime with the illustrated behavior of the action potential in Fig. 6.1.

6.3 Self-tuned criticality: controlling a neuron near its bifurcation point

As discussed above, many real biological systems appear to be poised at criticality [160]. In this regime, the system reaches maximal sensitivity to environmental changes while maintaining internal order, which is advantageous for survival and adaptation. Chialvo *et al* [166] used the first autocorrelation coefficient AC(1) to identify the critical parameter in high-dimensional models. Since perturbations take longer to dissipate near criticality, the critical slowing down is captured by this measurement. AC(1) is the autocorrelation of the order parameter at lag $K = 1$. The autocorrelation function AC, for a time lag K can be defined as $AC(K) = c_K/c_0$ [175], where c_K is

$$c_K = \frac{1}{t_{\text{ser}}} \sum_{t=1}^{t_{\text{ser}}-K} (x_t - \bar{x})(x_{t+K} - \bar{x}), \tag{6.4}$$

with t_{ser} being the the length of the time series $x(t)$.

The hypothesis that real systems can operate near critical points based on SOC is consistent with the existence of an evolutionary feedback mechanism that finds the optimal critical point and keeps the system poised at it [52]. Accordingly, a recent method was proposed to model a control mechanism for complex systems [166]. The AC(1) function was used to tune the system to the vicinity of the critical point for both equilibrium (Ising model) and non-equilibrium models (Vicsek and Greenberg-Hastings).

For low-dimensional models, such as the Chialvo map discussed in the previous section, a phase transition manifests as a bifurcation. Could the control mechanism presented in [166] be suitable for tuning low-dimensional systems to their bifurcation point? In an attempt to answer this question, we presented the following analysis in reference [51].

AC(1) can also be employed for maps if a small additive Gaussian noise (with variance $\sigma \sim 10^{-6}$) is added to the activation variable in Eq. (6.2). This allows us to estimate the typical slowing down: if the system is far from the bifurcation point, perturbations decay rapidly, resulting in a relatively low AC value. On the other hand, as the system moves into an unstable regime, the typical critical slowing down of perturbations occurs, and the AC increases. Fig. 6.3 shows how the AC varies as a function of the bias k for the CM defined in Eq. (6.2). It can be observed that AC decreases as the control parameter k moves away from the bifurcation point. The inset of panel (a) shows the hysteresis reported in [174] for the excitable regime of the CM, depending on whether the control parameter increases or decreases. Also, the peak of AC coincides with the bifurcation points: $k \approx 0.03$ for the excitable regime and $k \approx 0.022$.

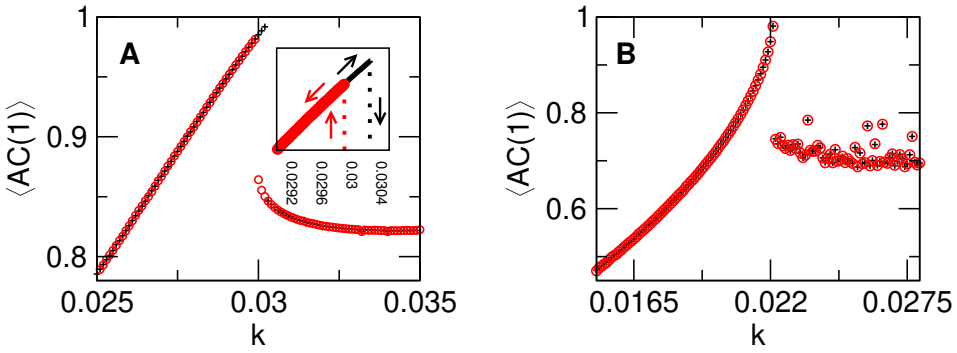

Figure 6.3 – Autocorrelation coefficient as a function of the control parameter of CM averaged over 10^2 samples, for excitable (a) and chaotic (b) regimes. The inset in panel (a) depicts the hysteresis for the excitable regime of the model. The evolution of AC is shown for both increasing and decreasing control parameter values, represented by black crosses and red circles, respectively.

Therefore, a control mechanism based on AC seems to be feasible for maps. The control strategy, presented in Ref. [166], is described by

$$\begin{aligned} d_i &= d_{i-1}.\mathrm{sgn}[AC_{(i)} - AC_{(i-1)}] \\ \delta_i &= (1 - AC_{(i)})^2 \\ k_{i+1} &= k_i + \delta.d.\kappa \end{aligned} \tag{6.5}$$

in which *sgn* is the sign function. The control is implemented using the parameter k, which may correspond to the number of postsynaptic receptors or the neuron's threshold, controlling the current it receives from other neurons. Starting from an initial value of k, Eq. (6.2) is simulated over a large number of iterations, and the average value of AC(1) for the activation variable is computed. Then, the AC(1) value at step i is compared with its value at the previous step $i-1$, which defines the sign of d_i. This means that when a decrease in AC(1) is detected, d_i changes its sign. In addition, the gradient toward the maximum value of AC(1) is computed by δ_i. These two values are used to adjust the control parameter for the next step, k_{i+1}. The constant κ is a small value ($\kappa = 0.0025$ in this work) used to determine the timescale at which the control parameter is adjusted.

The control strategy is applied to the CM for both excitable and chaotic regimes using 10^3 adaptation steps. For each of these steps, 4×10^4 iterations of the CM were considered after discarding a transient of 3×10^4 iterations. For the excitable regime, using parameters $(a, b, c) = (0.89, 0.60, 0.28)$, the results of the control mechanism are shown in Fig. 6.4.

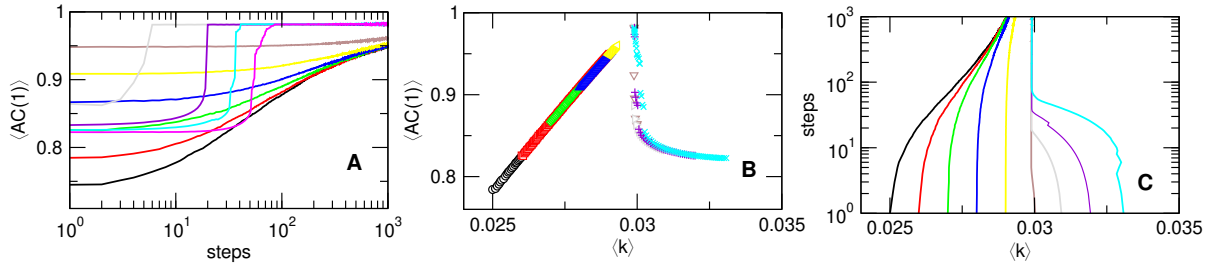

Figure 6.4 – Adaptive control of CM in the excitable regime. For all panels, data correspond to results averaged over 10^2 samples. Starting with different values of control parameter k, panels (a) and (c) show the evolution of AC(1) and k, respectively. Panel (b) shows AC(1) as a function of the control parameter.

First, Fig. 6.4(a) shows that for all initial conditions, AC(1) reaches its maximum value around 10^3 adaptation steps. Panel (b) depicts behavior very similar to that found

for AC without control (Fig. 6.3(a)). Panel (c) shows the evolution of the initial conditions across the adaptation steps. The control strategy successfully tunes the system to the critical value and keeps it poised at it. However, an interesting feature in this case is that instead of a single critical value, the control leads to two controlled values of k. This occurs due to the hysteresis in the excitable regime, which is also well reproduced by the control mechanism.

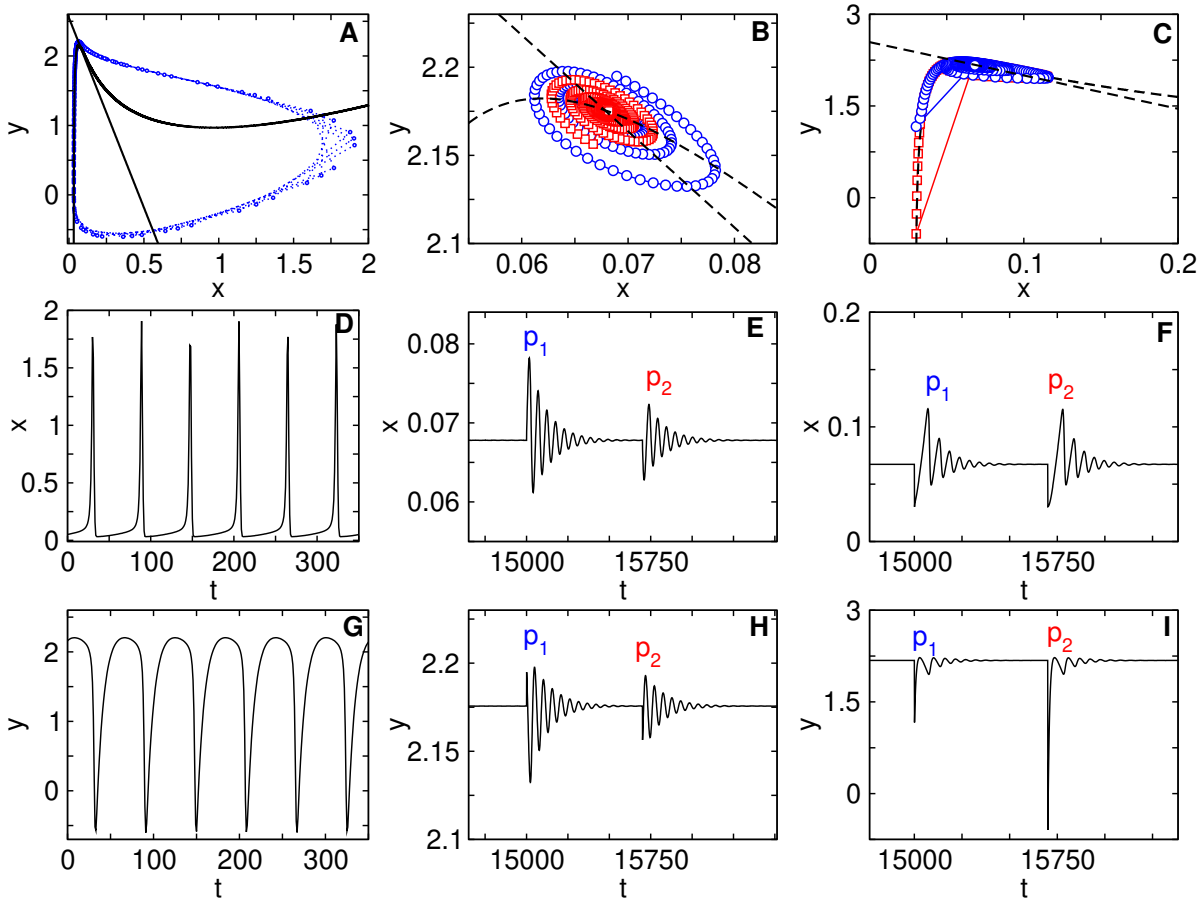

Figure 6.5 – Adaptive control of CM in the excitable regime. Panel (a) shows the evolution of the state variables (blue dotted lines) and the nullclines of Eq. (6.3) (black solid lines) without control for fixed $k = 0.031$ corresponding to the data in panels (d) and (g). Panels (b) and (c) show the evolution and the nullclines after the control is switched on and after two perturbations [panels (e) and (h), and panels (f) and (i), respectively]

The control mechanism for excitable dynamics is also illustrated in Fig. 6.5, where the CM without control (leftmost panels) is compared with the controlled version. The top panels in this figure show the solutions of Eq. (6.2) plotted in phase space, together with the overlapping nullclines of Eq. (6.3). The middle panels show the activation variables for the uncontrolled case, as well as for small and large perturbations. The

bottom panels show the same for the recovery variable. Thus, regardless of the amplitude of the perturbations, the system is led back to the controlled trajectories.

As discussed in Sec. 6.2, the Chialvo map can exhibit chaotic dynamics for certain regions of the parameter space. Chaotic bursting is characterized by aperiodic trajectories spiraling out of a repeller located in the proximity of the $(x = y = 1)$ region in phase space (see Fig. 6.6(a)). Thus, the same analysis of the control mechanism can be performed for the chaotic regime using $(a, b, c, k) = (0.89, 0.18, 0.28, 0.025)$.

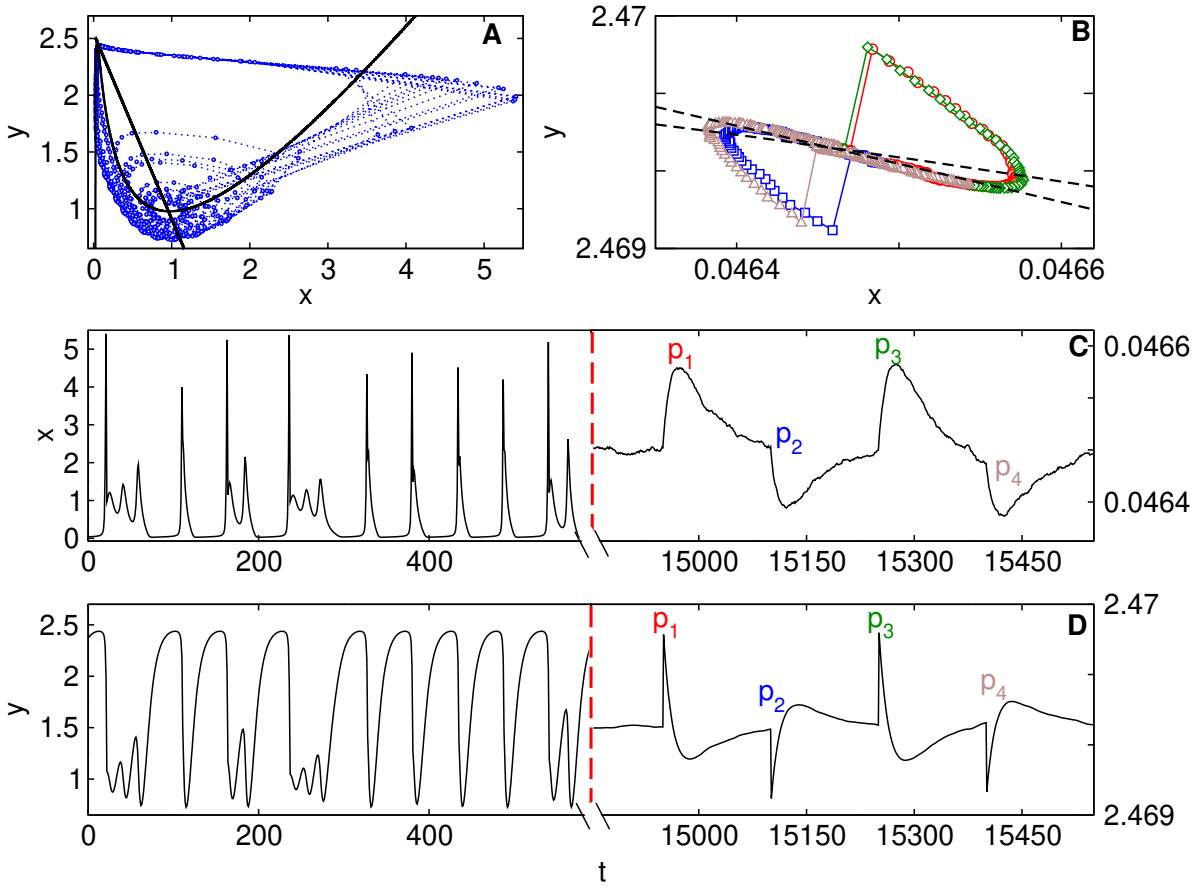

Figure 6.6 – Adaptive control of CM in the chaotic regime. In panel (a) the nullclines of Eq. (6.3) are displayed by black lines while the blue dotted lines show the trajectory for $k = 0.025$ of the CM solutions. The first half of panels (c) and (d) show the CM solutions without control. Panel (b) shows the nullclines (dashed lines) and the symbols are the trajectories of the system after small perturbations p_1, p_2, p_3, and p_4, are applied to the system now under control, which can be seen in the second half of panels (c) and (d).

Figure 6.6 pictures the solutions of the CM both without and with the control strategy under four perturbations in panels (a) and (b), respectively. In panel (b), it is possible to observe that the perturbed solutions are taken back to the controlled trajectory.

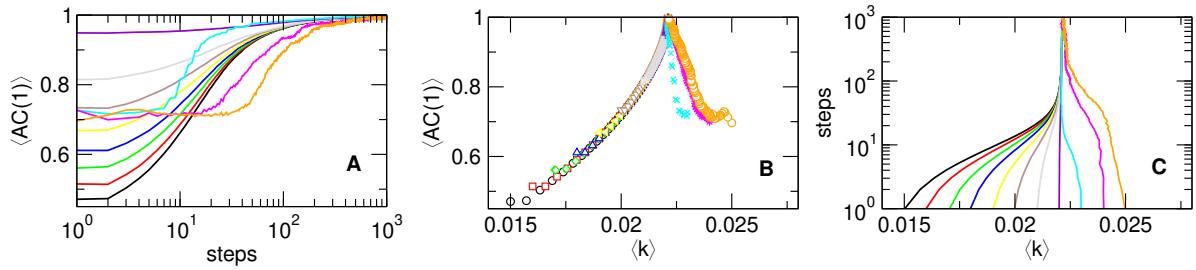

Figure 6.7 – Adaptive control of CM in the chaotic regime. For all panels, data correspond to results averaged over 10^2 samples. Starting with different values of control parameter k, panels (a) and (c) show the evolution of AC(1) and k, respectively. Panel (b) shows AC(1) as a function of the control parameter.

The leftmost part of panels (c) and (d) exhibits the chaotic state variables without control, and the rightmost parts show the action of four different perturbations on these state variables. Figure 6.7 shows the adaptive control strategy for the Chialvo map in the chaotic regime and how different initial conditions for k lead to a controlled bifurcation point, in agreement with previous analyses. It is possible to observe the resemblance of the AC function for the controlled system in panel (b) to the uncontrolled case shown in Fig. 6.3(b).

This work demonstrates that the slowdown of temporal correlations, which naturally occurs in a nonlinear system nearing instability, is sufficient to control and keep it close to that state. Furthermore, the presented control mechanism may be possibly employed in strategies that record and stimulate individual neurons monitored via optogenetic techniques [176], among other applications as tuning the system to its most sensitive point [177] and homeostatic regulation of neuronal firing and plasticity [178].

6.4 Concluding remarks

This chapter presented characteristics of brain dynamics that support the hypothesis of its operation in a critical regime. Paths toward a possible explanation of criticality in the brain were discussed, including the SOC mechanism, which justifies the application of control strategies in brain models. Using individual neuron modeling through the Chialvo map, we demonstrated the viability of a control strategy (originally applied to high-dimensional systems) when applied to low-dimensional models.

VII Summary and Prospects

Complex networks are a research field that has expanded significantly in the last few decades, primarily due to the vast amount of real data available, as well as their broad applicability across diverse areas of knowledge. The network-thinking perspective, corresponding to the identification of nodes and links in a complex system, has had a positive impact on the way these systems are investigated. For social systems, the idea of representing individuals as nodes and their interactions as links seems straightforward, and spreading processes, such as rumors and epidemics, are well represented as dynamical systems within this framework. Although many models leave out important aspects of real social systems, some relevant insights can still be obtained, such as how network structure affects the dynamics and the computation of an estimated epidemic threshold.

Furthermore, beyond the practical applications, spreading phenomena on top of complex networks have a theoretical aspect related to phase transitions. For instance, considering the thermodynamic limit, the epidemic threshold is the critical point of an absorbing-state phase transition (ASPT). Thus, concepts such as order parameter and susceptibility, first developed in the realm of equilibrium phase transitions, were adapted to investigate non-equilibrium cases such as ASPT. Chapter II focused on the network thinking of complex systems, as well as basic concepts and models for generating synthetic networks. Chapter III explored the contact process model (CP) and its modifications, as well as the susceptible-infected-susceptible (SIS) model on network structures to study criticality and phase transitions. These two chapters provided the fundamental background for the results presented in this thesis. The criticality in dynamical systems through complex networks was explored in two main projects: using visibility graphs and intermittent networks.

Chapter IV discussed the employment of the visibility graph (VG) method to map time series of epidemic prevalence onto graphs. These time series were generated from epidemic models presenting different natures of phase transitions. Using the degree correlations of the VG, we were able to distinguish between critical and off-critical regimes from epidemic models in homogeneous structures [31]. The off-critical time series presented only assortative degree correlations, while the cases belonging to the clean critical regimes presented asymptotic disassortativity. Determining whether a self-organized sys-

tem is critical or not is still a challenge in many real data applications, so the degree correlations of the VG method is shown as a promising alternative for tackling this issue. However, still concerning real systems, the original network structure where the dynamical process occurs is unknown in many cases. To address this, we extended the work on VG for spreading phenomena to heterogeneous networks containing different dynamical localization patterns. Our results showed that if the dynamical process is poisoned with strong localization, the criticality may be blurred. This means that even if the system is at an actual critical regime, the degree correlations of VG may not present the disassortative pattern that is the hallmark of criticality [32]. This work was also important to validate the method in the sense that no false positives were found in our analysis. In other words, in all cases where the asymptotic disassortative behavior was observed, the system was actually critical, indicating that the method remains effective in determining criticality in dynamical systems, provided that the localization is not extreme.

Chapter V explored the relation between the dynamics of a spreading process and the dynamics of contacts in a temporal network. We used a static backbone network structure to keep the maximum number of contacts for each node predetermined, and then, a dynamics of activation/inactivation is applied to the nodes or links. Each change in the state of a node or link was treated as an event, so that this dynamics could be expressed through a general renewal process. The heterogeneity in interactions, present in our daily life social contacts, was captured through an inter-event time distribution capable of presenting bursts of activity. Thus, heterogeneous inter-event times were used, and nodes or links could remain active/inactive for long periods or change their state rapidly. First, we suppressed the effects of localization in the backbone structure by analyzing a homogeneous network, for which the epidemic threshold was maximized when the average inter-event time was short and when the inter-event time distribution was less heterogeneous.

This approach was extended to heterogeneous backbone networks, such as those generated using the uncorrelated configuration model (UCM), including a finite-size analysis for network sizes ranging from $N = 10^3$ to $N = 10^7$ nodes. We found that for a degree exponent $\gamma = 3.5$, the node intermittency was able to suppress the multiple transitions in the susceptibility curves of the SIS model (common in these networks) while maintaining the same vanishing epidemic threshold behavior as the network size increased. When comparing the link and node intermittency strategies, we found that the former

resembled a simple reduction of contacts, while the latter indeed resulted in a nontrivial increase in the epidemic threshold. This result was also obtained using the susceptible-infected-recovered (SIR) model. Although this was a theoretical study using synthetic networks and inter-event time distributions, this result strongly suggests that a more effective strategy for containing a spreading process is the complete isolation of individuals for periods that are neither too long nor too heterogeneous.

Also in Ch. V, we investigated the SIS model using both homogeneous initial states and seed simulations, to estimate the behavior of the critical exponents for this model on node intermittent lattices. We varied the inter-event time distribution exponent to explore the effect of temporal heterogeneity. Using a less heterogeneous inter-event time distribution, with exponent $\beta = 3.5$, the qualitative behavior for the seed simulations was similar to that presented in the SIS model on static networks. However, when the inter-event time distribution was highly heterogeneous ($\beta = 2.5$), the previous result did not hold, and different patterns emerged in seed simulations. One of the prospects of this thesis is to continue investigating the SIS model on intermittent lattices to verify the possibility of temporal Griffiths phases (TGP) as a potential explanation for the deviations in critical behavior found in highly heterogeneous inter-event time distributions.

Chapter VI presented the critical brain hypothesis, as well as evidence supporting it. This hypothesis states that many optimal functionalities in the brain could only be explained if it operates in a state poised between order and disorder, i.e., at criticality. The concept of self-organized criticality was also discussed, including the hypothesis of an extended region of criticality in the brain. Additionally, in this chapter, the idea of criticality was explored through the successful application of a control mechanism to a low-dimensional individual neuron model [51]. The possibility of applying a control strategy to individual neuron models is important, as recent studies utilizing optogenetic techniques have enabled the stimulation and recording of individual neurons. Thus, the mechanism explored in this chapter could be relevant for tuning applications in the future. This chapter may be perceived as slightly separate from the other result chapters that focus on network approaches. However, critical dynamics in the brain is a prominent application for the VG method presented in this thesis. This project was already started during my research internship with the CEMSC^3 group. Although it has been put on hold, another prospect of this thesis is to resume it and use the VG method to investigate criticality in time series, not only related to brain activity but also in other real systems.

Bibliography

[1] S. A. Kivelson, J. M. Jiang, and J. Chang, *Statistical mechanics of phases and phase transitions*. Princeton Oxford: Princeton University Press, 2024.

[2] M. Henkel, M. Pleimling, H. Hinrichsen, and S. Lübeck, *Non-Equilibrium Phase Transitions*, vol. 2 of *Theoretical and Mathematical Physics*. Dordrecht: Springer, 2008.

[3] M. Le Bellac, F. Mortessagne, and G. G. Batrouni, *Equilibrium and non-equilibrium statistical thermodynamics*. Cambridge, UK ; New York: Cambridge University Press, 2004. OCLC: 144618541.

[4] J. Marro and R. Dickman, *Nonequilibrium Phase Transitions in Lattice Models*. Aléa-Saclay, Cambridge University Press, may 1999.

[5] R. Pastor-Satorras, C. Castellano, P. Van Mieghem, and A. Vespignani, "Epidemic processes in complex networks," *Reviews of Modern Physics*, vol. 87, no. 3, pp. 925–979, 2015.

[6] A. Arenas, W. Cota, J. Gómez-Gardeñes, S. Gómez, C. Granell, J. T. Matamalas, D. Soriano-Paños, and B. Steinegger, "Modeling the spatiotemporal epidemic spreading of covid-19 and the impact of mobility and social distancing interventions," *Phys. Rev. X*, vol. 10, p. 041055, Dec 2020.

[7] S. H. Strogatz, "Exploring complex networks," *Nature*, vol. 410, pp. 268–276, Mar. 2001.

[8] J. Ladyman and K. Wiesner, *What is a complex system?* Yale University Press, 2020.

[9] M. Newman, *Networks - An introduction*. OUP Oxford, 2010.

[10] A.-L. Barabási, *Network science*. Cambridge University Press, 2016.

[11] A.-L. Barabási, N. Gulbahce, and J. Loscalzo, "Network medicine: a network-based approach to human disease," *Nature Reviews Genetics*, vol. 12, pp. 56–68, Jan. 2011.

[12] K. Sugishita and N. Masuda, "Recurrence in the evolution of air transport networks," *Scientific Reports*, vol. 11, p. 5514, Mar. 2021.

[13] R. Albert and A.-L. Barabási, "Statistical mechanics of complex networks," *Rev. Mod. Phys.*, vol. 74, pp. 47–97, Jan 2002.

[14] M. A. Muñoz, R. Juhász, C. Castellano, and G. Ódor, "Griffiths Phases on Complex Networks," *Physical Review Letters*, vol. 105, p. 128701, Sept. 2010.

[15] S. Boccaletti, J. Almendral, S. Guan, I. Leyva, Z. Liu, I. Sendiña-Nadal, Z. Wang, and Y. Zou, "Explosive transitions in complex networks' structure and dynamics: Percolation and synchronization," *Physics Reports*, vol. 660, pp. 1–94, Nov. 2016.

[16] R. H. Shumway and D. S. Stoffer, *Time Series Analysis and Its Applications*. Springer, 2011.

[17] T.-P. Chang, H.-H. Ko, F.-J. Liu, P.-H. Chen, Y.-P. Chang, Y.-H. Liang, H.-Y. Jang, T.-C. Lin, and Y.-H. Chen, "Fractal dimension of wind speed time series," *Appl. Energy*, vol. 93, pp. 742–749, 2012.

[18] R. Glick and A. K. Rose, "Does a currency union affect trade? The time-series evidence," *Eur. Econ. Rev.*, vol. 46, pp. 1125–1151, 2002.

[19] R. G. Andrzejak, K. Lehnertz, F. Mormann, C. Rieke, P. David, and C. E. Elger, "Indications of nonlinear deterministic and finite-dimensional structures in time series of brain electrical activity: Dependence on recording region and brain state," *Phys. Rev. E*, vol. 64, p. 061907, 2001.

[20] D. P. Subha, P. K. Joseph, R. Acharya U, and C. M. Lim, "EEG Signal Analysis: A Survey," *J. Med. Syst.*, vol. 34, pp. 195–212, 2010.

[21] H. Kantz and T. Schreiber, eds., *Nonlinear time series analysis*. Cambridge nonlinear science series, Cambridge: Cambridge University Press, 2nd ed ed., 2003.

[22] Y. Zou, R. V. Donner, N. Marwan, J. F. Donges, and J. Kurths, "Complex network approaches to nonlinear time series analysis," *Physics Reports*, vol. 787, pp. 1–97, 2019.

[23] L. Lacasa, B. Luque, F. Ballesteros, J. Luque, and J. C. Nuño, "From time series to complex networks: The visibility graph," *Proceedings of the National Academy of Sciences of the United States of America*, vol. 105, no. 13, pp. 4972–4975, 2008.

[24] L. Lacasa, B. Luque, J. Luque, and J. C. Nuño, "The visibility graph: A new method for estimating the Hurst exponent of fractional Brownian motion," *EPL (Europhysics Letters)*, vol. 86, p. 30001, 2009.

[25] R. V. Donner and J. F. Donges, "Visibility graph analysis of geophysical time series: Potentials and possible pitfalls," *Acta Geophysica*, vol. 60, no. 3, pp. 589–623, 2012.

[26] M. Ahmadlou, H. Adeli, and A. Adeli, "New diagnostic EEG markers of the Alzheimer's disease using visibility graph," *Journal of Neural Transmission*, vol. 117, no. 9, pp. 1099–1109, 2010.

[27] J. Wang, C. Yang, R. Wang, H. Yu, Y. Cao, and J. Liu, "Functional brain networks in Alzheimer's disease: EEG analysis based on limited penetrable visibility graph and phase space method," *Physica A: Statistical Mechanics and its Applications*, vol. 460, pp. 174–187, Oct. 2016.

[28] G. Kutluana and İlker Türker, "Classification of cardiac disorders using weighted visibility graph features from ecg signals," *Biomedical Signal Processing and Control*, vol. 87, p. 105420, 2024.

[29] T. E. Harris, "Contact Interactions on a Lattice," *Ann. Probab.*, vol. 2, pp. 969–988, 1974.

[30] S. C. Ferreira, C. Castellano, and R. Pastor-Satorras, "Epidemic thresholds of the susceptible-infected-susceptible model on networks: A comparison of numerical and theoretical results," *Physical Review E - Statistical, Nonlinear, and Soft Matter Physics*, vol. 86, no. 4, pp. 1–8, 2012.

[31] J. T. Moraes and S. C. Ferreira, "Visibility graphs of critical and off-critical time series for absorbing state phase transitions," *Physical Review E*, vol. 108, p. 044309, Oct. 2023.

[32] J. T. Moraes and S. C. Ferreira, "Strong localization blurs the criticality of time series for spreading phenomena on networks," *Phys. Rev. E*, vol. 111, p. 044302, Apr 2025.

[33] C. Castellano and R. Pastor-Satorras, "Thresholds for Epidemic Spreading in Networks," *Physical Review Letters*, vol. 105, p. 218701, Nov. 2010.

[34] N. H. Fefferman and K. L. Ng, "How disease models in static networks can fail to approximate disease in dynamic networks," *Physical Review E*, vol. 76, p. 031919, Sept. 2007.

[35] P. Holme and J. Saramäki, *Temporal Networks*. Understanding Complex Systems, Berlin, Heidelberg: Springer, 2013.

[36] N. Masuda and R. Lambiotte, *A guide to temporal networks*, vol. 6 of *Series on complexity science*. New Jersey London Singapore Beijing Shanghai Hong Kong Taipei Chennai Tokyo: World Scientific, 2 ed., 2021.

[37] M. Karsai, H.-H. Jo, and K. Kaski, *Bursty Human Dynamics*. SpringerBriefs in Complexity, Cham: Springer International Publishing, 2018.

[38] C. Cattuto, W. Van Den Broeck, A. Barrat, V. Colizza, J.-F. Pinton, and A. Vespignani, "Dynamics of Person-to-Person Interactions from Distributed RFID Sensor Networks," *PLoS ONE*, vol. 5, p. e11596, July 2010.

[39] J. Fournet and A. Barrat, "Contact Patterns among High School Students," *PLoS ONE*, vol. 9, p. e107878, Sept. 2014.

[40] F. Vazquez, J. A. Bonachela, C. López, and M. A. Muñoz, "Temporal griffiths phases," *Phys. Rev. Lett.*, vol. 106, p. 235702, Jun 2011.

[41] E. Tagliazucchi, D. R. Chialvo, M. Siniatchkin, E. Amico, J.-F. Brichant, V. Bonhomme, Q. Noirhomme, H. Laufs, and S. Laureys, "Large-scale signatures of unconsciousness are consistent with a departure from critical dynamics," *Journal of The Royal Society Interface*, vol. 13, p. 20151027, Jan. 2016.

[42] J. M. Beggs and D. Plenz, "Neuronal Avalanches in Neocortical Circuits," *The Journal of Neuroscience*, vol. 23, pp. 11167–11177, Dec. 2003.

[43] J. M. Beggs, "The criticality hypothesis: how local cortical networks might optimize information processing," *Philosophical Transactions of the Royal Society A: Mathematical, Physical and Engineering Sciences*, vol. 366, pp. 329–343, Feb. 2008.

[44] T. Petermann, T. C. Thiagarajan, M. A. Lebedev, M. A. L. Nicolelis, D. R. Chialvo, and D. Plenz, "Spontaneous cortical activity in awake monkeys composed of neuronal avalanches," *Proceedings of the National Academy of Sciences*, vol. 106, pp. 15921–15926, Sept. 2009.

[45] T. L. Ribeiro, M. Copelli, F. Caixeta, H. Belchior, D. R. Chialvo, M. A. L. Nicolelis, and S. Ribeiro, "Spike Avalanches Exhibit Universal Dynamics across the Sleep-Wake Cycle," *PLoS ONE*, vol. 5, p. e14129, Nov. 2010.

[46] D. Fraiman, P. Balenzuela, J. Foss, and D. R. Chialvo, "Ising-like dynamics in large-scale functional brain networks," *Physical Review E*, vol. 79, p. 061922, June 2009.

[47] E. Tagliazucchi, P. Balenzuela, D. Fraiman, and D. R. Chialvo, "Criticality in Large-Scale Brain fMRI Dynamics Unveiled by a Novel Point Process Analysis," *Frontiers in Physiology*, vol. 3, 2012.

[48] A. Haimovici, E. Tagliazucchi, P. Balenzuela, and D. R. Chialvo, "Brain Organization into Resting State Networks Emerges at Criticality on a Model of the Human Connectome," *Physical Review Letters*, vol. 110, p. 178101, Apr. 2013.

[49] A. Fornito, A. Zalesky, and E. T. Bullmore, *Fundamentals of Brain Network Analysis*. San Diego: Elsevier Science & Technology, 2016.

[50] D. R. Chialvo, "Emergent complex neural dynamics," *Nature Physics*, vol. 6, pp. 744–750, Oct. 2010.

[51] J. T. Moraes, E. J. A. Trejo, S. Camargo, S. C. Ferreira, and D. R. Chialvo, "Self-tuned criticality: Controlling a neuron near its bifurcation point via temporal correlations," *Physical Review E*, vol. 107, p. 034204, Mar. 2023.

[52] P. Bak, *How Nature Works*. New York, NY: Springer New York, 1996.

[53] M. Mitchell, *Complexity: a guided tour*. New York, NY: Oxford University Press, 2009.

[54] P. W. Anderson, "More Is Different: Broken symmetry and the nature of the hierarchical structure of science.," *Science*, vol. 177, pp. 393–396, Aug. 1972.

[55] H. J. Jensen, *Complexity Science: The Study of Emergence*. Cambridge University Press, 1 ed., Nov. 2022.

[56] "Nobel Prize in Physics 2021." `https://www.nobelprize.org/prizes/physics/2021/summary/`. Acessed: Wed. 5 Mar. 2025.

[57] "Nobel Prize in Physics 2024." `https://www.nobelprize.org/prizes/physics/2024/summary/`. Acessed: Thur. 1 May. 2025.

[58] S. Thurner, P. Klimek, and R. Hanel, *Introduction to the Theory of Complex Systems*, vol. 1. Oxford University Press, Nov. 2018.

[59] G. L. Alexanderson, "About the cover: Euler and Königsberg's Bridges: A historical view," *Bulletin of the American Mathematical Society*, vol. 43, pp. 567–574, July 2006.

[60] H. Sachs, M. Stiebitz, and R. J. Wilson, "An historical note: Euler's Königsberg letters," *Journal of Graph Theory*, vol. 12, pp. 133–139, Mar. 1988.

[61] L. Euler, "Solutio problematis ad geometriam situs pertinentis," *Commentarii academiae scientiarum Petropolitanae*, pp. 128–140, Jan. 1741.

[62] "Kalingrad map." `https://maps.app.goo.gl/3me3ixTxtofpedG59`. Accessed 26 Mar. 2025.

[63] R. Guimerà, S. Mossa, A. Turtschi, and L. A. N. Amaral, "The worldwide air transportation network: Anomalous centrality, community structure, and cities' global roles," *Proceedings of the National Academy of Sciences*, vol. 102, pp. 7794–7799, May 2005.

[64] G. S. Costa, W. Cota, and S. C. Ferreira, "Outbreak diversity in epidemic waves propagating through distinct geographical scales," *Physical Review Research*, vol. 2, p. 043306, Dec. 2020.

[65] M. Bastian, S. Heymann, and M. Jacomy, "Gephi: An open source software for exploring and manipulating networks," *Proceedings of the International AAAI Conference on Web and Social Media*, 2009.

[66] "Google scholar juliane t. moraes." `https://scholar.google.com.br/citations?user=ZKaMrw8AAAAJ&hl=pt-BR`. Accessed 29 Mar. 2025.

[67] N. J. Van Eck and L. Waltman, "Software survey: VOSviewer, a computer program for bibliometric mapping," *Scientometrics*, vol. 84, pp. 523–538, Aug. 2010.

[68] R. Albert, H. Jeong, and A.-L. Barabási, "Diameter of the World-Wide Web," *Nature*, vol. 401, pp. 130–131, Sept. 1999.

[69] A.-L. Barabasi and R. Albert, "Emergence of Scaling in Random Networks," *Science*, vol. 286, pp. 509–512, Oct. 1999.

[70] R. Pastor-Satorras, A. Vázquez, and A. Vespignani, "Dynamical and correlation properties of the internet," *Physical Review Letters*, vol. 87, no. 25, pp. 258701–1–258701–4, 2001.

[71] M. E. J. Newman, "Assortative Mixing in Networks," *Physical Review Letters*, vol. 89, p. 208701, Oct. 2002.

[72] P. Erdős and A. Rényi, "On random graphs I," *Publicationes Mathematicae (Debrecen)*, vol. 6, pp. 290–297, 1959.

[73] B. Bollobás, *Random Graphs*. Cambridge University Press, 2 ed., Aug. 2001.

[74] E. N. Gilbert, "Random Graphs," *The Annals of Mathematical Statistics*, vol. 30, pp. 1141–1144, Dec. 1959.

[75] E. Bullmore and O. Sporns, "Complex brain networks: graph theoretical analysis of structural and functional systems," *Nature Reviews Neuroscience*, vol. 10, pp. 186–198, Mar. 2009.

[76] S. Milgram, "The Small-World Problem," *Psychology Today*, vol. 1, p. 61-67, May 1967.

[77] R. Cohen and S. Havlin, "Scale-Free Networks Are Ultrasmall," *Physical Review Letters*, vol. 90, p. 058701, Feb. 2003.

[78] M. Catanzaro, M. Boguñá, and R. Pastor-Satorras, "Generation of uncorrelated random scale-free networks," *Physical Review E - Statistical, Nonlinear, and Soft Matter Physics*, vol. 71, no. 2, pp. 1–4, 2005.

[79] M. Boguñá, R. Pastor-Satorras, and A. Vespignani, "Cut-offs and finite size effects in scale-free networks," *The European Physical Journal B*, vol. 38, pp. 205–209, Mar. 2004.

[80] S. N. Dorogovtsev, A. V. Goltsev, and J. F. F. Mendes, "Critical phenomena in complex networks," *Reviews of Modern Physics*, vol. 80, pp. 1275–1335, Oct. 2008.

[81] M. Boguñá, C. Castellano, and R. Pastor-Satorras, "Langevin approach for the dynamics of the contact process on annealed scale-free networks," *Physical Review E*, vol. 79, p. 036110, Mar. 2009.

[82] M. A. Muñoz, "*Colloquium* : Criticality and dynamical scaling in living systems," *Reviews of Modern Physics*, vol. 90, p. 031001, July 2018.

[83] D. Plenz and E. Niebur, eds., *Criticality in Neural Systems*. Wiley, 1 ed., Apr. 2014.

[84] C. D. Nadell, V. Bucci, K. Drescher, S. A. Levin, B. L. Bassler, and J. B. Xavier, "Cutting through the complexity of cell collectives," *Proceedings of the Royal Society B: Biological Sciences*, vol. 280, p. 20122770, Mar. 2013.

[85] A. Cavagna, A. Cimarelli, I. Giardina, G. Parisi, R. Santagati, F. Stefanini, and M. Viale, "Scale-free correlations in starling flocks," *Proceedings of the National Academy of Sciences*, vol. 107, pp. 11865–11870, June 2010.

[86] D. Sornette, *Why stock markets crash: critical events in complex financial systems*. Princeton, N.J: Princeton University Press, 2003.

[87] C. Castellano, S. Fortunato, and V. Loreto, "Statistical physics of social dynamics," *Rev. Mod. Phys.*, vol. 81, pp. 591–646, May 2009.

[88] P. Curie, *Propriétés magnétiques des corps à diverses températures*. Dissertations, Gauthier-Villars et fils, 1895.

[89] Z. Liu, E. Vatansever, G. T. Barkema, and N. G. Fytas, "Critical dynamical behavior of the ising model," *Phys. Rev. E*, vol. 108, p. 034118, Sep 2023.

[90] L. Onsager, "Crystal statistics. I. A two-dimensional model with an order-disorder transition," *Physical Review*, vol. 65, pp. 117–149, Feb. 1944.

[91] A. Lesne and M. Lagües, *Scale Invariance: From Phase Transitions to Turbulence*. Berlin, Heidelberg: Springer Berlin Heidelberg, 2012.

[92] L. Landau and E. Lifshitz, *Statistical Physics*. No. v. 5, Pergamon Press, 2011.

[93] N. Metropolis, A. W. Rosenbluth, M. N. Rosenbluth, A. H. Teller, and E. Teller, "Equation of State Calculations by Fast Computing Machines," *The Journal of Chemical Physics*, vol. 21, pp. 1087–1092, June 1953.

[94] M. Del Vicario, A. Bessi, F. Zollo, F. Petroni, A. Scala, G. Caldarelli, H. E. Stanley, and W. Quattrociocchi, "The spreading of misinformation online," *Proceedings of the National Academy of Sciences*, vol. 113, pp. 554–559, Jan. 2016.

[95] N. G. v. Kampen, *Stochastic processes in physics and chemistry.* Amsterdam ; New York : New York: North-Holland ; sole distributors for the USA and Canada, Elsevier North-Holland, 1981.

[96] M. J. Keeling and P. Rohani, *Modeling Infectious Diseases in humans and animals.* 2008.

[97] W. Kermack and A. G. McKendrick, "A contribution to the mathematical theory of epidemics," *Proceedings of the Royal Society of London. Series A, Containing Papers of a Mathematical and Physical Character*, vol. 115, pp. 700–721, Aug. 1927.

[98] R. Dickman, T. Tomé, and M. J. De Oliveira, "Sandpiles with height restrictions," *Physical Review E*, vol. 66, p. 016111, July 2002.

[99] S. Strogatz, *Nonlinear dynamics and chaos: with applications to physics, biology, chemistry, and engineering.* A Chapman & Hall book, Boca Raton London New York: CRC Press, second edition, first issued in hardback ed., 2019.

[100] W. Wang, Q.-H. Liu, J. Liang, Y. Hu, and T. Zhou, "Coevolution spreading in complex networks," *Physics Reports*, vol. 820, pp. 1–51, Aug. 2019.

[101] P. Grassberger, L. Chen, F. Ghanbarnejad, and W. Cai, "Phase transitions in cooperative coinfections: Simulation results for networks and lattices," *Physical Review E*, vol. 93, p. 042316, Apr. 2016.

[102] M. M. De Oliveira, R. V. Dos Santos, and R. Dickman, "Symbiotic two-species contact process," *Physical Review E*, vol. 86, p. 011121, July 2012.

[103] G. S. Costa, M. M. De Oliveira, and S. C. Ferreira, "Heterogeneous mean-field theory for two-species symbiotic processes on networks," *Physical Review E*, vol. 106, p. 024302, Aug. 2022.

[104] M. M. De Oliveira, S. G. Alves, and S. C. Ferreira, "Dynamical correlations and pairwise theory for the symbiotic contact process on networks," *Physical Review E*, vol. 100, p. 052302, Nov. 2019.

[105] R. B. Griffiths, "Nonanalytic Behavior Above the Critical Point in a Random Ising Ferromagnet," *Physical Review Letters*, vol. 23, pp. 17–19, July 1969.

[106] T. Vojta, "Rare region effects at classical, quantum and nonequilibrium phase transitions," *Journal of Physics A: Mathematical and General*, vol. 39, pp. R143–R205, June 2006.

[107] T. Vojta, "Disorder-Induced Rounding of Certain Quantum Phase Transitions," *Physical Review Letters*, vol. 90, p. 107202, Mar. 2003.

[108] T. Vojta and M. Dickison, "Critical behavior and Griffiths effects in the disordered contact process," *Physical Review E*, vol. 72, p. 036126, Sept. 2005.

[109] M. Dickison and T. Vojta, "Monte Carlo simulations of the smeared phase transition in a contact process with extended defects," *Journal of Physics A: Mathematical and General*, vol. 38, pp. 1199–1208, Feb. 2005.

[110] W. Cota, G. Ódor, and S. C. Ferreira, "Griffiths phases in infinite-dimensional, non-hierarchical modular networks," *Scientific Reports*, vol. 8, p. 9144, June 2018.

[111] P. Moretti and M. A. Muñoz, "Griffiths phases and the stretching of criticality in brain networks," *Nature Communications*, vol. 4, p. 2521, Oct. 2013.

[112] R. S. Sander, G. S. Costa, and S. C. Ferreira, "Sampling methods for the quasi-stationary regime of epidemic processes on regular and complex networks," *Physical Review E*, vol. 94, no. 4, pp. 1–12, 2016.

[113] R. Pastor-Satorras and A. Vespignani, "Epidemic Spreading in Scale-Free Networks," *Physical Review Letters*, vol. 86, no. 14, pp. 3200–3203, 2001.

[114] R. Pastor-Satorras and A. Vespignani, "Epidemic dynamics and endemic states in complex networks," *Physical Review E*, vol. 63, p. 066117, May 2001.

[115] M. Boguñá and R. Pastor-Satorras, "Epidemic spreading in correlated complex networks," *Physical Review E*, vol. 66, p. 047104, Oct. 2002.

[116] S. Chatterjee and R. Durrett, "Contact processes on random graphs with power law degree distributions have critical value 0," *The Annals of Probability*, vol. 37, Nov. 2009.

[117] D. Chakrabarti, Y. Wang, C. Wang, J. Leskovec, and C. Faloutsos, "Epidemic thresholds in real networks," *ACM Transactions on Information and System Security*, vol. 10, pp. 1–26, Jan. 2008.

[118] F. Chung, L. Lu, and V. Vu, "Spectra of random graphs with given expected degrees," *Proceedings of the National Academy of Sciences*, vol. 100, pp. 6313–6318, May 2003.

[119] A. S. Mata and S. C. Ferreira, "Pair quenched mean-field theory for the susceptible-infected-susceptible model on complex networks," *EPL (Europhysics Letters)*, vol. 103, p. 48003, Aug. 2013.

[120] M. Boguñá, C. Castellano, and R. Pastor-Satorras, "Nature of the Epidemic Threshold for the Susceptible-Infected-Susceptible Dynamics in Networks," *Physical Review Letters*, vol. 111, p. 068701, Aug. 2013.

[121] S. C. Ferreira, R. S. Sander, and R. Pastor-Satorras, "Collective versus hub activation of epidemic phases on networks," *Physical Review E*, vol. 93, no. 3, pp. 1–10, 2016.

[122] M. Kitsak, L. K. Gallos, S. Havlin, F. Liljeros, L. Muchnik, H. E. Stanley, and H. A. Makse, "Identification of influential spreaders in complex networks," *Nature Physics*, vol. 6, no. 11, pp. 888–893, 2010.

[123] C. Castellano and R. Pastor-Satorras, "Competing activation mechanisms in epidemics on networks," *Scientific Reports*, vol. 2, 2012.

[124] S. D. Campbell and F. X. Diebold, "Weather Forecasting for Weather Derivatives," *J. Am. Stat. Assoc.*, vol. 100, pp. 6–16, 2005.

[125] P. Gopikrishnan, V. Plerou, L. A. Nunes Amaral, M. Meyer, and H. E. Stanley, "Scaling of the distribution of fluctuations of financial market indices," *Phys. Rev. E*, vol. 60, pp. 5305–5316, 1999.

[126] P. Gopikrishnan, "Financial time series: A physics perspective," in *AIP Conference Proceedings*, vol. 519, (Fukuoka (Japan)), pp. 667–680, AIP, 2000.

[127] S. J. Clark and A. N. Turner, "Monitoring epidemics: Lessons from measuring population prevalence of the coronavirus," *Proceedings of the National Academy of Sciences of the United States of America*, vol. 118, no. 9, pp. 1–3, 2021.

[128] N. H. Packard, J. P. Crutchfield, J. D. Farmer, and R. S. Shaw, "Geometry from a Time Series," *Physical Review Letters*, vol. 45, pp. 712–716, Sept. 1980.

[129] F. Takens, "Detecting strange attractors in turbulence," in *Lecture notes in mathematics*, pp. 366–381, Springer, 1981.

[130] R. V. Donner, M. Small, J. F. Donges, N. Marwan, Y. Zou, R. Xiang, and J. Kurths, "RECURRENCE-BASED TIME SERIES ANALYSIS BY MEANS OF COMPLEX NETWORK METHODS," *International Journal of Bifurcation and Chaos*, vol. 21, pp. 1019–1046, Apr. 2011.

[131] P. Meakin, *Fractals, Scaling and Growth Far from Equilibrium*. Cambridge Nonlinear Science Series, Cambridge University Press, 1998.

[132] R. B. Davies and D. S. Harte, "Tests for hurst effect," *Biometrika*, vol. 74, no. 1, pp. 95–101, 1987.

[133] C. Flynn, "Fractional brownian motion realizations." Accessed 26 Apr. 2025.

[134] C. Liu, W. X. Zhou, and W. K. Yuan, "Statistical properties of visibility graph of energy dissipation rates in three-dimensional fully developed turbulence," *Physica A: Statistical Mechanics and its Applications*, vol. 389, no. 13, pp. 2675–2681, 2010.

[135] T. Vojta and J. A. Hoyos, "Criticality and Quenched Disorder: Harris Criterion Versus Rare Regions," *Physical Review Letters*, vol. 112, p. 075702, Feb. 2014.

[136] A. S. Mata and S. C. Ferreira, "Multiple transitions of the susceptible-infected-susceptible epidemic model on complex networks," *Physical Review E - Statistical, Nonlinear, and Soft Matter Physics*, vol. 91, no. 1, pp. 1–9, 2015.

[137] B. Min, K.-I. Goh, and A. Vazquez, "Spreading dynamics following bursty human activity patterns," *Physical Review E*, vol. 83, p. 036102, Mar. 2011.

[138] N. Masuda, K. Klemm, and V. M. Eguíluz, "Temporal Networks: Slowing Down Diffusion by Long Lasting Interactions," *Physical Review Letters*, vol. 111, p. 188701, Oct. 2013.

[139] P. Holme, "Modern temporal network theory: a colloquium," *The European Physical Journal B*, vol. 88, p. 234, Sept. 2015.

[140] L. Han, Z. Lin, Q. Yin, M. Tang, S. Guan, and M. Boguñá, "Non-Markovian epidemic spreading on temporal networks," *Chaos, Solitons & Fractals*, vol. 173, p. 113664, Aug. 2023.

[141] L. E. C. Rocha and V. D. Blondel, "Bursts of Vertex Activation and Epidemics in Evolving Networks," *PLoS Computational Biology*, vol. 9, p. e1002974, Mar. 2013.

[142] P. Holme, "Temporal network structures controlling disease spreading," *Physical Review E*, vol. 94, p. 022305, Aug. 2016.

[143] J.-P. Eckmann, E. Moses, and D. Sergi, "Entropy of dialogues creates coherent structures in e-mail traffic," *Proceedings of the National Academy of Sciences*, vol. 101, pp. 14333–14337, Oct. 2004.

[144] M. Karsai, M. Kivelä, R. K. Pan, K. Kaski, J. Kertész, A.-L. Barabási, and J. Saramäki, "Small but slow world: How network topology and burstiness slow down spreading," *Physical Review E*, vol. 83, p. 025102, Feb. 2011.

[145] J. Candia, M. C. González, P. Wang, T. Schoenharl, G. Madey, and A.-L. Barabási, "Uncovering individual and collective human dynamics from mobile phone records," *Journal of Physics A: Mathematical and Theoretical*, vol. 41, p. 224015, June 2008.

[146] J. F. Shortle, J. M. Thompson, D. Gross, and C. M. Harris, *Fundamentals of Queueing Theory*. Wiley Series in Probability and Statistics, Wiley, 1 ed., Jan. 2018.

[147] A. Vázquez, J. G. Oliveira, Z. Dezsö, K.-I. Goh, I. Kondor, and A.-L. Barabási, "Modeling bursts and heavy tails in human dynamics," *Physical Review E*, vol. 73, p. 036127, Mar. 2006.

[148] A. Vazquez, B. Rácz, A. Lukács, and A.-L. Barabási, "Impact of Non-Poissonian Activity Patterns on Spreading Processes," *Physical Review Letters*, vol. 98, p. 158702, Apr. 2007.

[149] W. Feller, *An Introduction to Probability Theory and Its Applications*, vol. II. Wiley, 2 ed., 1971.

[150] M. Karsai, K. Kaski, A.-L. Barabási, and J. Kertész, "Universal features of correlated bursty behaviour," *Scientific Reports*, vol. 2, p. 397, May 2012.

[151] H. Barghathi, T. Vojta, and J. A. Hoyos, "Contact process with temporal disorder," *Phys. Rev. E*, vol. 94, p. 022111, Aug 2016.

[152] D. Plenz, "The Critical Brain," *Physics*, vol. 6, p. 47, Apr. 2013.

[153] "What is Alzheimer's?." `https://www.alz.org/alzheimers-dementia/what-is-alzheimers`. Acessed: Wed. 19 Mar. 2025.

[154] R. Brookmeyer, E. Johnson, K. Ziegler-Graham, and H. M. Arrighi, "Forecasting the global burden of Alzheimer's disease," *Alzheimer's & Dementia*, vol. 3, pp. 186–191, July 2007.

[155] P. Hagmann, L. Cammoun, X. Gigandet, R. Meuli, C. J. Honey, V. J. Wedeen, and O. Sporns, "Mapping the Structural Core of Human Cerebral Cortex," *PLoS Biology*, vol. 6, p. e159, July 2008.

[156] W. J.G., S. E., T. J.N., and B. S., "The structure of the nervous system of the nematode *Caenorhabditis elegans*," *Philosophical Transactions of the Royal Society of London. B, Biological Sciences*, vol. 314, pp. 1–340, Nov. 1986.

[157] A. Lin, R. Yang, S. Dorkenwald, A. Matsliah, A. R. Sterling, P. Schlegel, S.-c. Yu, C. E. McKellar, M. Costa, K. Eichler, A. S. Bates, N. Eckstein, J. Funke, G. S. X. E. Jefferis, and M. Murthy, "Network statistics of the whole-brain connectome of Drosophila," *Nature*, vol. 634, pp. 153–165, Oct. 2024.

[158] O. Sporns, G. Tononi, and R. Kötter, "The Human Connectome: A Structural Description of the Human Brain," *PLoS Computational Biology*, vol. 1, no. 4, p. e42, 2005.

[159] K. J. Friston, "Functional and effective connectivity in neuroimaging: A synthesis," *Human Brain Mapping*, vol. 2, pp. 56–78, Jan. 1994.

[160] T. Mora and W. Bialek, "Are biological systems poised at criticality?," *Journal of Statistical Physics*, vol. 144, pp. 268–302, 2011.

[161] T. E. Harris, *The theory of branching processes*. Dover phoenix editions, New York: Dover, 1989. OCLC: 860376338.

[162] J. M. Beggs and D. Plenz, "Neuronal Avalanches Are Diverse and Precise Activity Patterns That Are Stable for Many Hours in Cortical Slice Cultures," *The Journal of Neuroscience*, vol. 24, pp. 5216–5229, June 2004.

[163] O. Kinouchi and M. Copelli, "Optimal dynamical range of excitable networks at criticality," *Nature Physics*, vol. 2, pp. 348–351, May 2006.

[164] P. Bak, C. Tang, and K. Wiesenfeld, "Self-organized criticality: An explanation of the $1/f$ noise," *Physical Review Letters*, vol. 59, pp. 381–384, July 1987.

[165] N. W. Watkins, G. Pruessner, S. C. Chapman, N. B. Crosby, and H. J. Jensen, "25 Years of Self-organized Criticality: Concepts and Controversies," *Space Science Reviews*, vol. 198, pp. 3–44, Jan. 2016.

[166] D. R. Chialvo, S. A. Cannas, T. S. Grigera, D. A. Martin, and D. Plenz, "Controlling a complex system near its critical point via temporal correlations," *Scientific reports*, vol. 10, no. 1, p. 12145, 2020.

[167] P. Bak and D. R. Chialvo, "Adaptive learning by extremal dynamics and negative feedback," *Physical Review E*, vol. 63, p. 031912, Feb. 2001.

[168] A. Levina, J. M. Herrmann, and T. Geisel, "Dynamical synapses causing self-organized criticality in neural networks," *Nature Physics*, vol. 3, pp. 857–860, Dec. 2007.

[169] R. Dickman, M. A. Muñoz, A. Vespignani, and S. Zapperi, "Paths to self-organized criticality," *Brazilian Journal of Physics*, vol. 30, pp. 27–41, Mar. 2000.

[170] H. Hoffmann and D. W. Payton, "Optimization by Self-Organized Criticality," *Scientific Reports*, vol. 8, p. 2358, Feb. 2018.

[171] S.-J. Wang and C. Zhou, "Hierarchical modular structure enhances the robustness of self-organized criticality in neural networks," *New Journal of Physics*, vol. 14, p. 023005, Feb. 2012.

[172] "Brain facts: a primer on the brain and nervous system.." `https://www.brainfacts.org:443/the-brain-facts-book`. Acessed: Sat. 22 Mar. 2025.

[173] M. Girardi-Schappo, M. H. R. Tragtenberg, and O. Kinouchi, "A brief history of excitable map-based neurons and neural networks," *Journal of neuroscience methods*, vol. 220, no. 2, pp. 116–130, 2013.

[174] D. R. Chialvo, "Generic excitable dynamics on a two-dimensional map," *Chaos, Solitons & Fractals*, vol. 5, no. 3-4, pp. 461–479, 1995.

[175] G. E. P. Box, G. M. Jenkins, G. C. Reinsel, and G. M. Ljung, *Time series analysis: forecasting and control*. Wiley series in probability and statistics, Hoboken, New Jersey: Wiley, fifth edition ed., 2016.

[176] J. P. Newman, M.-f. Fong, D. C. Millard, C. J. Whitmire, G. B. Stanley, and S. M. Potter, "Optogenetic feedback control of neural activity," *Elife*, vol. 4, p. e07192, 2015.

[177] V. M. Eguíluz, M. Ospeck, Y. Choe, A. Hudspeth, and M. O. Magnasco, "Essential nonlinearities in hearing," *Physical Review Letters*, vol. 84, no. 22, p. 5232, 2000.

[178] G. G. Turrigiano and S. B. Nelson, "Homeostatic plasticity in the developing nervous system," *Nature Reviews Neuroscience*, vol. 5, pp. 97–107, Feb. 2004.

[179] T. Tomé and M. J. De Oliveira, *Stochastic Dynamics and Irreversibility*. Graduate Texts in Physics, Cham: Springer International Publishing, 2015.

[180] M. M. De Oliveira and R. Dickman, "How to simulate the quasistationary state," *Physical Review E*, vol. 71, p. 016129, Jan. 2005.

[181] D. T. Gillespie, "A general method for numerically simulating the stochastic time evolution of coupled chemical reactions," *Journal of Computational Physics*, vol. 22, pp. 403–434, Dec. 1976.

[182] W. Cota and S. C. Ferreira, "Optimized Gillespie algorithms for the simulation of Markovian epidemic processes on large and heterogeneous networks," *Computer Physics Communications*, vol. 219, pp. 303–312, 2017.

[183] X. Lan, H. Mo, S. Chen, Q. Liu, and Y. Deng, "Fast transformation from time series to visibility graphs," *Chaos: An Interdisciplinary Journal of Nonlinear Science*, vol. 25, p. 083105, Aug. 2015.

Appendix

APPENDIX A – Generating complex networks

Optimized storage of connections

As mentioned in Sec. 2.3 of Chapter II, some networks may have a number of links ℓ that is much smaller than the maximum possible number if the network were fully connected. This results in a sparse adjacency matrix with many zero entries. As the network size increases, storing such a matrix becomes increasingly inefficient from a computational perspective. In many applications presented in this thesis, finite-size analysis was required, as we aimed to understand the behavior of dynamic processes on networks approaching the thermodynamic limit $N \to \infty$. Therefore, we review here an optimized method for storing network connections, which uses a set of three lists, encoded using vector structures in the C programming language. These lists are:

1. Degree list ($d[i]$): Stores the degree of each node i, such that the size of the list is equal to the number of nodes in the network.

2. Adjacency list ($a[i]$): Contains the connections of each node. Since each undirected link is stored twice (once for each endpoint), the total size of this list is 2ℓ.

3. Auxiliary list ($x[i]$): Used to index the adjacency list. It marks the starting position of the connections for each node i in the adjacency list, meaning that the neighbors of node i are stored starting from $a[x[i]]$.

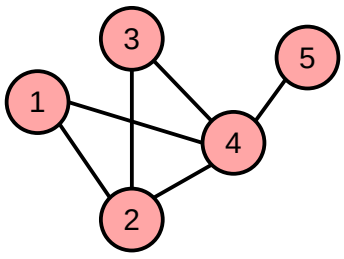

$$d = \{2, 3, 2, 4, 1\}$$

$$a = \{\underbrace{2, 4}_{\text{node 1}}, \underbrace{1, 3, 4}_{\text{node 2}}, \underbrace{2, 4}_{\text{node 3}}, \underbrace{1, 2, 3, 5}_{\text{node 4}}, \underbrace{4}_{\text{node 5}}\}$$

$$x = \{0, 2, 5, 7, 11\}$$

Figure 1.1 – Schematic representation of a network and its corresponding lists.

Figure 1.1 presents an example of a simple network and its corresponding representation using lists. This method allows efficient access to all information about the network's connections while also significantly reduces memory usage. Assuming each connection is stored as an integer variable occupying 4 bytes, the memory required for the largest vector (the adjacency list $a[i]$) is approximately $4 \times N \langle k \rangle$. In contrast, representing the same network with an adjacency matrix would require $4 \times N^2$ bytes, making the list-based method much more efficient, especially for sparse networks.

Uncorrelated Configuration Model

The Configuration Model generates random networks with a prescribed degree sequence, which, in principle, should exhibit no degree correlations due to the randomness of the connections [9]. However, as pointed out in [78], when dealing with scale-free networks for which the second moment of the degree distribution, $\langle k^2 \rangle$, diverges in the limit $N \to \infty$, a non-negligible number of self-connections and multiple links tend to appear. The problem is that simply forbidding such connections introduces degree correlations. To address this issue, one must impose a structural cutoff on the degree sequence, limiting the maximum degree to $k_s(N) \sim \sqrt{\langle k \rangle N}$. This constraint prevents the emergence of self- and multiple links and simultaneously avoids the introduction of correlations, as discussed in [79]. The uncorrelated configuration model (UCM), introduced in [78], incorporates this structural cutoff to produce random networks with a given degree distribution and neutral (i.e., uncorrelated) degree correlations.

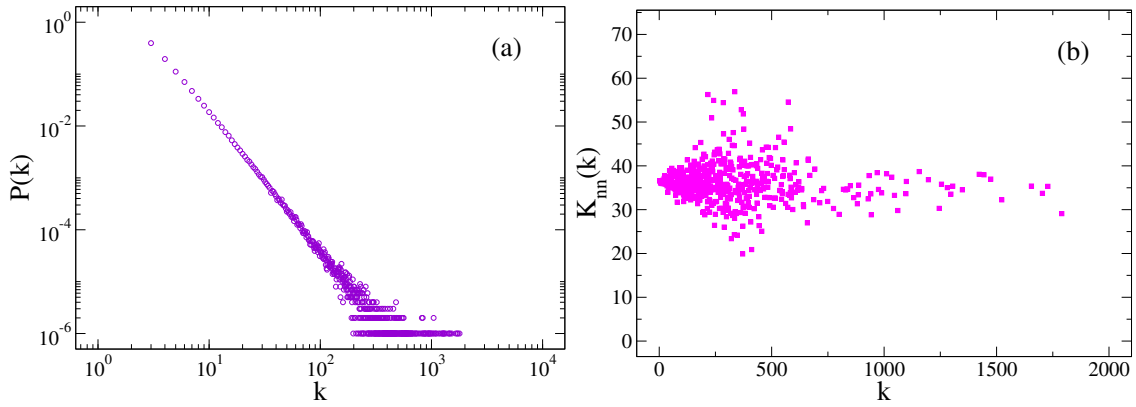

Figure 1.2 – Example of degree distribution (a) and degree correlations (b) of a network generated from UCM using $\gamma = 2.75$ and $N = 10^6$. The neutral behavior of degree correlations is expressed through the $\mu \approx 0$ considering $K_{\rm nn}(k) \sim k^{\mu}$ in panel (b).

The UCM was used to generate power-law degree distributed networks, and the computational time for a network of size $N = 10^6$ is of the order of seconds. Figure 1.2 shows the degree distribution in panel (a) and the degree correlations in panel (b) for a network generated using the UCM. It is possible to observe that the network is uncorrelated through the neutral pattern of $K_{\rm nn}(k)$. The degree correlations measured through the average degree of the nearest neighbors are discussed in Sec. 2.3.

The implementation of the UCM is described in the following steps.

(*i*) The first step is to determine the degrees of all nodes in the network according to the degree distribution and assign to each node a number of stubs corresponding to its degree. An example of a degree sequence is shown in Fig. 1.3(a). The degree distribution $P(k)$ must be defined in the interval $k_0 \leq k \leq k_c$, where k_c is the upper cutoff and k_0 is the minimum degree. In this thesis, we use $k_c = 2\sqrt{N}$ and $k_0 = 3$. This also ensures that the occurrence of self-loops or multiple links (illustrated in Fig. 1.3(c)) will be negligible. Additionally, the sum of all degrees must be even to ensure that no stub is left unconnected.

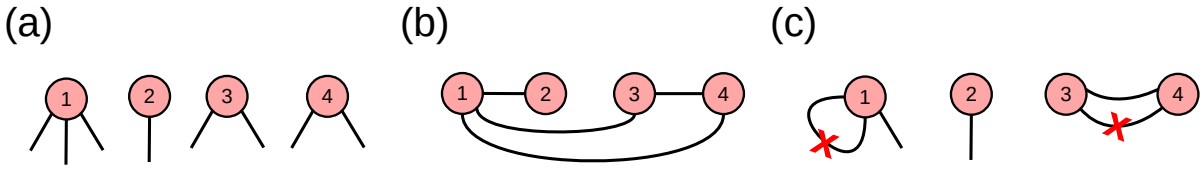

Figure 1.3 – Schematic illustration of the UCM implementation. (a) The stubs are distributed following a sequence of random degrees. In this example, the degree list is $d = \{3, 1, 2, 2\}$. (b) Links between two randomly chosen nodes. (c) Examples of multiple and self-links, which are forbidden in this model.

(*ii*) The second step is to randomly select two stubs and connect the nodes from which they belong, as in Fig. 1.3 (b), if this connection is not a self- or multiple link.

(*iii*) For connecting the whole network, step (*ii*) must be repeated until all stubs are used. At the end of the loop for the connection, if there are some stubs unconnected, all the links must be discarded and the steps restarted, drawing the degree distribution for another random seed.

APPENDIX B – Handling the quasi-stationary state

The absorbing state phase transitions (ASPT) appear in many parts of this thesis. For this class of transitions, finite-size effects are mainly relevant in two aspects: (i) As the control parameter λ approaches its critical value λ_c, the spatial correlation length $\xi_\perp$ increases but does not diverge, as it is limited by the lateral system size L. This causes the singularities, characteristics of infinite systems at criticality, to be both shifted from their true values and rounded, making the phase transition unobservable for finite systems. (ii) The second aspect is that, in a finite system, there is always a non-zero probability of reaching the absorbing state. Thus, even for $\lambda > \lambda_c$, the system can still fall into the absorbing state, meaning that the active steady state is no longer stable [2].

Therefore, for the models described in this thesis that exhibit ASPT in finite systems, the only true stationary state is the absorbing one. Thus, to study the active states using simulations in finite systems, we must consider a *quasi-stationary state*, which is reached after a certain transient period [4]. To establish the quasi-stationary state, it is possible to perturb the system by introducing activity that prevents it from becoming trapped in the absorbing state, using quasi-stationary (QS) methods. To explain how these perturbations can be implemented, the procedure outlined in reference [112] will be followed.

Given a stochastic process X_t allowing transitions between different configurations $n \to n \pm 1$ with $n = 0, 1, 2, \ldots$, the state $n = 0$ is considered the absorbing one. The transitions between different states m and n are governed by the rates w_{nm} [179]. We also define a similar process, X_t^*, for which $n = 0$ is no longer an absorbing state. The evolutions of X_t and X_t^* are equivalent for $n > 0$, apart from perturbations that may become negligible in the limit $N \to \infty$. Let P_n and P_n^* denote the probabilities of the system being in state n for the original process X_t and the modified process X_t^*, respectively. For the original dynamics, we have

$$\frac{dP_n}{dt} = \sum_m (w_{nm}P_m - w_{mn}P_n). \tag{2.1}$$

And for the modified dynamics

$$\frac{dP_n^*}{dt} = \sum_m [w_{nm}P_m^* - w_{mn}P_n^*] \; + \; F(P_0^*, P_1^*, ...) \; , \tag{2.2}$$

where F is a functional that can be adjusted according to the QS method being used, it is interpreted as a perturbative source. The stationary solution of Eq. (2.2) will lead to the QS distribution $\overline{P}_n$, from which it is possible to extract quantities of interest.

The standard QS method (SQS) consists of computing averages only over samples that did not visit an absorbing state. For this method in the context of spreading processes, the QS distribution is

$$\overline{P}_n = \lim_{t\to\infty} \frac{P_n(t)}{P_s(t)} \; , n > 0 \; , \tag{2.3}$$

where $P_s(t)$ is the probability that the dynamics is active at time t, and it is given by

$$P_s(t) = \sum_{n\geq 1} P_n(t) = 1 - P_o(t) \; . \tag{2.4}$$

This strategy may be difficult to implement, as the subcritical and critical regimes are frequently trapped in the absorbing state. As discussed in reference [180], one way to address this issue is to force the system to jump to an active configuration whenever the dynamics reach the absorbing state. This active configuration must be selected according to the QS probability distribution. In this case, it can be shown that the functional F in Eq. (2.2) takes the form $F = w_0 P_n^*$, where $w_0 = \sum_{m\neq 0} w_{0m}$ is the total rate of transition into the absorbing state. In practice, the QS probability distribution is not known. So, for computational purposes, one possible strategy is to construct and continuously update a list of configurations visited during the simulation. One of these configurations is then selected to be reestablished whenever the system reaches the absorbing state. As discussed in [112], although the SQS method is theoretically well-founded, it can be computationally less efficient than other possible approaches and also algorithmically more complicated. For this reason, it was not used in the simulations presented in this thesis. Instead, the approaches adopted to handle the quasi-stationary states are the following.

One possible way to handle the absorbing state is to allow it to occur, but then return the system to the configuration it occupied immediately before reaching the absorbing state, which characterizes a reflecting boundary condition (RBC) [98]. In terms

of the stochastic process discussed above, this is equivalent to allowing the state $n = 0$ to occur, but returning to the previous state with rate 1. This corresponds to using the perturbative source as $F = (\delta_{1,n} - \delta_{0,n})P_n^*$. Since the QS distribution is given by

$$\overline{P}_n = \lim_{t\to\infty} P_n^* \ , \tag{2.5}$$

if $n = 0$, Eq. (2.2) becomes

$$\frac{dP_0^*}{dt} = P_1^* - P_0^* \ , \tag{2.6}$$

so, for the QS regime, $\overline{P}_1 = \overline{P}_0$. This allows for the computation of averaged quantities of interest in the system's dynamics, such as the density of infected individuals. Although this method has a simple computational implementation, it should not be used for all network structures, as it differs significantly from the SQS in the case of heterogeneous networks [112]. Therefore, in this thesis, the RBC was used only in cases where the network is homogeneous, for instance, in lattices or RRNs.

The second QS method used in this thesis is the hub reactivation (HR), which is similar to the RBC, but instead of returning the system to the immediately previous configuration, the node of largest degree in the network must be reactivated. If there are two hubs with the same degree, one of them must be randomly selected. The primary motivation behind this strategy is the existence of localized active phases around the hubs for spreading processes, as the SIS [136]. It is important to mention that the HR method shows good agreement with the SQS in many cases [112]. Therefore, as it is easily implemented and computationally efficient, this method was used for the simulations in this thesis in cases where the original network structure was heterogeneous and localized.

APPENDIX C – Optimized Gillespie Algorithm

The epidemic models used to simulate spreading processes in this thesis are characterized by some important aspects: the events (healing, recovery, and infection) happen randomly in time with rates that are not time-dependent, and the probability of multiple events in an infinitesimal time is negligible, meaning that each event will happen once at each time. As discussed in Sec. 5.1.1, these aspects characterize a Poisson process, and the distribution of waiting times (inter-event times) is given by $\psi(\tau) = \alpha e^{-\alpha\tau}$, in which α is the rate for the events to occur. This Poisson assumption will lead to a Markovian description of epidemic models [5].

The Gillespie algorithm can be employed to simulate a continuous-time Markovian process, providing statistically exact results [181]. This method can be adapted to epidemic models by separating the dynamics into independent spontaneous processes and updating the states of the model at each time step, which is not fixed. If we consider Z independent Poisson processes, each occurring with rates $\nu_1, \ldots, \nu_Z$, the waiting times between events are given by $\psi_T(\tau) = Te^{-T\tau}$, where $T = \sum_{x=1}^{Z} \nu_x$ is the total rate, and x identifies the event. The probability that a specific event x occurs at a given time is ν_x/T. A random waiting time τ can be sampled using a uniformly distributed random number u by computing

$$u = \int_0^\tau Te^{-Tt}dt = 1 - e^{-T\tau} \ , \tag{3.1}$$

which leads to $e^{-T\tau} = 1 - u$. Since $1 - u$ is also uniformly distributed, we obtain $\tau = -\ln(u)/T$. This procedure captures the essence of the Gillespie algorithm as applied to epidemic models, where the rates can be, for example, $\nu_x = \mu$ for the healing event and $\nu_x = \lambda$ for the infection event. However, if the states of each node change at each time step, the list of all spontaneous processes must be continuously updated, and this task becomes unfeasible as the network size increases. Reference [182] presents the optimized Gillespie algorithm (OGA), which significantly reduces computational time compared to standard Gillespie algorithms, while maintaining statistical exactness. This improvement is due to the introduction of the phantom process, characterized by an event in which the state of the nodes does not change, but the time is still incremented. A phantom process

occurs whenever an infected node attempts to infect a neighbor that is already infected or recovered. The computational implementation of the OGA for the SIS model follows the steps described below.

(i) The initial condition is set by establishing the number of infected nodes, N_i, and the sum of the degrees of these infected nodes, N_n. Also, a list is created to store the labels of all infected nodes, denoted by $I[N_i]$.

(ii) The next step is to choose the event that will occur. A healing event, in which an infected node becomes susceptible with rate μ happens with probability

$$q = \frac{\mu N_i}{\mu N_i + \lambda N_n} \ , \tag{3.2}$$

where λ is the infection rate. With complementary probability $p = 1 - q$, an infected node is selected to attempt to infect one of its neighbors. This selection must be proportional to its degree under rejection probability $k_i/k_{\max}$. The neighbor is chosen at random, and the infection occurs if it is susceptible. If the neighbor is already infected, the event is classified as a phantom process.

(iii) The values of N_i, N_n are updated as well as the list $I[N_i]$. An optimized way to update this list is to replace the entry corresponding to the index chosen in the previous step with the entry of the last position in the list, so that the list size will be shortened by 1.

(iv) Time is incremented according to $t \to t + \Delta t$, where

$$\Delta t = \frac{-\ln(u)}{\mu N_i + \lambda N_n} \ , \tag{3.3}$$

where u is a pseudo-random number uniformly distributed in the interval $(0, 1)$.

(v) Steps (ii), (iii), and (iv) are repeated until the total simulation time $t_{\max}$. If the system reaches the absorbing state, i.e., $N_i = 0$, a quasi-stationary (QS) method (described in Appendix B) must be applied to return the system to an active configuration.

The above-described implementation can be easily adapted for other epidemic models. For instance, to simulate the SIR model, step (ii) would involve a recovery event instead of a healing event. In addition to the list of infected nodes, a list of recovered nodes, $R[N_r]$, must also be maintained, where N_r is the number of nodes in the recovered compartment. This list should also be updated in step (iii).

APPENDIX D – Visibility Graph algorithm

As discussed in Ch. IV, the VG method maps time series onto networks, and the resulting VG is expected to inherit characteristics from the original process underlying the time series [23]. The computational implementation of this method is straightforward and can be achieved by applying the visibility criterion from Eq. (4.1). However, using this condition directly yields a computational complexity of $O(t_s^2)$, where t_s is the length of the time series. This is because all possible connections between points in the time series must be checked. The algorithm therefore starts by verifying the possible connectivity between a time series value y_a and another value y_b, ensuring that no intermediate point y_c obstructs their visibility, as prescribed by Eq. (4.1). The variable c must be updated inside the loops over a and b. Also, the VG will always be connected, since each node representing a value in the time series is connected at least to the node representing the next value. The pseudo-code for the VG algorithm is presented below.

Algorithm 1 Visibility Graph Algorithm

```
Input: array y[1..t_s]
Output: variable L (number of links in the VG)
L ← 0
for a ← 1 to t_s − 1 do
    c ← a + 1
    L ← L + 1                                   ▷ Because a is connected to c.
    for b ← a + 2 to t_s do
        test ← y[b] + ((y[a] − y[b])(b − c))/(b − a)      ▷ The visibility criterion.
        if y[c] < test then
            c ← b
            L ← L + 1                           ▷ Because a is connected to b.
        end if
    end for
end for
return L
```

To exemplify the computational implementation time of Alg. 1, we use five samples of randomly and uniformly distributed time series to generate their corresponding VG. The CPU time as a function of the time series length is shown in Fig. 4.1. The simulations were performed using C on a 13th Gen Intel(R) Core(TM) i7-13700F with 64GB of RAM. As can be observed in this figure, the computational complexity is slightly below $O(t_s^2)$. Still, the VG for a time series of 10^6 values takes less than 10 minutes to run on this

computer. However, if even larger time series are needed, an optimized approach for the VG algorithm is presented in [183], where the authors use the *divide & conquer* strategy to achieve a computational complexity of $O(t_s \log(t_s))$.

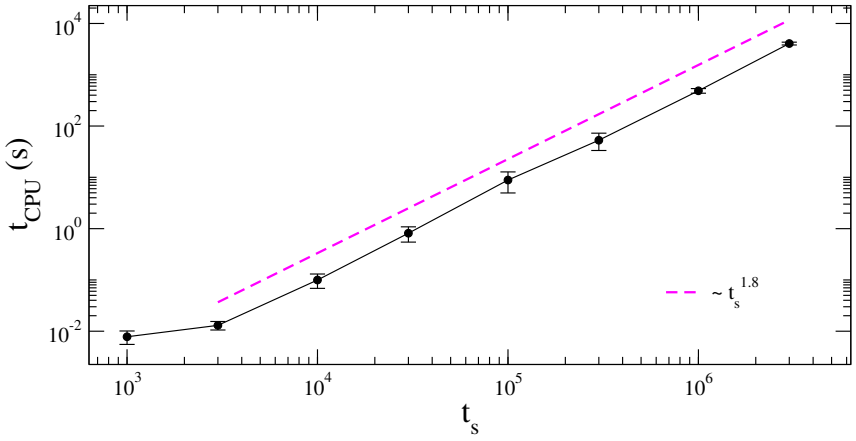

Figure 4.1 – CPU times as a function of time series length for the VG generated from five samples of time series with random values uniformly distributed. The error bars represent the standard deviation.

Finite-size and time analysis for VG

Besides the possible optimizations in the VG algorithm, another important consideration is how the length of the original system and the length of the time series used to generate the VG affect its measures. To address this, we considered the critical time series of the CP dynamics on two-dimensional lattices. The finite-size analysis is shown in Fig. 4.2, panels (a) and (b). The degree distributions are shown in panel (a) and exhibit heavier tails as the system size increases. The degree correlations, shown in panel (b), display a crossover from assortative to neutral behavior for smaller sizes, indicating that disassortative behavior will emerge for even larger sizes. The effect of the time series size is explored in panels (c) and (d) of Fig. 4.2, showing the degree distribution and the degree correlations, respectively. For this analysis, the lattice size was fixed at $L = 1000$. It can be observed that the disassortative behavior characteristic of VGs from critical time series emerges as the length of the time series increases.

Another question that may arise in studying VGs is whether the resolution of the time series influences the VG measures. Figure 4.3 explores the role of temporal resolution by comparing two time series derived from the same original system and dynamics but differing by one order of magnitude in time resolution. What we observe is that the effect of increasing time resolution is equivalent to increasing the size of the time series. This is

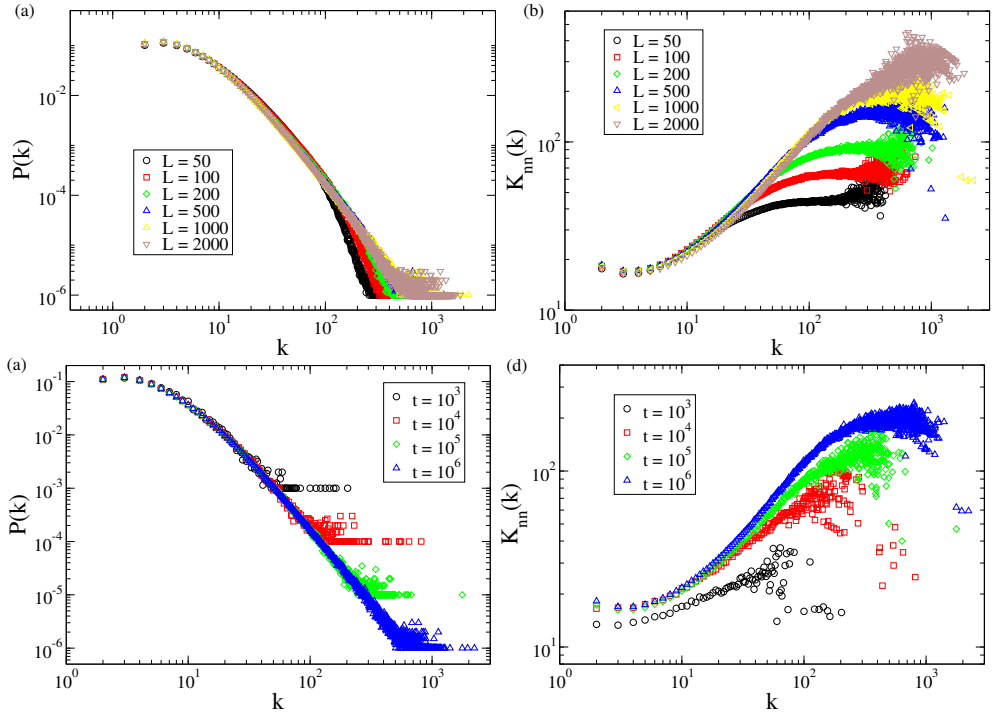

Figure 4.2 – Finite-size and time analysis for VGs obtained for critical CP dynamics ($\lambda_c = 1.6487$) on two-dimensional lattices. Finite-size analysis of (a) degree distribution and (b) degree correlations for series length fixed to 10^6 points equally spaced over intervals $\delta t = 1$. Finite-time analysis of (c) degree distribution and (d) degree correlations for fixed size $L = 1000$ and time resolution $\delta t = 1$.

easily verified by comparing Fig. 4.3 to panels (c) and (d) of Fig. 4.2. This allows us to fix the time series resolution and analyze only the finite-time scaling. All the time series used in this thesis were constructed with $\delta t = 1$, since the healing time in the epidemic models was set to time unit.

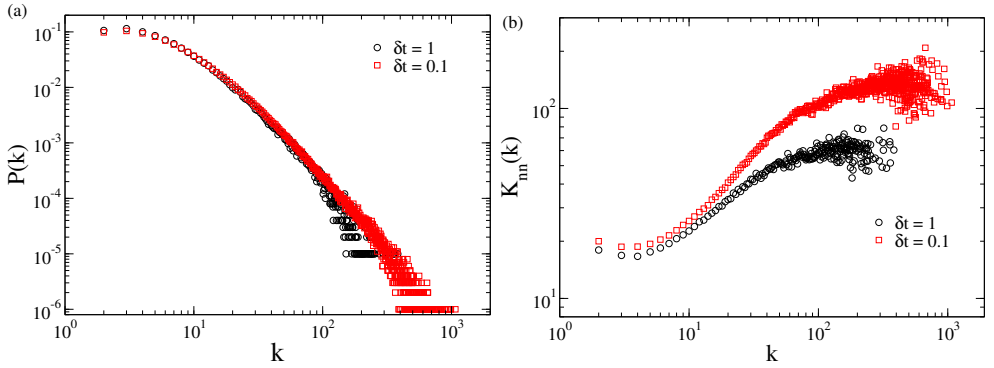

Figure 4.3 – Effects of time series resolution for VGs obtained for critical CP dynamics on two-dimensional lattices using $\lambda_c = 1.6487$. The system size is $L = 100$, and the time series corresponds to a time interval $t_s = 10^5$ with points equally spaced with intervals $\delta t = 0.1$ or $\delta t = 1$. Panel (a) presents the degree distributions, and panel (b) the average degree of the nearest neighbors.

APPENDIX E – Intermittent Networks algorithm

The intermittent networks explored in Ch. V constitute a possible approach for incorporating the temporal dimension into a contact structure. The method investigated in this thesis is based on starting from a static backbone network with a fixed number of contacts per node, and then attaching a dynamics of activation to nodes or links. The dynamics are governed by an inter-event time distribution, in which the event is the change of state of the node or link. The computational implementation mainly consists of the following tasks: (i) Creating a list to store the times of change for each node/link (t_{ch}) and filling it with a random variable distributed according to the inter-event time distribution $\psi(\tau)$ by using a pseudo-random number u uniformly distributed in the interval $(0, 1)$ and a cumulative probability distribution associated with the variable τ. This will be the time of the first change in the state of each node/link. (ii) Assigning the initial states ϵ to the nodes/links as either active ($\epsilon = 1$) or inactive ($\epsilon = 0$) with equal probability ($p = 0.5$). (iii) Evolving the dynamics of interest in the network. In this thesis, this dynamic corresponds to a spreading process, modeled by the OGA. Time in the simulation will evolve as determined by the spreading process. If $t \geq t_{\mathrm{ch}}$ for a node/link, its state must be updated.

However, how this last task is performed is crucial to the computational viability of the simulation. If at each time step, all nodes/links have their states checked for updates, the computational complexity will limit the size of the backbone network. To overcome this issue, an optimized solution is to update the states of nodes/links only when they are needed for the spreading process. For instance, when an infected node is chosen to infect a neighbor, the states of both nodes must be checked and updated if needed. All past changes in their states are then applied until $t_{\mathrm{ch}} > t$. Lines 20 to 23 in Alg. 2 show how the state updates occur. Similarly, when a node is chosen to be healed, its state is verified and updated if needed. For link intermittency, when an infection event occurs, the connection between the infected node and the neighbor to be infected is also checked and updated. Using this algorithm, we analyzed intermittent networks with size up to $N = 10^7$.

Algorithm 2 SIS dynamics in a node intermittent network

Input: β, τ_0, τ_{med}, λ, $t_{\max}$, network structure.
$r \leftarrow \beta(\tau_{\text{med}} - \tau_0) + \tau_0 - 2\tau_{\text{med}}$
Initialize variables: $t \leftarrow 0$, I, σ. ▷ $\sigma = 0$: susceptible; $\sigma = 1$: infected.
for $i \leftarrow 1$ to N **do** ▷ Uniformly distribute the initial states of the nodes.
    $prob \leftarrow \mathtt{u}$ ▷ u is a pseudo-random number uniformly distributed in (0,1).
    if $prob > 0.5$ **then**
        $\epsilon[i] \leftarrow 1$
    else
        $\epsilon[i] \leftarrow 0$
    end if
    $t_{ch}[i] \leftarrow (\tau_0 + r)(1 - \mathtt{u})^{1/(-\beta+1)} - r$
end for
while $t < t_{\max}$ **do** ▷ SIS model dynamics via OGA
    $Z \leftarrow \mathtt{u}$
    $p_{\text{inf}} = \lambda N_n/(N_i + \lambda N_n)$
    $\Delta t \leftarrow -\ln(\mathtt{u})/(N_i + \lambda N_n)$
    if $Z < p_{\text{inf}}$ **then** ▷ Infection event
        Select an infected node q from I chosen proportionally to its degree.
        if $t > t_{ch}[q]$ **then** ▷ The state of node q should already be updated.
            repeat ▷ This part updates the state of node q until t.
                Flip $\epsilon[q]$
                $t_{ch}[q] \leftarrow (\tau_0 + r)(1 - \mathtt{u})^{1/(-\beta+1)} - r + t_{ch}[q]$
            until $t_{ch}[q] \geq t$
        end if
        if $\epsilon[q] == 1$ **then**
            Randomly select a neighbor w of q.
            if $t > t_{ch}[w]$ **then**
                Update the state of w.
            end if
            if $\sigma[w] == 0$ and $\epsilon[w] == 1$ **then**
                w becomes infected.
                Update variables I, N_i, N_n, and σ.
            end if
        end if
    else ▷ Healing event
        Randomly select an infected node q from I.
        if $t > t_{ch}[q]$ **then**
            Update the state of node q.
        end if
        q becomes susceptible.
        Update variables I, N_i, N_n, and σ.
        if $N_i == 0$ **then**
            Use the QS method.
            Update variables I, N_i, N_n, and σ.
        end if
    end if
    $t \leftarrow t + \Delta t$
end while